UNIVERSITÀ DEGLI STUDI DI PARMA
DIPARTIMENTO DI INGEGNERIA DELL'INFORMAZIONE

Dottorato di Ricerca in Tecnologie dell'Informazione
XXVIII Ciclo

Alessandro Ugolini

Physical and MAC layer techniques for next generation satellite communications

DISSERTAZIONE PRESENTATA PER IL CONSEGUIMENTO
DEL TITOLO DI DOTTORE DI RICERCA

GENNAIO 2016

UNIVERSITÀ DEGLI STUDI DI PARMA

Dottorato di Ricerca in Tecnologie dell'Informazione

XXVIII Ciclo

Physical and MAC layer techniques for next generation satellite communications

Coordinatore:

Chiar.mo Prof. Marco Locatelli

Tutor:

Chiar.mo Prof. Giulio Colavolpe

Dottorando: *Alessandro Ugolini*

Gennaio 2016

Table of Contents

List of Figures

List of Tables

List of Acronyms

AIR	achievable information rate
APC	average power constraint
APSK	amplitude/phase shift keying
ASE	achievable spectral efficiency
AWGN	additive white Gaussian noise
BCH	Bose, Chaudhuri, and Hocquenghem
BCJR	Bahl-Cocke-Jelinek-Raviv
BER	bit error rate
BPF	band-pass filter
BPSK	binary phase shift keying
CDF	cumulative distribution function
CND	check-node decoder
CR	conventional receiver
CS	channel shortening
DPD	data predistorter

DVB	digital video broadcasting
DVB-S	digital video broadcasting for satellite
DVB-S2	digital video broadcasting for satellite, 2nd generation
DVB-S2X	digital video broadcasting for satellite, 2nd generation extensions
EO	Earth observation
EXIT	extrinsic information transfer
FDM	frequency division multiplexing
FE	front-end
FS	fractionally-spaced
FSM	finite-state machine
FTN	faster-than-Nyquist
GD	gradient descent
HPA	high power amplifier
IBO	input back-off
ICI	interchannel interference
IMUX	input multiplexer
ISI	intersymbol interference
LDPC	low-density parity-check
MAC	multiple access channel
MAP	maximum a posteriori
MF	matched filter

MI	mutual information
MMSE	minimum mean-square error
MODCOD	modulation and coding scheme
MSE	mean-square error
MUD	multiuser detector
OBO	output back-off
OMUX	output multiplexer
pASE	pragmatic achievable spectral efficiency
PDF	probability density function
PER	packet error rate
PPC	peak power constraint
PSK	phase shift keying
QPSK	quadrature phase shift keying
RRC	root-raised cosine
SE	spectral efficiency
SISO	soft-input soft-output
SNR	signal-to-noise ratio
SPD	signal predistorter
SUD	single-user detector
TDM	time division multiplexing
TFP	time-frequency packing
VND	variable-node decoder

Introduction

In the broad area of modern telecommunications, satellite communications are a growing field, which, year after year, offers an increasing variety of services. Among the many applications of communications through a satellite link, we mention the delivery of video signals, internet access, mobile telephony. Moreover, satellites are also widely used in localization scenarios, security applications, traffic control, and Earth observation missions. This growing demand has pushed the research community towards the study of methods to exploit more efficiently the limited bandwidth available.

The work presented in this thesis, hence, falls within the scope of the improvement of the *spectral efficiency*, that is, the amount of information per unit of bandwidth and time, of modern satellite communications systems. We will discuss and analyze several different scenarios, proposing the application of advanced techniques to maximize the spectral efficiency in each case. We point out that said techniques are completely general, and can be successfully applied to many different telecommunications scenarios, not limited to satellite links.

After a brief overview of some techniques and tools that will be applied to the different scenarios, provided in Chapter 1, each chapter focuses on a different problem.

Chapter 2 presents the results obtained in support of the standardization of the extensions to the current standard for digital video broadcasting. In this scenario, aimed at the delivery of a video stream, we will derive the optimal transmission rate that can be supported by current architectures, and we will then investigate the application of

advanced techniques at the transmitter and at the receiver.

Chapter 3 still focuses on signal broadcasting, but in a scenario in which two *co-located* satellites are available. Co-located satellites are commonly used as a backup in case of failure or to cover different frequency bands. Instead, we will study the potential benefits arising from the simultaneous activation of the two satellites to serve the same user on the same frequency band. We will analyze different models for the communication channel, deriving information theoretic bounds for the transmission rates under the assumption of different transceiver strategies.

In Chapter 4, we propose the application of *multiuser detection* in the forward link of a multibeam satellite system. In this application, corresponding, for example, to internet access through satellite, each user experiences a high level of interference coming from signals in adjacent cells. We will analyze and compare three different scenarios, corresponding to three alternative transceiver schemes.

Finally, Chapter 5 targets the spectral efficiency optimization in Earth observation links. In this scenario, the information data to be transmitted are generated on the satellite, for example as images of the Earth surface, and then transmitted to ground stations. We will consider two different configurations and compare the application of various approaches, both at the transmitter and at the receiver sides.

Chapter 1

Background

This chapter provides a quick overview of some techniques that will be applied to the different scenarios addressed in the next chapters. In particular, the problem of maximum a posteriori (MAP) symbol detection will be addressed first. Then, since optimal MAP detection is often unfeasible on a realistic channel, some suitable techniques for complexity reduction are introduced. Finally, a technique that allows to increase the spectral efficiency (SE) of transmission systems by properly optimizing the symbol interval and the frequency spacing of the transmitted signals is described.

1.1 MAP Symbol Detection: the BCJR Algorithm

In this section we briefly review the most common algorithm for MAP symbol detection, the Bahl-Cocke-Jelinek-Raviv (BCJR) algorithm, named after the authors who first proposed it [1]. Let us consider, for the sake of simplicity, a discrete-time linear intersymbol interference (ISI) channel,[1] for which the received signal can be expressed as

$$y_k = \sum_{\ell=0}^{L} h_\ell x_{k-\ell} + w_k\,, \quad k = 0,\ldots,K-1\,, \tag{1.1}$$

[1] The same considerations can be easily generalized to more complex channel models.

where x_k is the symbol transmitted during the k-th interval, $\{h_\ell\}_{\ell=0}^{L}$ are the coefficients of the channel response, assumed of finite length L, and w_k is a complex additive white Gaussian noise (AWGN) sample with variance N_0. This channel model can be equivalently represented in vector notation as

$$\mathbf{y} = \mathbf{H}\mathbf{x} + \mathbf{w}\,, \tag{1.2}$$

where we have defined the vectors $\mathbf{y} = [y_0, \ldots, y_{K-1}]^T$, $\mathbf{x} = [x_0, \ldots, x_{K-1}]^T$, and $\mathbf{w} = [w_0, \ldots, w_{K-1}]^T$, and the matrix $\mathbf{H}$, with dimensions $K \times K$, which represents the ISI channel. Note that this representation assumes the use of the Forney model [2] for the observable; however, the MAP symbol detection strategy can be straightforwardly applied also when adopting the Ungerboeck model [3, 4].

The aim of a MAP symbol detector is to compute a decision on each transmitted symbol based on the whole sequence of observed samples, as

$$\begin{aligned} \hat{x}_k &= \operatorname*{argmax}_{x_k} P(x_k|\mathbf{y}) \\ &= \operatorname*{argmax}_{x_k} p(\mathbf{y}|x_k) P(x_k)\,, \end{aligned} \tag{1.3}$$

where $P(x_k)$ is the a priori probability of the symbol, and $p(\mathbf{y}|x_k)$ is the probability density function (PDF) of the received vector conditioned to the transmission of the symbol x_k. If we interpret our channel with memory as a finite-state machine (FSM), with the state defined as $\sigma_k = [x_{k-1}, \ldots, x_{k-L}]$, the BCJR algorithm computes the PDF $p(\mathbf{y}|x_k)$ as

$$p(\mathbf{y}|x_k) = \sum_{\sigma_k, \sigma_{k+1}} \alpha_k(\sigma_k)\beta_{k+1}(\sigma_{k+1})p(y_k|x_k, \sigma_k)\,. \tag{1.4}$$

The terms $\alpha_k(\sigma_k)$ and $\beta_{k+1}(\sigma_{k+1})$ in (1.4) are the forward and backward metrics of the BCJR, respectively, and they can be recursively updated as

$$\alpha_{k+1}(\sigma_{k+1}) = \sum_{x_k, \sigma_k} \alpha_k(\sigma_k)p(y_k|x_k, \sigma_k)P(x_k) \tag{1.5}$$

$$\beta_k(\sigma_k) = \sum_{x_k, \sigma_{k+1}} \beta_{k+1}(\sigma_{k+1})p(y_k|x_k, \sigma_k)P(x_k)\,, \tag{1.6}$$

provided that the starting values of the recursions are properly initialized.

The MAP symbol detection strategy is then composed of a forward and a backward stage, in which the quantities (1.5) and (1.6) are computed, respectively, followed by the computation of the a posteriori probabilities on the symbols, $P(x_k|\mathbf{y})$, through (1.4) and (1.3). The BCJR algorithm is a soft-input soft-output (SISO) detector, that, together with decisions on symbols, provides reliability information on said decisions, that can be exploited by a properly designed decoder. The described detection algorithm can be conveniently implemented by means of the framework provided by factor graphs and the sum-product algorithm [5].

1.2 Mismatched Detection

A key problem, related to the analysis and the design of a communication system, is the evaluation of the ultimate performance limit imposed by a given channel, to be interpreted as an ideal benchmark for any practical system over the same channel. An important performance limit is given by the achievable information rate (AIR), that is, the average mutual information per symbol, which is defined as

$$I(\mathbf{x};\mathbf{y}) = \lim_{K\to\infty} \frac{1}{K} \mathrm{E}\left[\log_2 \frac{p(\mathbf{y}|\mathbf{x})}{\sum_{\mathbf{x}'} p(\mathbf{y}|\mathbf{x}')P(\mathbf{x}')}\right] \quad [\text{bit/ch. use}]\,. \tag{1.7}$$

In (1.7), $\mathrm{E}[\cdot]$ denotes the expectation operator, $p(\mathbf{y}|\mathbf{x})$ is the channel PDF, and $P(\mathbf{x})$ is the probability distribution of the transmitted symbols. With reference to the channel (1.2), the channel PDF is

$$\begin{aligned} p(\mathbf{y}|\mathbf{x}) &= \frac{1}{(\pi N_0)^K} \exp\left(-\frac{\|\mathbf{y}-\mathbf{H}\mathbf{x}\|^2}{N_0}\right) \\ &= \frac{1}{(\pi N_0)^K} \exp\left(-\frac{\mathbf{y}^\dagger\mathbf{y} - 2\Re\left\{\mathbf{y}^\dagger\mathbf{H}\mathbf{x}\right\} + \mathbf{x}^\dagger\mathbf{G}\mathbf{x}}{N_0}\right), \end{aligned} \tag{1.8}$$

where the operator $(\cdot)^\dagger$ stands for Hermitian (i.e., transposed and complex conjugated), $\Re$ denotes the real part of a complex number, and $\mathbf{G} = \mathbf{H}^\dagger\mathbf{H}$. The AIR (1.7) can be effectively computed for a practical channel with the numerical method described in [6]. However, this method assumes the availability of the optimal BCJR detector for the channel under considerations, hence, the knowledge of the PDF (1.8).

If the channel PDF is not known, or the optimal detector has an excessive complexity that does not allow for a practical implementation, we cannot directly resort to the technique in [6].

In this case, we can compute a lower bound on the AIR, obtained by replacing $p(\mathbf{y}|\mathbf{x})$ in (1.7) with an arbitrary auxiliary channel law $q(\mathbf{y}|\mathbf{x})$ with the same input and output alphabets as the original channel, according to the principle of mismatched detection [7]. The resulting lower bound is

$$I_q(\mathbf{x};\mathbf{y}) = \lim_{K\to\infty} \frac{1}{K} \mathrm{E}\left[\log_2 \frac{q(\mathbf{y}|\mathbf{x})}{\sum_{\mathbf{x}'} q(\mathbf{y}|\mathbf{x}')P(\mathbf{x}')}\right] \quad [\text{bit/ch. use}]\,. \tag{1.9}$$

If the auxiliary channel law represents a finite-state channel, $q(\mathbf{y}|\mathbf{x})$ can be computed, by using the optimal MAP symbol detector for that auxiliary channel [6]. Clearly, this detector will be suboptimal for the actual channel, and hence the resulting AIR will be a lower bound on the actual one. However, this bound is achievable by that specific receiver, according to mismatched detection [6, 7]. We point out that the sequence $\mathbf{y}$ is generated according to the real channel model, and hence the adopted technique can be successfully applied to derive lower bounds on the information rate for any channel model.

1.3 Channel Shortening

The complexity of the optimal MAP detection algorithm can quickly become unmanageable when the size of the trellis increases, that is, when the channel memory is high and/or the dimension of the adopted constellation grows. There have been two main directions to address this problem: i) to perform detection on the original trellis but exploring only a fraction of it (see, for example, [8–10]), or ii) to build a reduced trellis that is then processed with full complexity (refer to [11, 12]). The technique known as channel shortening (CS) falls in the second category. The history of CS receivers starts in the early 1970s with the work of Falconer and Magee [13], which originated further research on the topic [14–20]. In all these works, the receivers have been designed to minimize the mean-square error (MSE) between the transmitted and

received signals. This strategy, however, does not directly correspond to the highest achievable transmission rate from an information theoretical perspective.

The work of Rusek and Prlja [21] generalizes the previous works on CS by proposing a technique to design the optimal receiver for a given reduced complexity, from an information theoretic point of view, for a generic linear channel. In particular, the optimal front-end (FE) filter for channel shortening and branch metrics for trellis processing are derived in closed form under the assumption of Gaussian inputs, but the authors show that the performance is excellent also when adopting practical discrete constellations.

In this section, we briefly review the main results of [21] for the special case of ISI channels. Let us consider again the model (1.2) and the corresponding channel PDF (1.8). To achieve the desired complexity reduction, (1.8) can be replaced by the mismatched channel law

$$q(\mathbf{y}|\mathbf{x}) = \frac{1}{(\pi N_{\mathrm{r}})^K} \exp\left(-\frac{\mathbf{y}^\dagger \mathbf{y} - 2\Re\left\{\mathbf{y}^\dagger \mathbf{H}^{\mathrm{r}} \mathbf{x}\right\} + \mathbf{x}^\dagger \mathbf{G}^{\mathrm{r}} \mathbf{x}}{N_{\mathrm{r}}} \right), \tag{1.10}$$

where the matrices $\mathbf{H}^{\mathrm{r}}$, $\mathbf{G}^{\mathrm{r}}$ and the mismatched noise density N_{r} are subject to optimization.[2] By removing the terms irrelevant for the detection process, namely those that do not depend on the transmitted symbols $\mathbf{x}$, the mismatched law (1.10) can be redefined as

$$q(\mathbf{y}|\mathbf{x}) = \exp\left(2\Re\left\{\mathbf{y}^\dagger \mathbf{H}^{\mathrm{r}} \mathbf{x}\right\} + \mathbf{x}^\dagger \mathbf{G}^{\mathrm{r}} \mathbf{x}\right), \tag{1.11}$$

where, without loss of generality, N_{r} has been absorbed into the design of $\mathbf{H}^{\mathrm{r}}$, and $\mathbf{G}^{\mathrm{r}}$. We can notice from (1.11) that the need for trellis processing arises only from the matrix $\mathbf{G}^{\mathrm{r}}$; hence, $\mathbf{G}^{\mathrm{r}}$ must be computed such that $(\mathbf{G}^{\mathrm{r}})_{mn} = 0$ for $|m-n| > L$, where $(\mathbf{G}^{\mathrm{r}})_{mn}$ denotes the element of the matrix at row m and column n, and L is the desired length of the resulting shortened channel response. To achieve an effective complexity reduction, L must be selected to be lower than the actual channel memory.

In [21], the matrices $\mathbf{H}^{\mathrm{r}}$, and $\mathbf{G}^{\mathrm{r}}$ are designed to maximize the lower bound (1.9) on the AIR of the channel. For ISI channels, $\mathbf{H}^{\mathrm{r}}$ and $\mathbf{G}^{\mathrm{r}}$ are perfectly characterized by the discrete sequences $\mathbf{h}^{\mathrm{r}}$ and $\mathbf{g}^{\mathrm{r}}$, and the derivation of the optimal CS filter and

[2] Note that (1.10) does not necessarily need to be a valid PDF.

channel response can be simplified. Let $H(\omega)$ and $G(\omega)$ be the Fourier transforms of $\mathbf{h}^{\mathrm{r}}$ and $\mathbf{g}^{\mathrm{r}}$, respectively. It can be proved [21] that, for an ISI channel with transfer function $H(\omega)$ and a receiver trellis characterized by $G^{\mathrm{r}}(\omega)$, with $\min_{\omega} G^{\mathrm{r}}(\omega) > -1$, the optimal receiver filter is

$$H^{\mathrm{r}}(\omega) = \frac{H^{\dagger}(\omega)}{|H(\omega)|^2 + N_0}(G^{\mathrm{r}}(\omega) + 1), \tag{1.12}$$

where $H(\omega)$ is the Fourier transform of the actual channel response $\mathbf{h}$. Notably, the filter (1.12) can be seen as the cascade of a minimum mean-square error (MMSE) filter, that does not depend on the reduced channel memory L, followed by a filter with transfer function $G^{\mathrm{r}}(\omega)+1$. When the memory L is equal to zero, (1.12) reduces to a classical MMSE filter.

The steps to compute $G^{\mathrm{r}}(\omega)$ can be summarized as follows (refer to [21] for a complete theoretical analysis), for a channel with known transfer function $H(\omega)$ and noise density N_0.

1. Compute
$$B(\omega) = \frac{N_0}{|H(\omega)|^2 + N_0} \tag{1.13}$$
and its inverse Fourier transform $\{b_\ell\}_{\ell=-L}^{L}$.

2. Define the vector $\mathbf{b} = [b_1, \ldots, b_L]$ and the matrix $\mathbf{B}$ as the Toeplitz matrix of dimension $L \times L$ formed from the vector $[b_0, \ldots, b_{L-1}]$, that is
$$\mathbf{B} = \begin{bmatrix} b_0 & b_1 & \ldots & b_{L-1} \\ b_1 & b_0 & \ldots & b_{L-2} \\ \vdots & \vdots & \ddots & \vdots \\ b_{L-1} & b_{L-2} & \ldots & b_0 \end{bmatrix}.$$

3. Compute the real-valued scalar $c = b_0 - \mathbf{b}\mathbf{B}^{-1}\mathbf{b}^{\dagger}$.

4. Define the vector $\mathbf{u} = \frac{1}{\sqrt{c}}[1, -\mathbf{b}\mathbf{B}^{-1}]$.

5. Finally, compute the optimal reduced channel response $\mathbf{g}^{\mathrm{r}}$ as

$$g_\ell^{\mathrm{r}} = \sum_{i=\max(0,\ell)}^{\min(L,L+\ell)} u_i u_{i-\ell}^* - \delta_\ell\,, \quad \ell = -L,\ldots,L\,, \tag{1.14}$$

where δ_k is the Kronecker delta function, and its Fourier transform $G^{\mathrm{r}}(\omega)$.

The authors of [21] also provide a closed-form expression for a lower bound to the AIR of the channel, achievable with the optimal detector for the considered reduced trellis, under the assumption of Gaussian distributed input symbols. This lower bound can be computed as $I_{\mathrm{LB}} = \log_2 \frac{1}{\sqrt{c}}$.

As mentioned, although the theoretical derivation of the CS filters assumes that the input symbols have Gaussian distribution, the performance of the CS technique is excellent even with discrete input alphabets. To demonstrate this fact, we show in Figure 1.1, where E_{s} is the average energy per symbol, the AIR I_R of a binary phase shift keying (BPSK) modulation on the EPR4 channel, with response $\mathbf{h} = [0.5\ 0.5\ -0.5\ -0.5]$. The figure compares a full complexity BCJR detector, taking into account the full channel memory and having a trellis with 8 states, with a BCJR processing a reduced trellis with dimension increasing from a single state, for $L = 0$, to 4 states, for $L = 2$.

The described procedure to compute the optimal CS filters assumes that the channel is perfectly known at the receiver. In particular, the channel response $\mathbf{h}$ and the noise density N_0 are required for the computation of (1.12). If the channel parameters are unknown, the classical approach is to estimate them by standard estimation techniques, as exemplified in [22]. An alternative approach is that presented in [22], which relies on an MMSE autocorrelation estimator and is denoted as adaptive CS. The derivation of the optimal filters, in this case, is based on the observation that the term $B(\omega)$ in (1.13) is the power spectral density of the error at the output of the MMSE filter [23]. If we define $e_k = \hat{x}_k - x_k$ the error between the output of the MMSE equalizer $\hat{x}_k$ and the transmitted symbol x_k, then the sequence $\{b_\ell\}_{\ell=-L}^{L}$ is the autocorrelation of said error, that is, $b_\ell = \mathrm{E}\left[e_{k+\ell} e_k^*\right]$.

In a practical implementation on a continuous-time channel with ISI, the block diagram of the receiver is shown in Figure 1.2. A sufficient statistic for detection is ex-

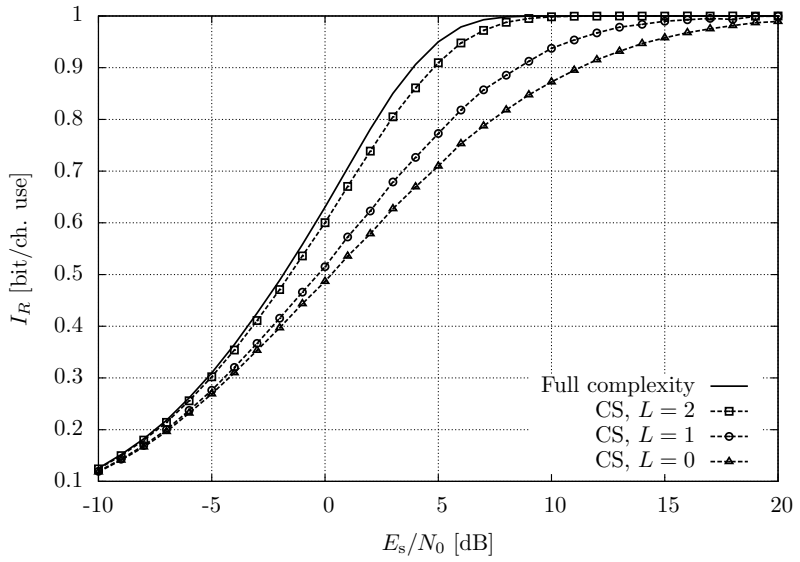

Figure 1.1: AIR for the CS receiver with increasing complexity on the EPR4 channel using a BPSK modulation.

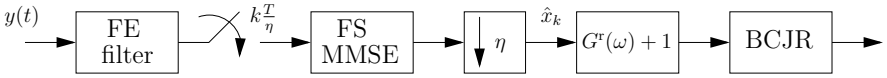

Figure 1.2: Block diagram of the receiver using the adaptive CS technique.

tracted from the received signal by sampling the output of a FE filter with η samples per symbol time. These samples are then processed by a fractionally-spaced (FS)-MMSE equalizer. The output of the equalizer is then downsampled with a factor η to obtain the estimated symbol sequence $\hat{\mathbf{x}} = \{\hat{x}_k\}_{k=0}^{K-1}$, from which the error sequence $\mathbf{e} = \{e_k\}_{k=0}^{K-1}$ is computed as $\mathbf{e} = \hat{\mathbf{x}} - \mathbf{x}$. Finally, the coefficients b_ℓ are estimated as

$$\hat{b}_\ell = \frac{1}{K-\ell} \sum_{k=0}^{K-\ell-1} e_{k+\ell} e_k^*, \quad \ell = -L, \ldots, L.$$

From the coefficients b_ℓ, the reduced channel response can be computed as in the classical CS approach (1.14).

In [22] it is shown that this adaptive approach is convenient when the channel

has a response of infinite length with only few poles, because in this case the MMSE equalizer has a short impulse response. Moreover, there is no need to perform any Fourier transform to compute the response $\mathbf{g}^{\mathrm{r}}$, thus reducing the receiver complexity. Furthermore, as mentioned, this receiver structure does not need any information about the channel, hence it is completely adaptive and applicable to channels with unknown response. This is the case, for example, of a channel arising from the application of the time-frequency packing (TFP) technique, detailed in the next section.

Finally, we mention that the interaction between CS complexity reduction and interference cancellation for iterative receivers has been recently addressed in [24, 25]. In particular, the authors take into account the reliability of the soft information provided by the decoding stage to properly update the sequences $\mathbf{h}^{\mathrm{r}}$ and $\mathbf{g}^{\mathrm{r}}$ at each iteration.

1.4 Time-Frequency Packing

In traditional digital communications, orthogonal signaling is often adopted to ensure the absence of ISI and interchannel interference (ICI). However, when finite-order constellations are used, it is possible to increase the SE of communication systems by giving up the orthogonality condition and by introducing a controlled interference into the signal. This idea was first introduced by Mazo for single carrier transmissions with the name of faster-than-Nyquist (FTN) signaling [26]. FTN signaling is a linear modulation technique that reduces the time spacing between two adjacent pulses (the symbol time) well below that ensuring the Nyquist condition, thus introducing controlled ISI [26–28]. If the receiver can cope with the ISI, the efficiency of the communication system is increased. In the original papers on FTN signaling [26–28], this optimal time spacing is obtained as the smallest value giving no reduction of the minimum Euclidean distance with respect to the Nyquist case. This ensures that, asymptotically, the ISI-free bit error rate (BER) performance is reached when optimal detectors are used. More recently, this concept has been extended to multicarrier transmissions in [28]. In this case, intentional ICI is also introduced by reducing the frequency separation among carriers.

A multicarrier FTN signal can be expressed as

$$x(t) = \sum_k \sum_i x_k^{(i)} p(t - k\tau T) e^{j2\pi i \nu F t}, \tag{1.15}$$

where $x_k^{(i)}$ is the complex symbol transmitted during the k-th signaling interval over the i-th carrier, $p(t)$ is the base pulse, usually a pulse with root-raised cosine (RRC) spectrum with roll-off α, and T and F are the symbol time and frequency spacing that ensure orthogonality in the time and frequency domains, respectively.[3] The coefficients $\tau \leq 1$ and $\nu \leq 1$ are the compression factors for the symbol interval and frequency spacing, respectively. While setting them to 1 results in an orthogonal transmission, they can be reduced to a given extent without reducing the minimum Euclidean distance. The effects of the application of FTN in the time domain are schematically represented in Figure 1.3, which shows the transmission of a generic pulse $p(t)$ with orthogonal signaling (Figure 1.3(a)) and adopting a coefficient $\tau < 1$ (Figure 1.3(b)). We see how interference from adjacent pulses arises in the latter case.

From a practical point of view, FTN may require an optimal detector whose complexity, however, easily becomes unmanageable. No hints are provided in the original papers on how to perform the optimization in the more practical scenario where a reduced-complexity receiver is employed. From a theoretical point of view, although this technique has been proposed to increase the spectral efficiency of a communication system, the uncoded BER is used as figure of merit in place of the SE itself.

Before discussing ways to solve these problems, we need to introduce a few definitions. Let us consider the multicarrier transmission in (1.15) where νF is the frequency separation between two adjacent carriers and τT is the symbol time. We will collect in a vector $\mathbf{x}^{(i)} = \{x_k^{(i)}\}$ the input symbols transmitted over the i-th carrier. At the receiver side, a discrete-time set of sufficient statistics is extracted using a bank of matched filters (MFs) and we denote by $\mathbf{y}^{(i)} = \{y_k^{(i)}\}$ the samples at the output of the MF for the i-th carrier.

Depending on the allowed complexity at the receiver, different strategies can be adopted for detection. For example, the receiver can neglect both ICI and ISI and

[3] As far as F is concerned, its minimum value is $F = \frac{1+\alpha}{T}$.

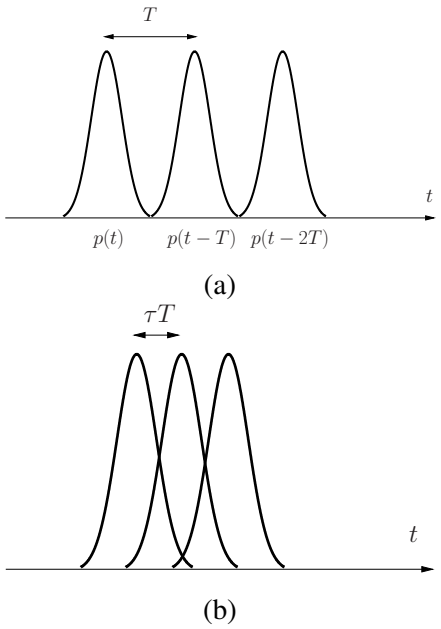

Figure 1.3: Schematic view of orthogonal (a) and FTN (b) signaling in the time domain.

adopt a symbol-by-symbol detector. In other words, instead of the optimal receiver for the actual channel, we could adopt the optimal receiver for a simplified auxiliary channel, for which the combined effect of ISI and ICI is modeled as a zero-mean Gaussian process independent of the additive thermal noise. Note that the interference is really Gaussian distributed only if the transmitted symbols are Gaussian distributed as well, and this is not the case in practice. Especially when the interference set is small, that is, when τ and ν are close to one, the actual interference distribution may substantially differ from a Gaussian distribution. However, the accuracy of this approximation is not of concern here: assuming Gaussian-distributed interference is anyway required to ensure that a symbol-by-symbol receiver is optimal, for the auxiliary channel model. Namely, it is like to say that the Gaussian assumption is a *consequence* of the choice of the symbol-by-symbol receiver. Once the simplified receiver has been selected, suboptimal for the channel at hand but optimal for the

considered auxiliary channel, it is possible to compute, by using the technique in [6], a lower bound on the AIR for that channel. According to mismatched detection [7], this lower bound is *achievable* by that particular suboptimal detector. The achievable spectral efficiency (ASE) is defined as the ratio between the achievable lower bound on the information rate and the product $\nu F \tau T$

$$\mathrm{ASE} = \frac{I_q\left(\mathbf{x}^{(i)};\mathbf{y}^{(i)}\right)}{\nu F \tau T}, \tag{1.16}$$

where νF is a measure of the bandwidth of the given subcarrier.

The most recent extension of the FTN principle is thus TFP in [29], where it is proposed to optimize ν and τ in order to maximize the ASE. The idea is very simple: by reducing ν and τ the bound on the AIR $I_q\left(\mathbf{x}^{(i)};\mathbf{y}^{(i)}\right)$ will certainly degrade due to the increased interference. However, the ASE (1.16) can be improved. Hence, the main quantity of interest is not the uncoded BER performance.[4] We may accept a degradation of the AIR provided that the ASE is increased. Improving the SE without increasing the constellation size is convenient since low-order constellations are more robust to impairments such as phase noise and nonlinearities.

In [29], the main concepts are presented with reference to a symbol-by-symbol detector and the AWGN channel, working on the samples at the MFs output. More sophisticated receiver architectures are considered in [30], still with reference to the AWGN channel. In general, there are several receiver architectures that have been considered for the detection of TFP signals, that include the CS technique described previously, as well as equalization [31] and filtering, followed by a MAP symbol detector based on a BCJR algorithm. Further gains can be obtained by using algorithms which detect more than one carrier at a time. In general, the larger the receiver complexity, the higher the gains that this technique allows to obtain. Its effectiveness has been demonstrated in several scenarios on wireless and optical channels [30, 32–34].

[4] Since there is no need to keep the same Euclidean distance as in the Nyquist case, there is no need to employ a base pulse satisfying the Nyquist condition. Thus TFP can be adopted for *any* base pulse.

Chapter 2

Optimization of Single-Satellite Broadcasting Systems

In recent years, the need to satisfy the growing demand for high data rates pushed the investigation towards the development of many techniques aimed at increasing the SE of broadcasting satellite systems. The digital video broadcasting for satellite, 2nd generation (DVB-S2) standard [35] was developed in 2003 with the main aim of improving the performance of existent DVB-S systems [36], while keeping a reasonable receiver complexity. At the end of 2012, the DVB project started the development of an evolution of DVB-S2, which was approved in March 2014 with the name of DVB-S2 extensions (DVB-S2X) [37]. The new standard has the aim of improving the SE achieved by DVB-S2 systems through the application of innovative techniques to different stages of the transceiver architecture.

The reference transmitter architecture for DVB-S consisted of a RRC shaping pulse with roll-off equal to 0.35, and a symbol rate of 27.5 Mbaud [36]. The same settings continued to be applied by DVB-S2, which, however, allows to operate also with increased symbol rates around 30 Mbaud thanks to the additional available roll-offs, 0.25 and 0.2 [35]. These relatively high roll-off values make the implementation of shaping filters and timing recovery easy, while the symbol rate values have been chosen to guarantee low interference from adjacent transponders and to ensure that

on-board satellite equipment is able to cope with the power dissipated by transponder filters [38]. As far as the receiver architecture is concerned, symbol-by-symbol detection is usually performed, followed by the decoding stage.

However, nowadays technological evolution allows to adopt smaller roll-off factors and more sophisticated detection and decoding techniques. This chapter proposes an overview of the techniques we considered in support of the DVB-S2X standardization process. Some of these techniques will be analyzed in detail and their performance will be assessed and compared with those of a classical DVB-S2 architecture. In particular, in the next sections we will address the following aspects.

The optimization of the signal bandwidth and symbol rate. As mentioned, the adoption of a smaller roll-off has allowed DVB-S2 systems to work with an increased symbol rate. In light of this consideration, we will perform a joint optimization of the symbol rate and of the roll-off factor, in order to derive the best transmission parameters. These values will take into account the full DVB-S2X channel model as specified in [39], thus including the presence of adjacent signals from other transponders, whose contribution is fundamental to evaluate the optimal signal bandwidth.

The use of a more sophisticated detection algorithm. It is reasonable to think that the use of a highly performing detector, specifically tailored for the nonlinear satellite channel, could increase the achieved SE. We will then present and compare different detection algorithms with different complexity.

The use of new channel codes. The DVB-S2 standard foresees the use of low-density parity-check (LDPC) codes in combination with Bose, Chaudhuri, and Hocquenghem (BCH) codes as outer code and the phase shift keying (PSK) and amplitude/phase shift keying (APSK) constellations specified in [35]. However, these modulation and coding schemes (MODCODs) offer a signal-to-noise ratio (SNR) granularity which does not allow to fully cover the spectral efficiency values of interest in broadcasting application scenarios. For this reason, new MODCODs have been designed [40] for linear and non-linear channels, which improve the SNR granularity and achieve higher spectral efficiency with respect to DVB-S2 [41]. For this reason, these new MODCODs have been included in the DVB-S2 extensions. While the design of new channel codes is beyond the scope of this chapter, we will evaluate the

performance of these new proposed schemes in some scenarios of interest and with different transceiver configurations.

The application of faster-than-Nyquist or time packing. In satellite systems, orthogonal signaling is often adopted to avoid ISI, at least in the absence of nonlinear distortions. When finite-order constellations are considered (such as, for example, PSKs), it is well known that the SE can be improved by relaxing the orthogonality condition, thus intentionally introducing ISI. In this case, the systems are working in the domain of the *Faster-than-Nyquist* paradigm [26–28, 42] or its extension known as *time packing* [29, 30, 33]. A similar effect could also be achieved by properly increasing the signal bandwidth at the transmitter output as shown in [33]. In fact, for fixed transponder filter bandwidths, an increase of the signal bandwidth will result in an increase of ISI. Since, as mentioned, the system operates in the presence of adjacent signals, an excessive bandwidth increase might not be feasible; however, the use of time packing adds another degree of freedom that can be properly exploited. For this reason, we will evaluate the performance of time packing applied to this broadcasting scenario.

The optimization of the transmitted pulse. During the standardization of DVB-S2X, it has been considered to redesign the shaping pulse adopted at the transmitter. There are examples showing that a properly designed pulse can allow to achieve SE gains on the linear channel [43], and similar techniques could be applied on the satellite channel. For implementation simplicity and compatibility with DVB-S2 systems, classical RRC pulses have been preferred in DVB-S2X. However, later in the chapter, we will mention an alternative possible approach to the pulse design.

The optimization of the signal constellations. DVB-S2 foresees the use of constellations with up to 32 points, distributed on up to 3 concentric rings. The design of new constellations for the satellite channel has been an active research field. In particular, for nonlinear channels, we mention [44–46], where the authors adopt a simulated annealing algorithm to jointly optimize the constellations and the bits to symbols labeling. The new constellations that were selected for DVB-S2X were proposed in [40], and foresee both an increased number of points (up to 256) and a different distribution of the points on the rings for cardinalities already foreseen by

DVB-S2, resulting in an improved spectral efficiency. In this chapter, we will propose a different design technique that allows to obtain optimized constellations for the satellite channel.

Finally, we point out that these techniques can also be combined. As an example, time packing can take advantage of the use of more sophisticated detection algorithms able to cope with the introduced (linear and nonlinear) ISI or of the use of a properly designed shaping pulse or constellation. Thus, separate investigations of these techniques would lead to wrong conclusions and an incomplete investigation.

In the next sections we will address the following topics. Sections 2.1 and 2.2 describe, respectively, the system model adopted throughout the chapter and the different figures of merit used to evaluate the performance of the analyzed systems. Section 2.3 presents different detection algorithms, while Sections 2.4 and 2.5 describe the tested optimization techniques and present their results. Finally, some concluding remarks are reported in Section 2.6.

2.1 System Model

This chapter analyzes the scenario of interest for broadcasting applications, i.e., a single-carrier-per-transponder scenario, where each satellite transponder is assumed to work with a single carrier occupying the entire transponder bandwidth. In this case, the on-board power amplifier can operate closer to saturation and hence improve its efficiency.

The complex envelope of the signal transmitted over the carrier under consideration can be expressed as

$$x(t) = \sum_{k=0}^{K-1} x_k p(t - kT_s),$$

where $\{x_k\}_{k=0}^{K-1}$ are the K transmitted symbols. The base pulse $p(t)$ has an RRC-shaped spectrum with roll-off factor α, and $T_s = \tau T$ is the symbol interval. T represents half of the main lobe duration of $p(t)$, while $\tau \leq 1$ is a compression factor deriving from the possible application of the time packing technique. The signal bandwidth is $W = (1+\alpha)/T$. The transmitted symbols belong to a given zero-mean

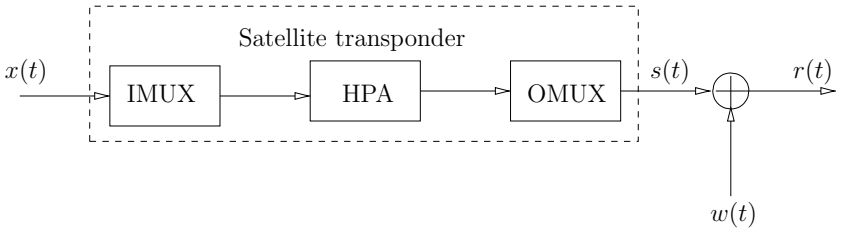

Figure 2.1: Block diagram of the satellite transponder.

complex constellation $\mathcal{X}$ having cardinality $\|\mathcal{X}\| = M$, possibly predistorted [47]. As foreseen by the transmission standards, these $M-$ary symbols are obtained from binary encoded symbols (possibly interleaved) through a proper mapping scheme, according to [35, 37]. In this chapter, we will adopt only the constellations usually adopted in broadcasting applications, that is those with M up to 16, but the same analyses could be extended to higher-dimensional constellations.

The block diagram of the satellite transponder is shown in Figure 2.1. It includes an input multiplexer (IMUX) filter, which removes the adjacent channels, a high power amplifier (HPA), and an output multiplexer (OMUX) filter aimed at reducing the spectral broadening caused by the nonlinear amplifier. The HPA AM/AM and AM/PM characteristics and the IMUX/OMUX frequency responses are described in [35] and reported in Figures 2.2 and 2.3. The OMUX filter has -3 dB bandwidth equal to 38 MHz. Although the HPA is a nonlinear memoryless device, the overall system has memory due to the presence of IMUX and OMUX filters.

The received signal is further corrupted by AWGN, whose low-pass equivalent $w(t)$ has power spectral density N_0. The received signal can be expressed as

$$r(t) = s(t) + w(t)\,,$$

where $s(t)$ is the signal at the output of the transponder. Moreover, we consider the presence of two interfering signals coming from adjacent transponders, with a frequency spacing of 40 MHz from the useful signal, and with the same power, as specified by the DVB-S2X channel model [39]. Finally, we point out that the whole investigation will be carried out under the assumption of perfect synchronization at the

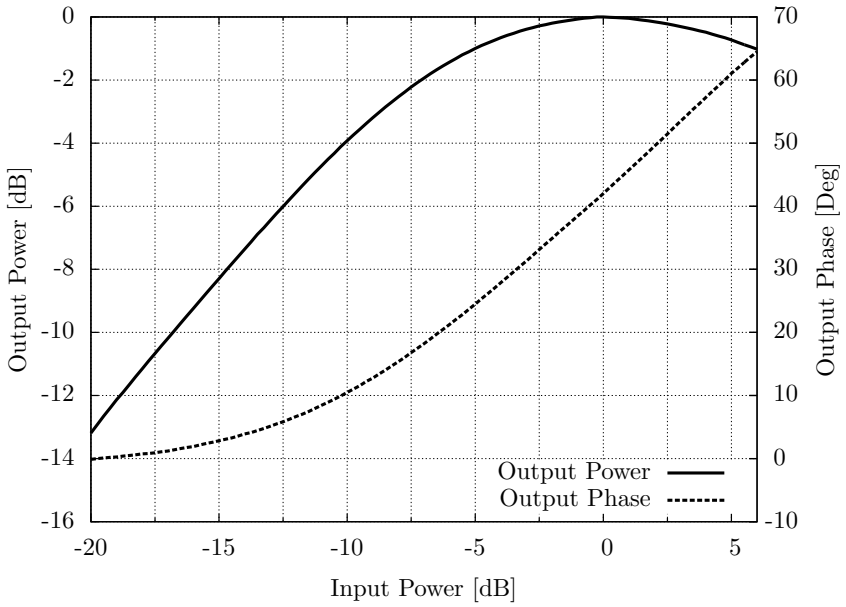

Figure 2.2: HPA characteristics.

receiver. Synchronization schemes for DVB-S2 systems are addressed, for example, in [48, 49].

2.2 Figures of Merit

This section introduces the different figures of merit used to assess the performance of the analyzed systems and techniques. The first one is an information-theoretic figure of merit, represented by the ASE, defined as

$$\mathrm{ASE} = \frac{I_R}{T_s B_{\mathrm{OMUX}}} \quad [\mathrm{bit/s/Hz}], \tag{2.1}$$

where I_R is the AIR and $B_{\mathrm{OMUX}} = 38$ MHz is the -3 dB bandwidth of the OMUX filter [35]. For a system with memory, I_R can be computed by means of the Monte Carlo method described in [6]. When a suboptimal detector is employed, this technique gives an achievable lower bound on the actual information rate, corresponding

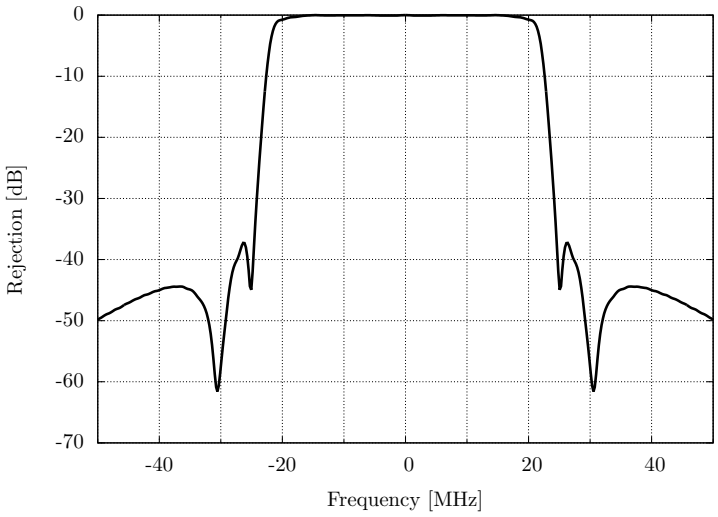

(a) IMUX

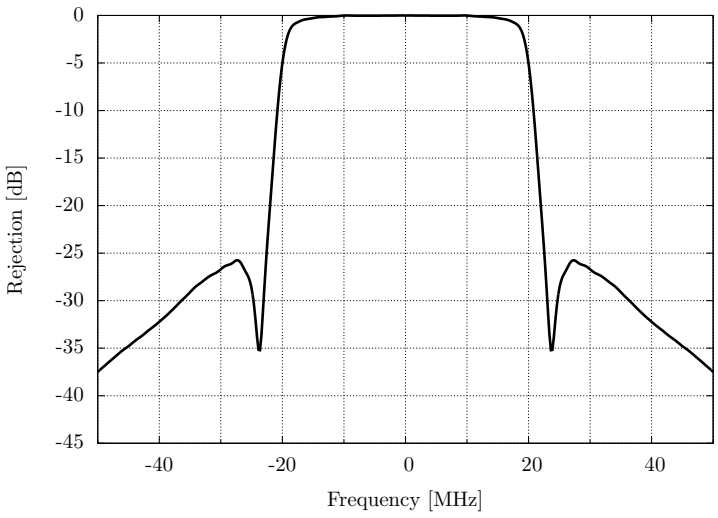

(b) OMUX

Figure 2.3: IMUX (a) and OMUX (b) filters characteristics.

to the information rate of the considered channel when that suboptimal detector is adopted [7]. More details on the computation of I_R have been reported in Section 1.2.

A more practical figure of merit is the SE achieved by a specific MODCOD. It is defined as

$$\mathrm{SE} = \frac{r \log_2(M)}{T_s B_{\mathrm{OMUX}}} \quad [\mathrm{bit/s/Hz}],$$

where r is the rate of the adopted binary code. The ASE for a given transceiver scheme (modulation, shaping pulse, symbol rate, and detector) shows the maximum SE that can be achieved by any practical MODCOD and employing joint detection and decoding. It can thus be computed with no reference to a practical coding scheme [6].

Finally, a third figure of merit that we will consider is the pragmatic achievable spectral efficiency (pASE), defined as in (2.1), but with I_R replaced by the the *pragmatic information rate* (also known as *BCJR-once rate* [50]). The pASE represents an upper bound on the SE of practical MODCODs when detection and decoding are performed separately, without any iteration between them.

We point out that other bandwidth definitions could be used as a reference without any loss of generality and any modification in the conclusions. All figures of merit will be represented into the Shannon plane as a function of P_{sat}/N, where P_{sat} is the HPA power at saturation and N is the noise power. This ratio is related to the average energy per transmitted symbol, E_{s}, by

$$\frac{P_{\mathrm{sat}}}{N} = \frac{E_{\mathrm{s}}}{N_0}\,\mathrm{OBO}\,\frac{R_{\mathrm{s}}}{B_{\mathrm{OMUX}}},$$

where R_{s} denotes the symbol rate, and OBO is the output back-off of the HPA. The SE will be computed for a P_{sat}/N value corresponding to a target packet error rate (PER) of 10^{-3}.

2.3 Detection Algorithms for the Nonlinear Channel

This section describes the detection algorithms that will be adopted throughout the chapter. We will first introduce the optimal MAP detector for the satellite channel, then we will consider lower complexity alternatives.

2.3.1 Optimal MAP Detection: the Chip Detector

The nonlinear transponder and the possible application of the time packing technique (to be detailed later) introduce (nonlinear) ISI on the transmitted signal. Assuming that the system has finite-memory, we can model the modulator, IMUX and OMUX filters, and the HPA as a FSM, whose input is the symbol sequence $\{x_k\}_{k=0}^{K-1}$ and whose output is the signal

$$s(t) = \sum_{k=0}^{K-1} \bar{s}(t - kT_s, x_k, \sigma_k), \tag{2.2}$$

where the term $\bar{s}(t - kT_s, x_k, \sigma_k)$ is assumed to have support on the interval $[kT_s, (k+1)T_s)$ and is thus a "chip" (a slice) of the signal. The state σ_k of the FSM contains the previous L channel inputs, where L is the memory length of the channel:

$$\sigma_k = (x_{k-1}, x_{k-2}, \ldots, x_{k-L}).$$

Therefore, the optimal MAP symbol detector consists of a bank of filters [51] matched to all possible waveforms $\bar{s}(t - kT_s, x_k, \sigma_k)$, followed by a BCJR detector [1]. The complexity of the BCJR algorithm is $\mathcal{O}(M^{L+1})$. In principle, the real channel memory can be much larger than that assumed by the detection algorithm, and hence the choice of L is often dictated by implementation complexity reasons, thus resulting in a suboptimal implementation.

2.3.2 Lower Complexity Detection Algorithms

The chip detector tends to be optimal for $L \to \infty$, independently of the HPA, IMUX, and OMUX characteristics and of the possible application of the time packing technique. However, its complexity for optimal detection becomes soon unmanageable unless proper techniques for complexity reduction are employed. For the sake of clarity, let us just consider, for example, the case of the transmission of a linear modulation with orthogonal signaling on the AWGN channel. It is known that, in this case, the symbol-by-symbol detector is optimal. On the other hand, the chip detector would require a large memory L, since it does not exploit the linear nature of

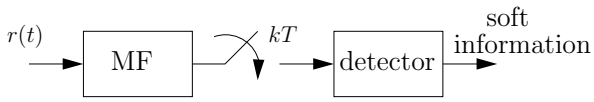

Figure 2.4: Block diagram of the CR.

the received signal and the orthogonality condition. In light of these considerations, it is reasonable to think that the optimal performance achieved by the chip detector may be reached by lower complexity algorithms, using smaller values of L. For this reason, this section introduces other detection algorithms beyond the chip detector. These detectors are still based on a BCJR algorithm, with complexity $\mathcal{O}(M^{L+1})$, but they are expected to achieve performance similar to the chip detector with lower values of L.

Conventional DVB-S2 Receivers

Conventional DVB-S2 receivers are based on a symbol-by-symbol soft detector working on samples at the output of a MF. Throughout the chapter, this receiver will be denoted as conventional receiver (CR), and it will be used as a performance benchmark. A block diagram of the CR is reported in Figure 2.4. The complexity of the symbol-by-symbol detector adopted by the CR is $\mathcal{O}(M)$.

FS-MMSE Receiver

A more sophisticated detection algorithm has been proposed in [52, 53]. At the receiver, a sufficient statistic is extracted by using oversampling at the output of a FE filter [54]. A FS-MMSE equalizer, working at twice the symbol rate, then acts as an adaptive filter, followed by a symbol-by-symbol detector. This detector does not rely on any specific signal model and the receiver is fully adaptive. It has been shown in [52] that a filter with 42 complex taps represents a good trade-off between performance and complexity. Figure 2.5 shows a block diagram of the FS-MMSE receiver. Also in this case, the complexity is $\mathcal{O}(M)$, so this receiver is directly comparable with the CR.

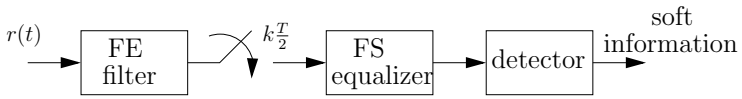

Figure 2.5: Block diagram of the FS-MMSE receiver.

SISO Detection Based on the Volterra Model

A SISO detection algorithm for the nonlinear satellite channel has been proposed in [55], based on the relevant terms of the Volterra series expansion of the nonlinear HPA described in [56]. It is composed of a suitably designed filter, followed by a BCJR algorithm with proper branch metrics, taking into account only a portion L of the actual channel memory. This receiver will be denoted as *SISO Volterra* in the next sections.

Adaptive CS Receiver

An evolution of the FS-MMSE receiver, able to take into account also part of the channel memory, is based on the application of the adaptive CS technique detailed in Section 1.3. The output of the FS-MMSE equalizer is filtered by a properly designed CS filter, and detection is performed by a BCJR detector with branch metrics computed according to the CS algorithm [22]. When the memory length is set to $L = 0$, this receiver becomes equivalent to the FS-MMSE receiver.

We finally point out that all detectors, with the exception of the SISO Volterra, can also be used jointly with a data predistorter (DPD) at the transmitter, such as that proposed in [57] and also investigated in [47], with the aim of pre-compensating the distortions introduced by the HPA. The SISO Volterra receiver, on the other hand, is specifically designed to work in the absence of a DPD because it already takes into account the nonlinear nature of the channel. Moreover, common DVB-S2 receivers usually perform detection and decoding separately, with a pragmatic approach. However, it is well known that performing iterative detection and decoding at the receiver improves the performance with a limited complexity increase. For this reason, we will also analyze the impact of the application of iterative detection and decoding.

2.4 Bandwidth and Symbol Rate Optimization

As mentioned, the DVB-S2 standard [35] foresees the use of RRC pulses with roll-off factors α equal to 0.2, 0.25, or 0.35, and recommends symbol rates of the order of 30 Mbaud. However, as a consequence of the continuous technological evolution, it has been recently considered to increase the symbol rate of DVB-S2 signals despite this could involve a complexity increase. Hence, a joint optimization of the roll-off and symbol rate is required to identify the best working scenario.

For this investigation we will adopt only the CR and the FS-MMSE receivers, in order to gain a first insight on the symbol rate values that can be reached by an improved system, still keeping a receiver complexity comparable to that of conventional systems. We remark that the presence of an equalizer in the FS-MMSE receiver allows the system to better handle the increased distortions and interference arising when working with higher symbol rate values. The transmitter uses the constellations commonly adopted in broadcasting systems, i.e., the M-PSK constellations, with $M = 4, 8$, and the APSK constellations with $M = 16$, foreseen by the DVB-S2 standard [35]. For each case, the input back-off (IBO) of the HPA has been optimized to maximize performance. In particular, it has been set to 0 dB for PSKs and to 3 dB for APSKs.

2.4.1 Numerical Results

In the first optimization step, we address the increase of the symbol rate of the transmitted signal. The performance of the two receivers is evaluated with four symbol rate values: $R_s = 31$ (adopted by common DVB-S2 systems), 34, 37, and 40 Mbaud, all working with the lowest roll-off factor foreseen by the DVB-S2 standard ($\alpha = 0.2$). Figure 2.6 reports the envelope of the ASE of the three modulation formats, for both receivers.[1] The figure shows that CR is unable to support symbol rates higher than 34 Mbaud without significant losses, while FS-MMSE clearly reaches its best performance at 37 Mbaud. The saturation effect in all ASE curves is due to the fact that we

[1] With "envelope" we mean the highest of the three ASE values corresponding to the three modulation formats, for each value of P_{sat}/N.

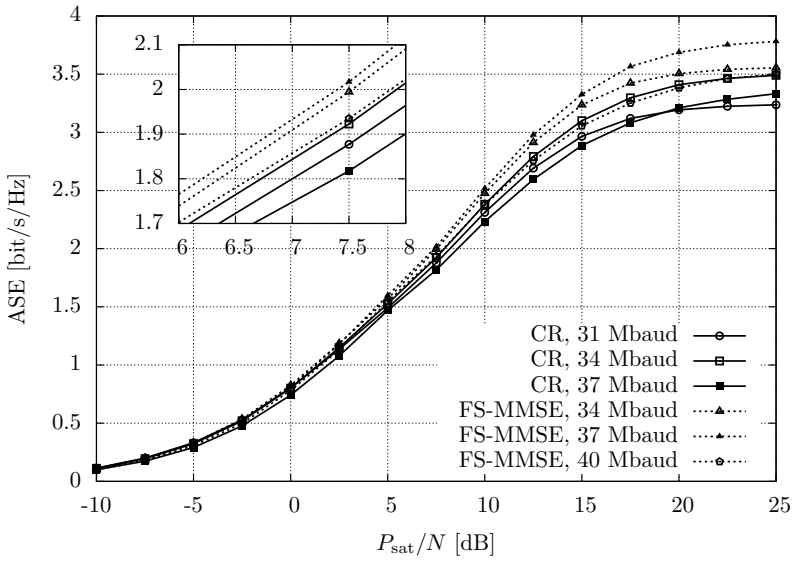

Figure 2.6: ASE for CR and FS-MMSE detectors with $\alpha = 0.2$.

are using finite order constellations.

The next step is to jointly optimize the symbol rate and roll-off factor for the FS-MMSE receiver. The results of this joint optimization are reported in Figure 2.7, for the same symbol rate values as in Figure 2.6. The main conclusion of this analysis is that the optimal setting is to adopt a symbol rate of 37 Mbaud with a roll-off equal to 0.1 or 0.05, which are practically equivalent in performance. To simplify the physical implementation, we select the value $\alpha = 0.1$ (which corresponds to a bandwidth $W = 40.7$ MHz) for the remaining sections of the chapter. Higher symbol rate values should be discarded because, besides a clear performance loss, they would also cause problems related to power dissipation in on-board equipment and to ICI [38].

After this theoretical analysis, we want to verify whether the practical LDPC codes foreseen in [35] can confirm these results. For this purpose, we select four DVB-S2 MODCODs (quadrature phase shift keying (QPSK) with $r = 4/5$, 8PSK with $r = 2/3$ and $r = 3/4$, and 16APSK with $r = 3/4$), and compute their SE. For all schemes, the decoder performs a maximum of 50 iterations, and for the FS-MMSE

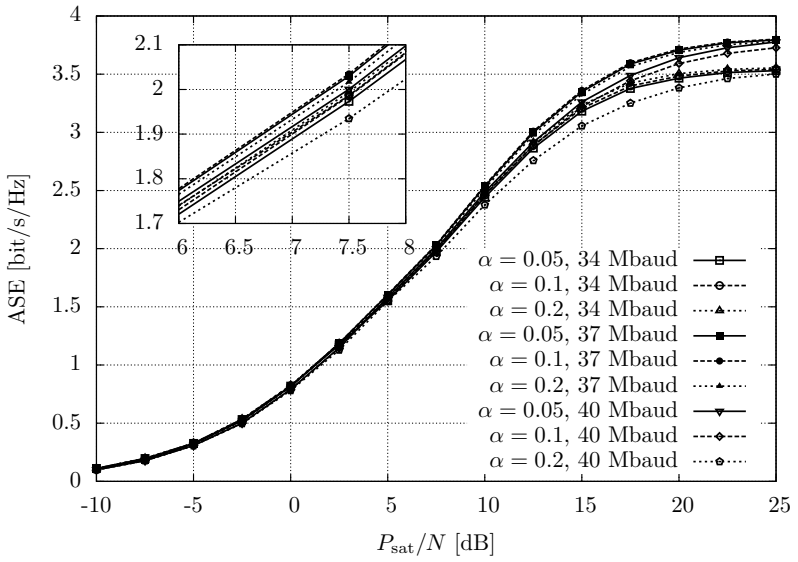

Figure 2.7: Symbol rate and roll-off optimization for the FS-MMSE receiver.

receiver iterations are performed between the detector and the decoder, which are known to potentially give advantages for APSK modulations. No iterations are performed by common DVB-S2 receivers, so this iterative scheme is not applied to the CR. Figures 2.8 and 2.9 show, respectively, the SE achievable by the selected MODCODs when $\alpha = 0.2$ for both receivers, and the SE for different symbol rate and roll-off values for the FS-MMSE receiver. The results are perfectly in line with the information-theoretical analysis, so they confirm that a system with $R_{\mathrm{s}} = 37$ Mbaud and $\alpha = 0.1$ represents the optimal setting even when practical codes are adopted. As far as the transmitted side is concerned, while for CR a static DPD is used for all modulation formats, for the FS-MMSE receiver it is necessary only for APSKs.

Having fixed the transmission parameters to $R_{\mathrm{s}} = 37$ Mbaud and $\alpha = 0.1$, let us now evaluate how the higher complexity detectors perform in this scenario. For this purpose, we will, from now on, take the FS-MMSE receiver with optimized parameters as our reference system. Figures 2.10 and 2.11 show the ASE computed for the considered detectors with 8PSK and 16APSK. The SISO Volterra and FS-MMSE

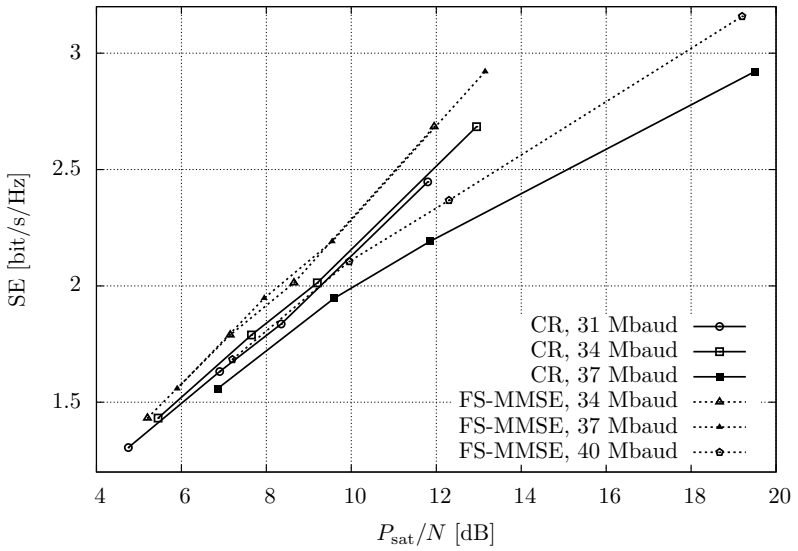

Figure 2.8: SE for CR and FS-MMSE detectors with $\alpha = 0.2$.

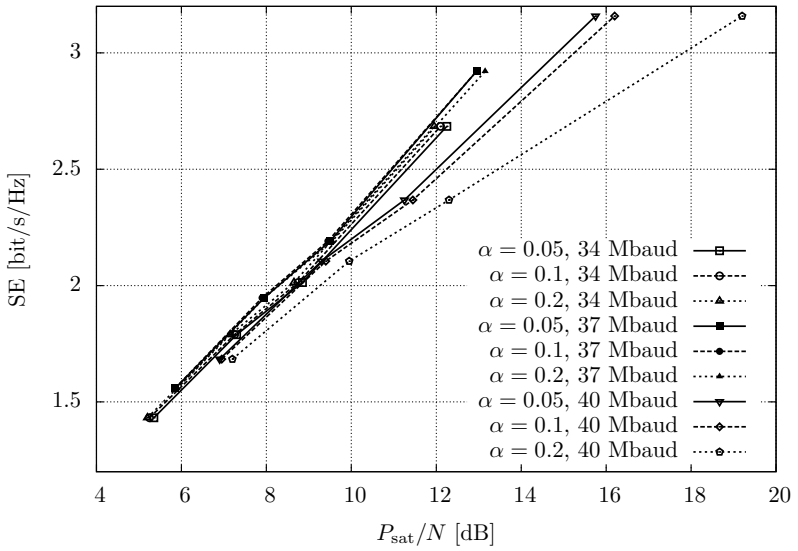

Figure 2.9: SE for the FS-MMSE detector, for different symbol rates and roll-offs.

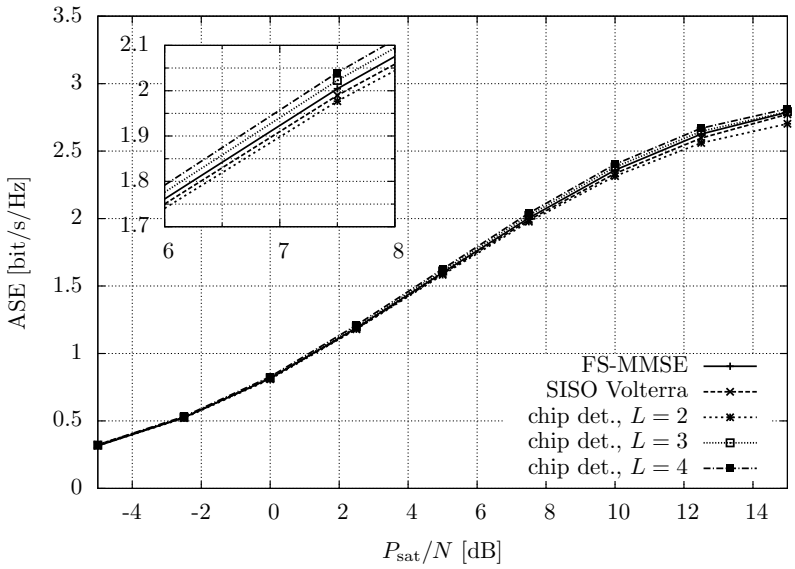

Figure 2.10: ASE for 8PSK with different receivers.

detectors are working on a symbol-by-symbol base ($L = 0$) because we have verified that higher memory values do not improve ASE significantly (namely, the adaptive CS receiver with $L > 0$ has the same performance as the FS-MMSE in this scenario). On the other hand, the chip detector has been tested with increasing values of the memory L until the ASE saturation has been reached (i.e., when two consecutive values of L result in the same ASE). Results show that the lower complexity detectors are practically equivalent and they both reach almost optimal performance. In light of these results, it is worth to point out that the adoption of a properly designed symbol-by-symbol detector is almost optimal, and more sophisticated algorithms cannot provide any performance improvement, independently of the signal model considered at the detector.

As mentioned, the ASE is achievable by receivers performing iterative detection and decoding. However, if iterations are not allowed, a loss is likely to occur. To evaluate this loss, we report in Figure 2.12 the comparison between ASE and pASE for FS-MMSE detector with QPSK, 8PSK, and 16APSK. The distance of approximately

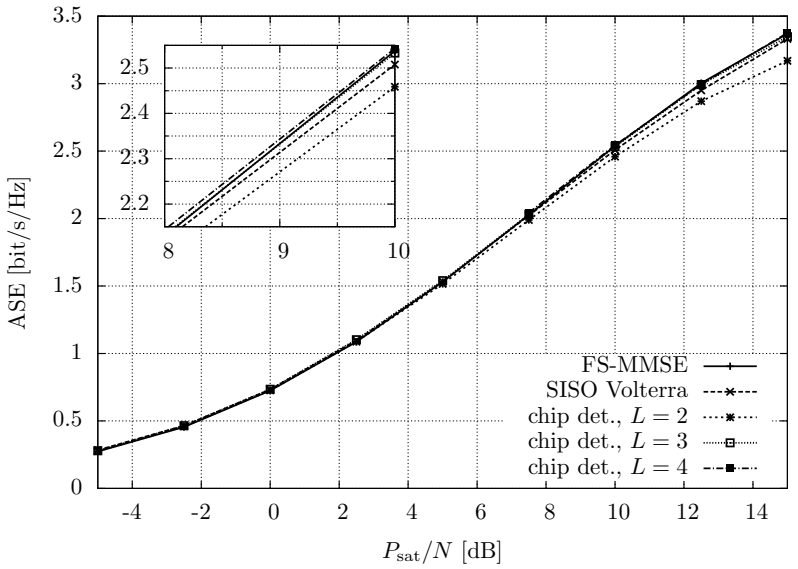

Figure 2.11: ASE for 16APSK with different receivers.

$0.2 \div 0.3$ dB between the ASE and pASE curves for 16APSK means that there is room for an improvement when allowing iterations between detector and decoder. On the other hand, no improvement is expected for QPSK and 8PSK. This is not surprising, since QPSK and 8PSK use a Gray mapping, and thus no gain has to be expected when performing iterations with the detector [58].

2.5 Advanced Optimization Techniques

The aim of this section is to present some possible techniques to improve the SE, that can be applied at the transmitter side. Our aim is to suitably optimize the symbol interval through the application of time packing, and to optimize the adopted constellations and the shaping pulse $p(t)$.

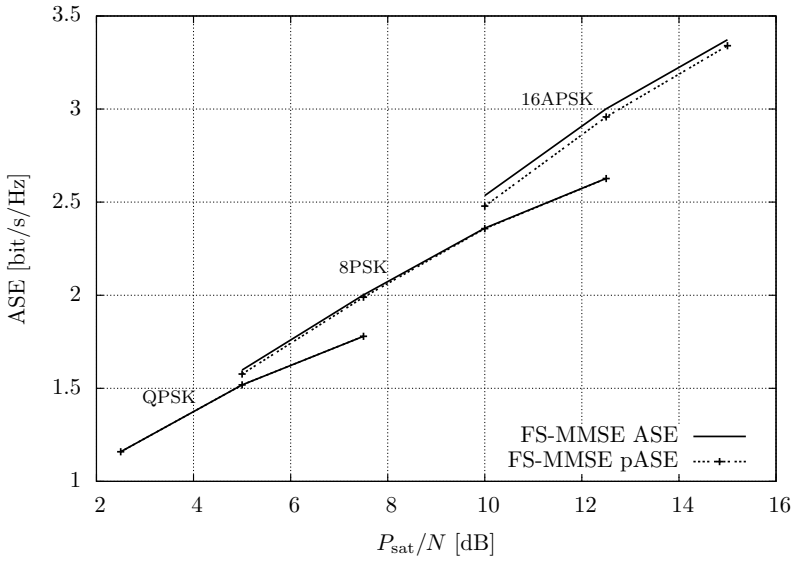

Figure 2.12: ASE and pASE comparison.

2.5.1 Time Packing

The application of time packing to the nonlinear satellite channel has already been considered in [33], but our working scenario is slightly different. In fact, [33] was published before the DVB-S2X standard was developed, and hence it did not consider some aspects of the DVB-S2X channel model [39]. In particular, in [33] the frequency spacing between adjacent transponders has been optimized to maximize the SE, while in this chapter it is fixed to 40 MHz. As a consequence, the bandwidth of the signal is also constrained to about 40 MHz, while in [33] there were no constraints on the bandwidth due to adjacent signals.

The properties of ASE in (2.1) as a function of τ cannot be determined in closed form, but it is clear, by physical arguments, that it is bounded, continuous in τ, and tends to zero when $\tau \to 0$ or $\tau \to \infty$. Hence, ASE has a maximum value, when varying τ. The optimization problem consists of finding the value of τ that results in the maximum ASE; this problem can be studied by evaluating (2.1) performing a coarse search on the values of τ.

2.5.2 Constellation and Shaping Pulse Optimization

As far as the constellation is concerned, the optimization algorithm that allowed us to obtain the best performance is a variant of the classical gradient descent (GD) algorithm [59], which has been used to solve the following optimization problem:

$$\mathcal{X}^* = \arg\max_{\mathcal{X}:\|\mathcal{X}\|=M} I_R(\mathcal{X}),$$

in which we have explicitly pointed out the dependence of the information rate I_R on the constellation.

The steps of the GD algorithm can be summarized as follows.

1. Choose randomly M points in the complex plane, with the only constraint that they must form an energy-normalized constellation called $\mathcal{X}_0$, i.e.,

$$\frac{\sum_{c_i \in \mathcal{X}_0} |c_i|^2}{M} = 1. \tag{2.3}$$

   Then set $\mathcal{X}^* = \mathcal{X}_0$ and compute $I_R^* = I_R(\mathcal{X}_0)$.

2. At each iteration $\ell = 1, 2, \ldots$ of the GD algorithm, choose randomly one of the M points of $\mathcal{X}_{\ell-1}$ and move it to an adjacent free point (where adjacent means on an adjacent vertex of a square grid whose steps are equal to the step size of the GD) to form the new constellation $\mathcal{X}_\ell$; then normalize $\mathcal{X}_\ell$ according to (2.3).

3. Compute $I_R(\mathcal{X}_\ell)$. If $I_R(\mathcal{X}_\ell) > I_R^*$, set $I_R^* = I_R(\mathcal{X}_\ell)$ and $\mathcal{X}^* = \mathcal{X}_\ell$, otherwise set $\mathcal{X}_\ell = \mathcal{X}_{\ell-1}$. Go to step 2.

This optimization algorithm has been run until convergence, i.e., until no improvement in the information rate has been achieved for a certain number of iterations. Since the exact shape of the function $I_R(\mathcal{X})$ is unknown for the case of interest, the optimization process must avoid being trapped in some local maximum. Therefore, we have performed the optimization by running several parallel instances of the GD algorithm, each starting from a different random constellation. The best solution, in

terms of information rate, among all instances has then been selected as the overall maximum. In this way, the procedure becomes a *multistart* GD algorithm.

The optimization of the constellation is a complex procedure, requiring a great amount of memory and thousands of iterations to converge to a good solution. When using the chip detector with high values of the constellation cardinality and of the memory L, the optimization process requires many days of simulation on a workstation. We could avoid this problem with the use of the FS-MMSE receiver, which works on a symbol-by-symbol base and significantly reduces the memory requirements to achieve the final result. The optimized constellations can then be used with every kind of detector. Once again, the optimization has been performed taking into account the full DVB-S2X satellite channel model described in [39].

A further optimization step has been attempted by applying a similar procedure to the shaping pulse $p(t)$: we have expressed the information rate I_R as a function of $p(t)$, and we have applied the GD algorithm to each sample of the pulse. However, the high number of samples of a pulse makes the computation unfeasible for values of $M > 4$, and even with a QPSK the operation is very slow and there is no guarantee that it will converge to a good solution. The attempts to optimize the pulse did not bring any advantage to the spectral efficiency of the system. We also attempted the use of different kinds of pulses, like raised cosine or Gaussian pulses, but they have shown no gain with respect to the classical RRC pulse. Hence, the design of an optimized shaping pulse for the satellite channel remains an open issue.

To conclude the analysis of the optimization techniques, we point out that we have attempted a joint optimization of the constellations/shaping pulses in the presence of time packing. However, due to the high complexity of this joint optimization problem, we could obtain only partial results, whose advantages are too limited to be of any interest. As an example to give an insight on the complexity of the problem, it is worth mentioning that the optimized pulses result to be very sensitive to the memory L and to the time packing factor τ. This means that an optimized pulse for some values of L and τ can be highly suboptimal for other values. Hence, a good pulse optimization should be performed for several values of L and τ, and for different constellations, but this has not been possible due to the high complexity of the problem.

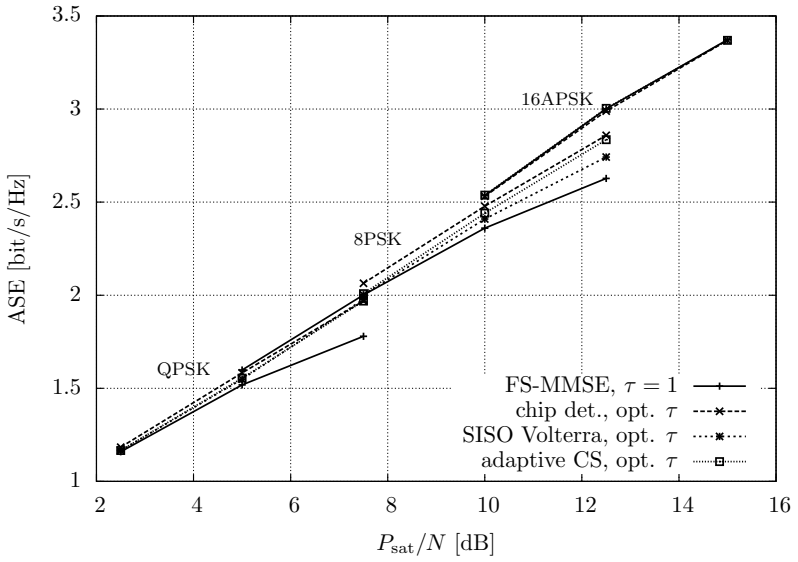

Figure 2.13: ASE for all described detectors when time packing is employed.

2.5.3 Numerical Results

This section presents the results obtained with the application of the described advanced optimization techniques. Figure 2.13 shows the ASE computed with optimized values of τ for the three alternative detectors and for the three modulation formats of interest. The considered memory for all detection algorithms is, for complexity reasons, $L = 5$ for QPSK and 8PSK, and $L = 4$ for 16APSK. From this figure, we see that for QPSK the three detection schemes are quite equivalent, and time packing provides a gain in terms of ASE of approximately 14% at $P_{\mathrm{sat}}/N = 7.5$ dB with respect to orthogonal signaling. However, considering this result alone is misleading: at the selected P_{sat}/N value, QPSK is no longer the optimal constellation, and by switching to 8PSK this gain disappears. In case of 8PSK, the chip detector exhibits a gain of approximately 5% at $P_{\mathrm{sat}}/N = 10$ dB and it slightly outperforms the other two detectors. However the same conclusions as for QPSK apply, since 16APSK outperforms 8PSK at this P_{sat}/N value. Finally, for 16APSK modulation, time packing is unable to provide any gain.

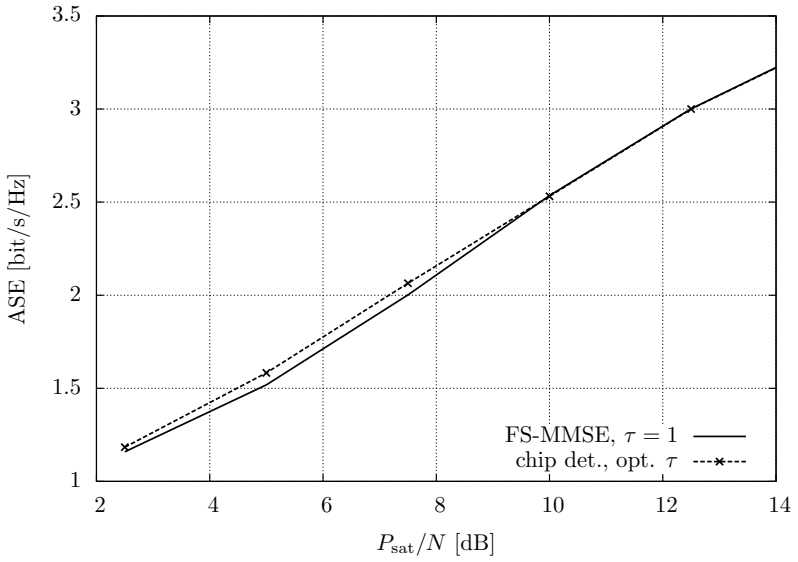

Figure 2.14: ASE envelope in case of optimized time packing and the chip detector.

Figure 2.14 compares the envelope of the chip detector ASE curves in Figure 2.13 with orthogonal signaling. This figure shows that the potential of time packing on the satellite channel is very limited. In fact, for medium-high P_{sat}/N values, 16APSK with $\tau = 1$ outperforms time packing. The main conclusion of this analysis is that the benefits of time packing are too limited, and only at low P_{sat}/N, to justify the complexity increase necessary to apply this technique. As a final note, with respect to [33], the adopted detection algorithm has a better trade-off between complexity and performance. Despite this, time packing is still unable to give advantages in this scenario.

One may wonder whether this result is due to the excessively small memory assumed by the detector and whether the time packing technique can provide a gain when the detector complexity is further increased. In order to evaluate this aspect, we have compared the signal (2.2) provided by the FSM model with the actual useful signal. In fact, the optimality of the chip detector is related to the accuracy of the signal model assumed by the detector itself. Figure 2.15 shows the MSE between the

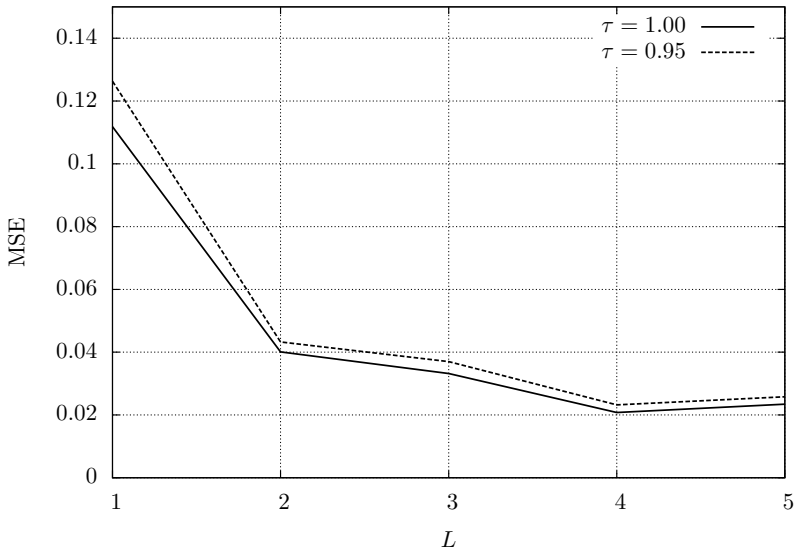

Figure 2.15: MSE between the actual signal and that considered by the chip detector.

actual useful component of the received signal, and the waveform (2.2) considered by the chip detector. The MSE is shown as a function of the memory L considered at the receiver. The adopted modulation is 16APSK, with orthogonal signaling and time packing with $\tau = 0.95$. We see from the figure that the MSE with $\tau = 0.95$ reaches a floor for $L = 4$. This suggests that the chip detector with $L = 4$ is almost optimal also for $\tau = 0.95$, hence the ASE of 16APSK modulation cannot be improved by increasing the receiver complexity. Similar conclusions can be drawn for the other modulation formats. For these reasons, time packing will not be considered anymore in the rest of the chapter, and for the same reasons it has been discarded in the standardization process of DVB-S2X. However, the reader has to consider that, in practice, a sort of surrogate of time packing has already been introduced with the optimization of W. In fact, by increasing the value of W, ISI is increased as well [33].

Having discarded time packing as a possible solution, for the next steps we will use only the FS-MMSE receiver, which, as we have shown, offers the best trade-off between performance and complexity. After this analysis, we have considered the

application of the constellation optimization algorithm described previously to the cases of $M = 4, 8, 16$, obtaining the following results (independently of the IBO).

1. In the case $M = 4$, the optimal constellations converges almost perfectly to a classical QPSK.

2. In the case $M = 8$, the optimized constellations results to be 8PSK at low P_{sat}/N and 1+7APSK at high P_{sat}/N, being 1+7APSK composed of a point in the origin of the complex plane and seven points equally spaced on a circle. This behavior is clear from Figure 2.16, which plots the ASE for the two modulation formats for their best IBO (0 dB for 8PSK and 3 dB for 1+7APSK).

3. In the case $M = 16$, the algorithm converges to 3+13APSK for the P_{sat}/N values of interest.[2] However, when the signal is predistorted, the classical 16APSK provides the best results, thus there is no need to replace that constellation. This behavior is clear from Figure 2.17, which reports the ASE for the two constellations, without and with the application of the static DPD described in [57] at the transmitter.

Figures 2.18 and 2.19 show the two optimized constellations for the cases of $M = 8$ and $M = 16$, together with the corresponding ideal 1+7APSK and 3+13APSK. Apart from random phase rotations, we notice a very good correspondence between the simulation results and the ideal constellations adopted for the computation of the ASE.

In order to confirm the information theoretic analysis, we have simulated the PER of MODCODs employing the DVB-S2 LDPC codes with blocklength 64800 bits [35] and the LDPC codes with the same length, introduced in DVB-S2X [37]. In Figure 2.20 the PER is evaluated for 8PSK and 1+7APSK, using the DVB-S2X codes with rates r equal to $11/20$, $104/180$, $18/30$, and $20/30$ foreseen by [37]. These results perfectly confirm the theoretical curves shown in Figure 2.16, with 1+7APSK that tends to outperform 8PSK for P_{sat}/N greater than about 6.5 dB.

[2] It is interesting to notice that the number of points of the inner circle tends to increase with P_{sat}/N, as already pointed out in [45] for different scenarios. However these P_{sat}/N values are not of interest for the problem considered here.

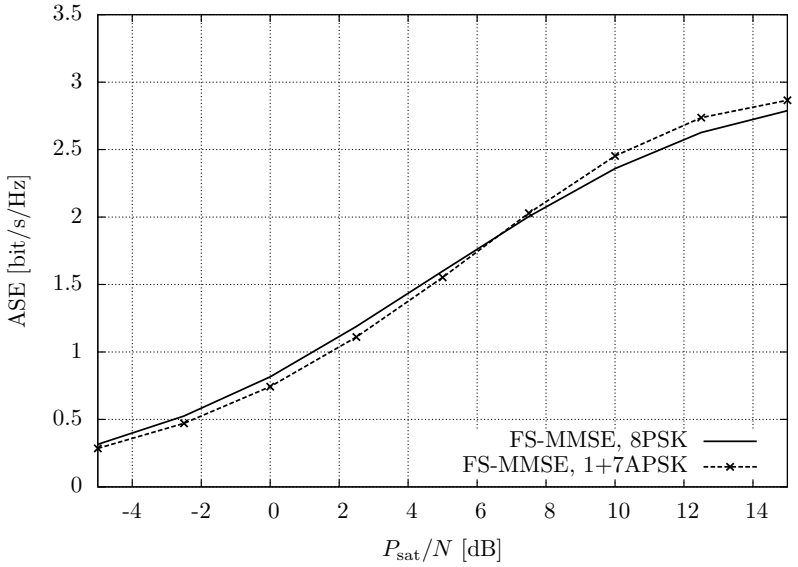

Figure 2.16: ASE comparison between 8PSK and 1+7APSK.

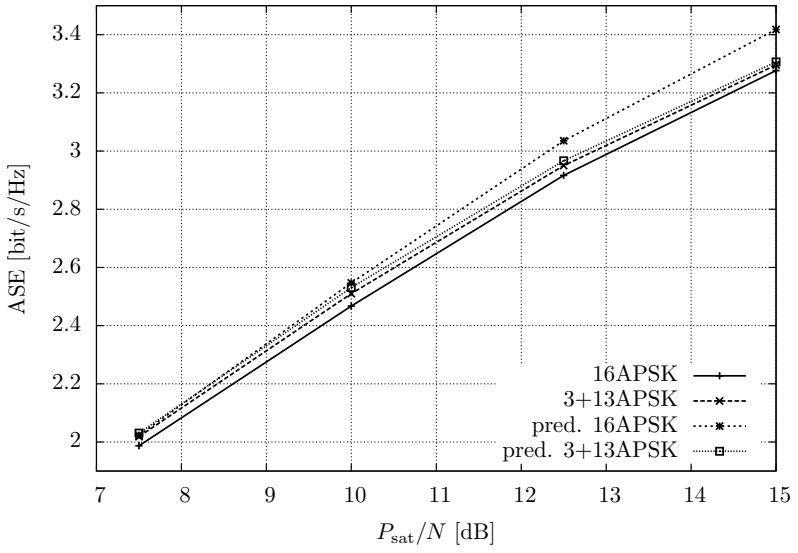

Figure 2.17: ASE comparison with predistortion for constellations with $M = 16$.

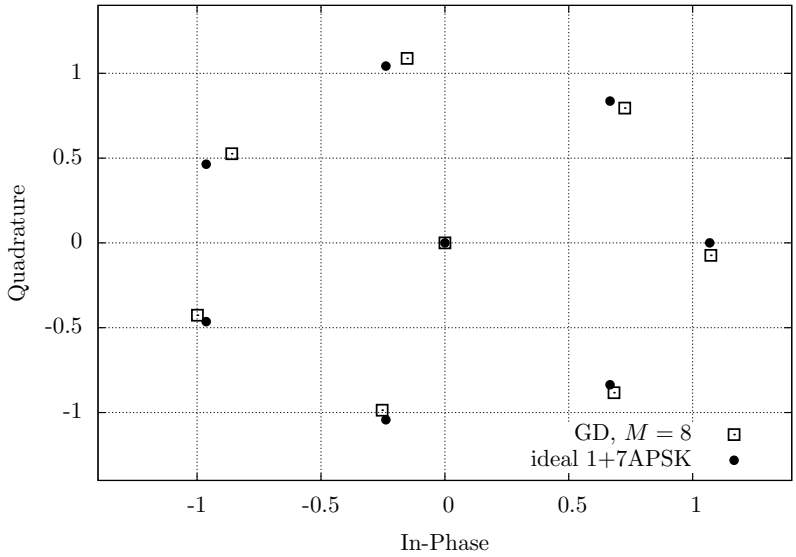

Figure 2.18: GD output and ideal 1+7APSK constellation.

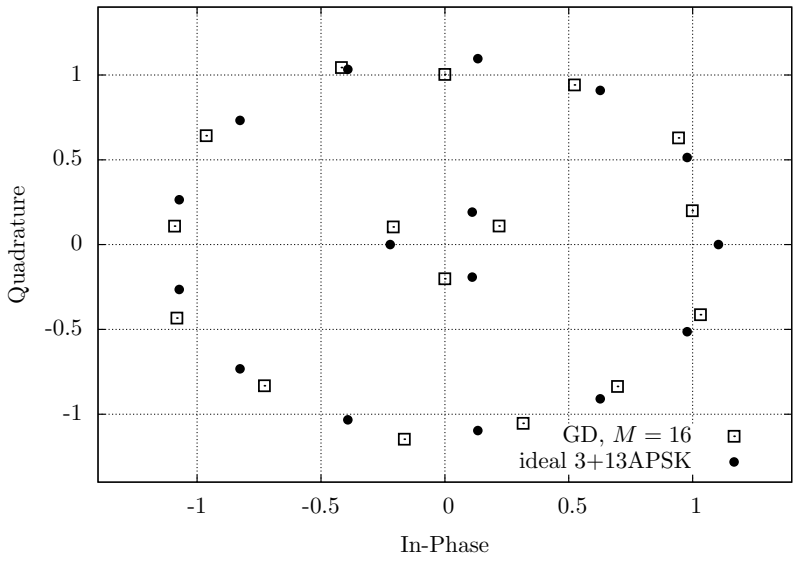

Figure 2.19: GD output and ideal 3+13APSK constellation.

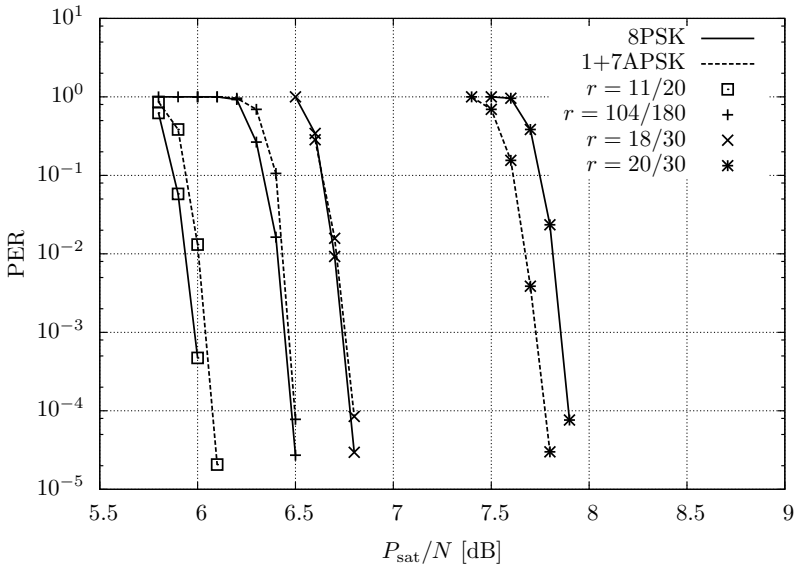

Figure 2.20: PER for DVB-S2X codes, with 8PSK and 1+7APSK, with the FS-MMSE detector.

Finally, we summarize the tested practical MODCODs in Figure 2.21, where the arrows point to the first MODCOD using the corresponding modulation format (for each curve, the points before the first arrow are obtained with QPSK). The first two curves represent the spectral efficiency for MODCODs with DVB-S2 codes. As expected, performing iterations between detector and decoder (continuous line) allows about 0.2 dB gain with respect to the absence of iterations (dashed line) for 16APSK only. Then, we see than the DVB-S2X codes always gain with respect to DVB-S2. The gains are due in part to an improvement in the code design, but mainly to the higher granularity that allows to better cover the spectral efficiency plane, especially the P_{sat}/N regions corresponding to modulation changes (for example, $9 \div 11$ dB). To conclude the analysis, for some MODCODs, the adoption of 1+7APSK allows a further gain of about $0.1 \div 0.2$ dB. The SE achieved by MODCODs shown in Figure 2.21 is reported in Tables 2.1 and 2.2.

P_{sat}/N [dB]	SE [bit/s/Hz]	Mod.	Rate
5.05	1.4605	QPSK	3/4
5.65	1.5579	8PSK	96/180
5.95	1.6066	8PSK	11/20
6.05	1.6228	8PSK	100/180
6.45	1.6877	8PSK	104/180
6.75	1.7526	8PSK	3/5
7.85	1.947	8PSK	2/3
9.05	2.1637	16APSK	100/180
9.5	2.2503	16APSK	104/180
10.35	2.42	16APSK	28/45 *
10.7	2.5099	16APSK	116/180 *
11.05	2.5965	16APSK	2/3 *
11.7	2.7047	16APSK	25/36 *
12.85	2.921	16APSK	3/4 *

Table 2.1: DVB-S2X MODCODs (* means iterations between detector and decoder).

P_{sat}/N [dB]	SE [bit/s/Hz]	Mod.	Rate
7.75	1.947	1+7APSK	2/3
8.6	2.1096	1+7APSK	13/18
9.05	2.1908	1+7APSK	3/4
9.55	2.2719	1+7APSK	140/180

Table 2.2: DVB-S2X MODCODs with the proposed optimized constellation.

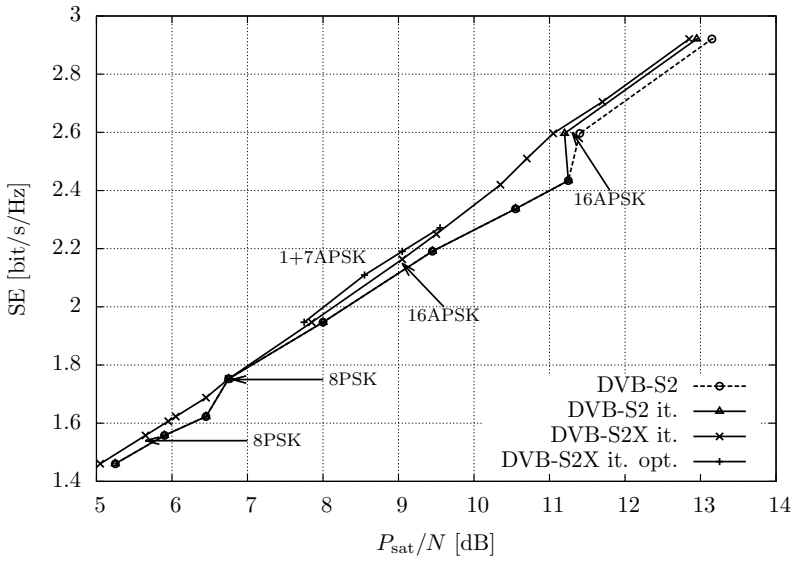

Figure 2.21: Tested practical MODCODs.

2.6 Conclusions

In this chapter, we have addressed the design of an efficient transceiver scheme for DVB-S2X systems. Several optimization steps have been performed both at the transmitter and at the receiver. At the transmitter side, these include the selection of the optimal symbol rate and signal bandwidth, the design of new constellations and the application of the time packing technique. At the receiver side, instead, we have tested several detection algorithms with different degrees of complexity.

Furthermore, we have assessed the performance of the recently proposed DVB-S2X LDPC codes and evaluated the advantages of the application of iterative detection and decoding.

The main results of the investigation can be summarized as follows. An optimized DVB-S2X system should use RRC-shaped pulses with roll-off equal to 0.1, transmitted at a symbol rate of 37 Mbaud. At the receiver, a simple FS-MMSE equalizer followed by a symbol-by-symbol detector grants an excellent performance even compared with detectors taking into account a part of the channel memory. The new

LDPC codes provide a very good coverage of the SNR range of interest in broadcasting applications, and applying iterative detection and decoding allows to achieve gains with only a limited complexity increase. Finally, while the application of time packing is not convenient in this scenario, we have shown that a properly designed constellation can give further (limited) advantages.

We have evaluated both the theoretical performance, in terms of ASE, and the SE of practical MODCODs, showing a strong agreement between them.

Chapter 3

Analysis of Multiple Satellites Broadcasting Systems

In today's satellite communication systems, the scarcity of frequency spectrum and the ever growing demand for data throughput has increased the need for resource sharing. In recent years, users of professional broadcast applications such as content contribution, distribution, and professional data services have demanded more spectrally efficient solutions.

Satellite service providers often have the availability of *co-located* satellites: two (or more) satellites are said to be co-located when, from a receiver on Earth, they appear to occupy the same orbital position. Co-location of satellites is typically used to cover the fully available spectrum by activating transponders on different satellites that cover non-overlapping frequencies or as a stand-by in-orbit redundancy, when the backup satellite is activated in case of failure of the main satellite. However, the second satellite can also be exploited to try to increase the capacity of the communications link.

In this chapter, we address a scenario in which the backup satellite is activated in addition to the main one, to improve the ASE of the overall communication system. The transmission from the two satellites can be coordinated, but through simple geometrical considerations it can be easily shown that even with a coverage area of

a few tens of kilometers and two co-located signals separated in angle by a fraction of degree, time alignment is not possible. On the other hand, the considered system model can also represent a scenario where a single satellite with two transponders operating at the same frequency is employed and hence the two transmitted signals can be considered synchronous.

Here, we study the AIR of a system where the two satellites transmit on overlapping geographical coverage areas with overlapping frequencies, and compare our results with that achievable by the frequency division multiplexing (FDM) strategy and with that achievable adopting the well known Alamouti space-time block code [60].

The two-satellites scenario has been studied in [61, 62], where the satellite channel is approximated as a linear AWGN channel, and the information theoretic analysis has been carried out under the limiting assumption of Gaussian inputs. We instead examine three different models for the system: the linear AWGN channel, the peak-power-limited AWGN channel [63–65], and the satellite channel adopted in the DVB-S2 standard [35]. The studied system is an instance of broadcast channel [66–69] with multiple transmitters. However, we are interested in a scenario in which the same information must be sent to every receiver. This situation corresponds, for example, to the delivery of a television broadcast channel. We show that all these scenarios can be analyzed by means of network information theory and we will resort to multiple access channels (MACs) [66, 70] with proper constraints.

Our analysis reveals that, if we allow multiuser detection, the strategy based on overlapping signals achieves higher ASEs with respect to that achievable by using FDM. Interestingly, we show that there are cases in which a single satellite can outperform both these multiple satellites strategies, but not the Alamouti scheme.

The remainder of this chapter is structured as follows: in Section 3.1 we present a general system model valid for all cases, and in Section 3.2 we briefly review the theory of MACs. In Sections 3.3 and 3.4 we discuss the achievable rates by FDM and by the Alamouti space-time code. In Sections 3.5, 3.6, and 3.7 we analyze the three different channel models. Finally, in Section 3.8 we investigate the performance of practical MODCODs for this scenario, and Section 3.9 concludes the chapter.

3.1 System Model

Figure 3.1 depicts a schematic view of the baseband model we are considering. A single operator properly sends two separate data streams to the two satellites. The impact of the feeder uplink interference is considered negligible in this scenario. Data streams are linearly modulated signals, expressed as

$$x_i(t) = \sum_k x_k^{(i)} p(t - kT) \quad i = 1, 2, \tag{3.1}$$

where $x_k^{(i)}$ is the k-th symbol transmitted on data stream i, $p(t)$ is the shaping pulse, and T is the symbol time.

Each satellite, then, relays the signal, denoted as $s_i(t)$,[1] to several users scattered in its coverage area. For each user, the received signal is the sum of the two signals coming from the satellites, with a possible power unbalance γ^2 due to a different path attenuation (we assume $1/2 \leq \gamma \leq 1$). Without loss of generality, we assume that the attenuated signal is $s_2(t)$, otherwise we can exchange the roles of the two satellites. The received signal is also affected by a complex AWGN process $w(t)$ with power spectral density N_0. As mentioned, time alignment between the signals transmitted by the two satellites is not possible. In fact, if the signals from the two satellites come perfectly aligned at a given receiver in the area, there will be other receivers for which a misalignment of a few symbols is observed. On the other hand, it is straightforward to show that our information-theoretic analysis does not depend on the time alignment of the two signals, and we will assume synchronous users to simplify the exposition. Hence, the received signal has the following expression

$$y(t) = s_1(t) + \gamma e^{j\phi(t)} s_2(t) + w(t), \tag{3.2}$$

where $s_1(t)$ and $s_2(t)$ are the signals at the output of the two satellites, and $\phi(t)$ is a possible phase noise process, caused by the instabilities of the oscillators. We assume that the phase noise is slowly varying with respect to the signals' symbol rate and perfectly known at the receiver. Signals $s_1(t)$ and $s_2(t)$ are transmitted with overlapping frequencies, and the overall signal has bandwidth W.

[1] It can be $s_i(t) \neq x_i(t)$ due to the nonlinear transformation at the satellite transponder.

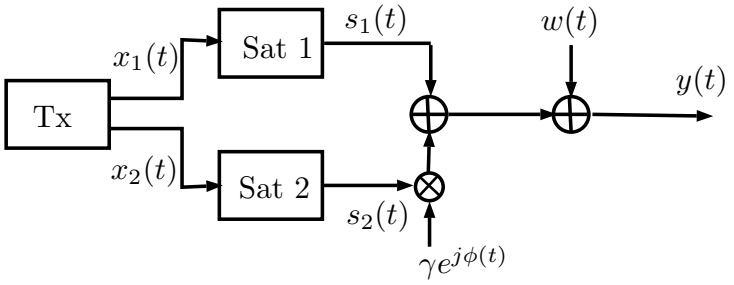

Figure 3.1: Block diagram of the analyzed system.

Since we are analyzing a broadcast scenario in which different receivers experience different (and unknown) levels of power unbalance, we impose that the two satellites transmit with the same rate. This constraint will be better clarified in the next sections. Channel state information is not available at the transmitter and no cooperation among the users is allowed. This is because the target is on broadcasting applications.

A simple alternative strategy to overlapping frequencies, that allows to avoid interference between the two transmitted signals, is FDM. The bandwidth W is divided into two equal subbands, that are assigned to the different satellites. An unequal subband allocation does not make sense since the power unbalance is different for different receivers in the coverage area and, in any case, unknown to the transmitter. In this case, the received signal has expression

$$y(t) = s_1(t)e^{j\pi f_c t} + \gamma e^{-j\pi f_c t + j\phi(t)} s_2(t) + w(t)\,, \tag{3.3}$$

where f_c is the frequency separation between the two signals.

Another possible alternative to avoid interference between the two signals is the use of the Alamouti space-time block code [60], consisting in the two satellites exchanging the transmitted signals in two consecutive transmissions. Unlike the two previous strategies, its classical implementation requires a perfect alignment in time of the signals received from the two satellites. However, an alternative implementation working in the presence of a delay which can be different for different receivers is described in [71].

As in Chapter 2, these transmission strategies will be compared by using the overall ASE of the system as a figure of merit. In this scenario, the ASE is defined as

$$\text{ASE} = \frac{I_R}{TW} \quad [\text{bit/s/Hz}],$$

where I_R is the maximum AIR of the channel. However, since in the scenario of interest the values of T and W are fixed, without loss of generality we will assume that the product $TW = 1$ and we will refer to the terms AIR and ASE interchangeably.

3.2 Achievable Rates in a MAC

In this section, we review some results on classical MACs [66]. We consider the transmission of independent signals from the two satellites.[2] We denote by R_1 the ASE of the first satellite and by R_2 that of the second satellite. At this point, we make no assumptions on the channel inputs, since a better characterization of the input distributions is presented in the next sections. However, independently of the form assumed by the input distribution, the boundaries of the ASE region can be expressed, for each fixed SNR, as [66]

$$\begin{aligned} R_1 &\leq I(x_1;y|x_2) \triangleq I_1 \\ R_2 &\leq I(x_2;y|x_1) \triangleq I_2 \\ R_1+R_2 &\leq I(x_1,x_2;y) \triangleq I_{\text{J}}\,, \end{aligned}$$

where $I(x_1;y|x_2)$, $I(x_2;y|x_1)$, and $I(x_1,x_2;y)$ represent the mutual information between x_1 and y conditioned to x_2, that between x_2 and y conditioned to x_1, and that between the couple (x_1,x_2) and y, respectively; we have omitted the dependence on t and adopted the definitions I_1, I_2, and I_{J} to simplify the notation.

Figure 3.2 is useful to gain a better understanding of the behavior of ASE regions. Point D corresponds to the maximum ASE from satellite 1 to the receiver when satellite 2 is not sending any information. Point C corresponds to the maximum rate at

[2] We will explain later, in Section 3.5, why this is the best choice for the signals transmitted from the two satellites.

which satellite 2 can transmit as long as satellite 1 transmits at its maximum rate.[3] The maximum of the sum of the ASEs, however, is obtained on points of the segment B-C; these points can be achieved by joint decoding of both signals. It does not make sense to adopt different rates for the two satellites, since each satellite ignores whether its signal will be attenuated or not and this attenuation will vary for different receivers. As a consequence, the only boundary point of the ASE region we can achieve is point E, which lies on the line $R_1 = R_2$. As the power increases and/or the power unbalance decreases, the rates increase and the shape of the spectral efficiency region tends to become more symmetric. As a result of these changes of the region, point E can be found in different positions of the boundary, on both segments A-B and B-C (E on the middle point of B-C corresponds to the absence of power unbalance and to a perfectly symmetric region). We can distinguish three significant rate regions in which E can be found.

1. Point F has coordinates $(I_1 - I_2, I_2)$ and aggregate sum-rate equal to I_1. When E falls in the region to the left of F (segment A-F), the total sum-rate of the channel is $2I_2$. Since in this region $I_1 > 2I_2$, it is convenient to use a single transmitter with rate I_1, rather than activating the second satellite.

2. Point B has coordinates $(I_J - I_2, I_2)$ and aggregate sum-rate I_J. When E is in the region between F and B, this still corresponds to a total sum-rate equal to $2I_2$, but now we have $I_1 < 2I_2$, so there are gains over the single satellite case. However, the system still does not reach the highest achievable sum-rate I_J.

3. Finally, when E is on the right of B, i.e., on segment B-C, the system reaches its highest achievable sum-rate I_J.

In light of these considerations, the sum-rate of the channel, under the constraint of equal rates for both transmitters, is defined as a "practical" sum-rate, and denoted as $I_{J,p}$. It is easy to see, through graphical considerations, that

$$I_{J,p} = \min(I_J, 2I_2)\,.$$

[3] If we exchange the role of the two satellites, the same considerations hold for points A and B instead of D and C.

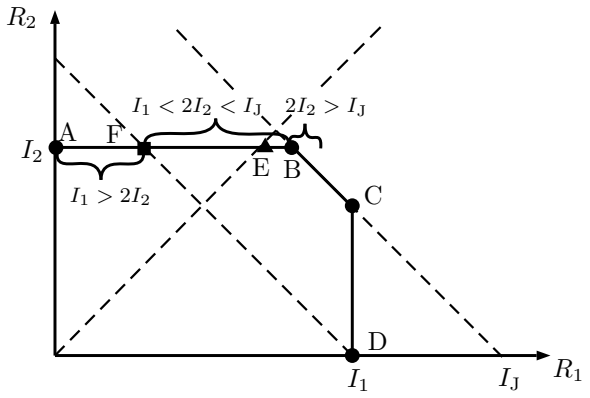

Figure 3.2: Achievable rates region in the case $I_2 < I_1$.

We can also conclude that there are cases in which it is not convenient to use two transmitters.

In Figure 3.3 we report three qualitative examples of ASE regions. As mentioned, the maximum rate we can achieve corresponds to the intersection of the black dashed line with the ASE region (denoted as points A, B, and C in the figure), and points D, E, and F correspond to a transmission with overall rate equal to I_1. In red, point A falls in the first region, so in this case it is more convenient to use a single satellite rather than activating both transmitters. In green, point B is in the second region, so it reaches a rate higher than I_1 but lower than I_J. In blue, point C is on the diagonal boundary of the region, so the sum-rate of the channel is I_J, the highest achievable by the system. Hence, from the study of the ASE region, it is immediate to understand when it is convenient to activate the second satellite and when the system can reach the maximum sum-rate achievable on the channel.

3.3 Achievable Rates by FDM

Since the two signals transmitted by the FDM model (3.3) operate on disjoint bandwidths, they are independent and the AIR of this system is equal, in case $\gamma = 1$, to that of a single transmitter with double SNR. We define by I_{FDM} the rate achiev-

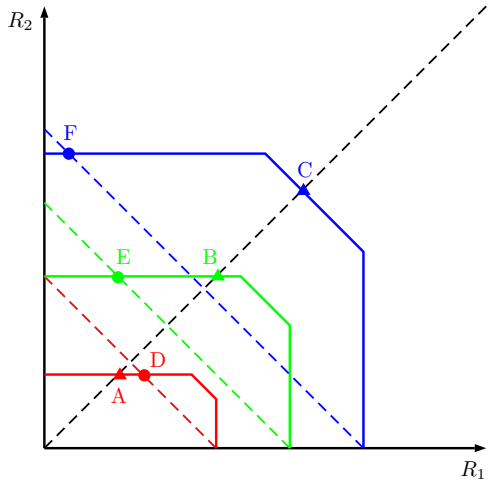

Figure 3.3: Examples of spectral efficiency regions.

able by FDM, and by $I_{\text{FDM,p}}$ that achievable by FDM under the equal rate constraint. The latter is clearly equal to twice the minimum ASE of the two subchannels. We demonstrate that the rate achievable by FDM is always lower than or equal to that achievable with two signals with overlapping frequencies in the absence of nonlinear distortions; the same result holds for the practical rates and can be stated in the following theorem.

Theorem 1. *Let us consider the ideal multiple access channel*

$$y(t) = x_1(t) + \gamma x_2(t) + w(t)\,. \tag{3.4}$$

The following inequalities hold

$$I_{\text{J}} \geq I_{\text{FDM}} \tag{3.5}$$

$$I_{\text{J,p}} \geq I_{\text{FDM,p}} \tag{3.6}$$

with equality if and only if $x_1(t)$ and $x_2(t)$ are Gaussian random processes and $\gamma^2 = 0$ dB.

For the proof, we first need a preliminary result concerning the differential entropies of two continuous random variables.

Lemma. *Let x and y be two independent continuous complex random variables, with PDFs $p(x)$ and $p(y)$ and differential entropies $h(x)$ and $h(y)$. Then*

$$h(x+y) \geq 1 + \frac{h(x)+h(y)}{2} \tag{3.7}$$

with equality if and only if x and y are independent Gaussian random variables with the same variance.

Proof. For the entropy power inequality [72, 73]

$$\begin{aligned} 2^{h(x+y)} &\geq 2^{h(x)} + 2^{h(y)} && (3.8) \\ &= 2^{1+\frac{h(x)+h(y)}{2}} \cosh\left(\frac{h(x)-h(y)}{2}\ln 2\right) \\ &\geq 2^{1+\frac{h(x)+h(y)}{2}} && (3.9) \end{aligned}$$

where equalities in (3.8) and (3.9) hold if and only if x and y are Gaussian and have the same variance. Eq. (3.7) is finally derived by taking the logarithm of (3.9). □

We then consider the rates achievable by FDM. Under the assumption of ideal FDM transmission, a sufficient statistic is obtained by sampling the continuous waveforms. The observables for the two subchannels are

$$y_1 = x_1 + w_1 \tag{3.10}$$

$$y_2 = \gamma x_2 + w_2 \tag{3.11}$$

where x_1 and x_2 are the signal samples, w_1 and w_2 are white Gaussian noise processes with power $N/2$ instead of N, since FDM works with half the bandwidth with respect to the case of a single transmitter. The mutual information of FDM is the average of the mutual information for the two channels, i.e.,

$$I_{\text{FDM}} = \frac{h(y_1)+h(y_2)}{2} - \log_2\left(\pi e \frac{N}{2}\right),$$

and the practical rate is

$$I_{\text{FDM,p}} = h(y_2) - \log_2\left(\pi e \frac{N}{2}\right).$$

Since the mutual information is a non decreasing function of the SNR [74], clearly it is $I_{\mathrm{FDM,p}} \leq I_{\mathrm{FDM}}$.

We finally prove Theorem 1.

Proof. We first prove inequalities (3.5) and

$$2I_2 \geq I_{\mathrm{FDM,p}}\,. \tag{3.12}$$

The samples at the output of channel (3.4) can be equivalently expressed as $y = y_1 + y_2$ and the mutual information of this equivalent expression reads $I_{\mathrm{J}} = h(y_1 + y_2) - \log_2(\pi eN)$. Hence,

$$I_{\mathrm{J}} - I_{\mathrm{FDM}} = h(y_1 + y_2) - \frac{h(y_1) + h(y_2)}{2} - 1$$

from which, by an application of the Lemma, we derive inequality (3.5). The mutual information I_2, instead, reads

$$\begin{aligned} I_2 &= h(y|x_1) - \log_2(\pi eN) \\ &= h(y_2 + w_1) - \log_2(\pi eN) \end{aligned}$$

and

$$2I_2 - I_{\mathrm{FDM,p}} = 2h(y_2 + w_1) - h(y_2) - \log_2(2\pi eN)$$

which becomes (3.12) from Lemma.

Since $I_{\mathrm{J,p}} = \min(I_{\mathrm{J}}, 2I_2)$ and $I_{\mathrm{FDM}} \geq I_{\mathrm{FDM,p}}$, clearly (3.6) follows with equality if and only if x_1 and x_2 are Gaussian with $\gamma^2 = 0$ dB. □

The theorem, beyond the mathematical proof, has a practical explanation. The use of a second satellite, besides increasing the overall transmitted power, makes the distribution of $x_1(t) + \gamma x_2(t)$ closer to a Gaussian distribution (see the Berry-Esséen theorem [75]). Thus, a sort of shaping gain must be added to the gain arising from the higher power.

The strategy based on FDM is perfectly equivalent, in terms of ASE, to a strategy based on time division multiplexing (TDM), in which time is divided into slots of equal length, and each satellite is allotted a slot during which only that satellite

transmits and the other remains silent. During its slot, each satellite is allowed to use twice the power. However, on satellites, due to peak power constraints, it is not possible to double the power and the satellite amplifiers are not conceived for power bursts. Hence the TDM strategy will not be considered as a feasible solution in this scenario.

3.4 Achievable Rates by the Alamouti Scheme

We now consider the application of the Alamouti scheme [60]. The two satellites first transmit $x_1(t)$ and $x_2(t)$ and then $-x_2^*(t)$ and $x_1^*(t)$, respectively. The rate I_{A}, achievable by the Alamouti scheme, satisfies the following theorem.

Theorem 2. *Let us consider the ideal multiple access channel*

$$y(t) = x_1(t) + \gamma x_2(t) + w(t)\,,$$

where $x_i(t)$, $i = 1,2$ are random processes such that $-x_i(t)$ has the same finite-dimensional distributions as $x_i(t)$. The following inequality holds

$$I_{\mathrm{J}} \underset{(a)}{\geq} I_{\mathrm{A}} \underset{(b)}{\geq} I_{\mathrm{FDM}}$$

with equality in (a) if and only if $x_1(t)$ and $x_2(t)$ are independent Gaussian random processes with the same variance, and in (b) if and only if $\gamma^2 = 0$ dB.

Proof. Let us start by first proving inequality (a). The observable for Alamouti precoding is

$$\begin{aligned} y_{\mathrm{A},1} &= x_1 + \gamma x_2 + w_{\mathrm{A},1} \\ y_{\mathrm{A},2}^* &= -x_2 + \gamma x_1 + w_{\mathrm{A},2} \end{aligned}$$

where $w_{\mathrm{A},1}, w_{\mathrm{A},2}$ are independent Gaussian random variables with power N.

Let us evaluate

$$\begin{aligned} I_{\mathrm{J}} - I_{\mathrm{A}} &= h(y) - \frac{h(y_{\mathrm{A},1}, y^*_{\mathrm{A},2})}{2} && (3.13)\\ &\geq h(y) - \frac{h(y_{\mathrm{A},1}) + h(y^*_{\mathrm{A},2})}{2} && (3.14)\\ &= 0 && (3.15) \end{aligned}$$

where (3.15) is obtained by observing that $h(y) = h(y_{\mathrm{A},1}) = h(y^*_{\mathrm{A},2})$. Equality in (3.14) is achieved if and only if $y_{\mathrm{A},1}$ and $y^*_{\mathrm{A},2}$ are independent. From an application of the Lukacs-King theorem [76], independence holds if and only if x_1 and x_2 are independent Gaussian random variables with the same power.

We now prove inequality (b): the Alamouti observable, after receiver processing, is

$$\tilde{y}_{\mathrm{A},i} = \sqrt{1+\gamma^2}\, x_i + \tilde{w}_{\mathrm{A},i} \quad i = 1,2\,. \tag{3.16}$$

and is still a sufficient statistic for detection. The SNR in (3.16) is $(1+\gamma^2)/2 \leq 1$ times the one in (3.10) and $(1+\gamma^2)/2\gamma^2 \geq 1$ times that in (3.11). Hence, since the mutual information is a concave function of the SNR [74], no matter the input distribution, inequality (b) is straightforward and it holds with equality if and only if $\gamma^2 = 0$ dB. □

Theorem 2 shows that the AIR of the Alamouti scheme is between the ones achievable by two overlapping signals and by FDM. However, it has the interesting feature that it is not degraded by the equal rates constraint. This is due to the fact that both signals are transmitted once by the satellite with no attenuation and once by the satellite with attenuation γ. Hence, while it is always true that $I_{\mathrm{A}} \geq I_{\mathrm{FDM,p}}$, it can also happen that $I_{\mathrm{A}} \geq I_{\mathrm{J,p}}$.

3.5 AWGN Channel with Average Power Constraint

A first case study, useful to draw some preliminary considerations about the theoretical limits for the system under consideration, is the classical AWGN channel with

average power constraint (APC). For this case, we have that the two satellites of Figure 3.1 have no effect on the signal, hence the received signal reads

$$y(t) = x_1(t) + \gamma e^{j\phi(t)} x_2(t) + w(t)\,.$$

We express the APC as

$$\mathrm{E}\left[|x_i(t)|^2\right] \leq P \quad i = 1,2\,,$$

where P is the maximum allowed average power.

For this channel, the capacity is reached with independent Gaussian inputs, $p(t) = \mathrm{sinc}(t/T)$, and $TW = 1$ [72]. A sufficient statistic is derived by sampling the output of a low pass filter [54, 72]. Since we are assuming slow-varying phase noise, perfectly known at the receiver, the observable can be approximated as

$$y_k = x_k^{(1)} + \gamma e^{j\phi_k} x_k^{(2)} + w_k\,,$$

where $\phi_k = \phi(kT)$. The phase noise does not change the statistics, and hence the ASE I_{J} is given by the classical Shannon capacity, taking into account the total transmitted power, and reads

$$I_{\mathrm{J}} = \log_2\left(1 + (1+\gamma^2)\frac{P}{N}\right)\,,$$

where $N = N_0 W$ is the noise power in the considered bandwidth. If, instead, we adopt the FDM model (3.3), the ASE can be computed as the average of the ASEs of two subchannels, each transmitting on half the bandwidth:

$$I_{\mathrm{FDM}} = \frac{1}{2}\log_2\left(1 + 2\frac{P}{N}\right) + \frac{1}{2}\log_2\left(1 + 2\gamma^2\frac{P}{N}\right)\,.$$

When we introduce the equal rate constraint, it is straightforward to show that we have the following practical ASEs

$$\begin{aligned} I_{\mathrm{J,p}} &= \min\left(I_{\mathrm{J}}, 2\log_2\left(1 + \gamma^2\frac{P}{N}\right)\right) \\ I_{\mathrm{FDM,p}} &= \log_2\left(1 + 2\gamma^2\frac{P}{N}\right)\,. \end{aligned}$$

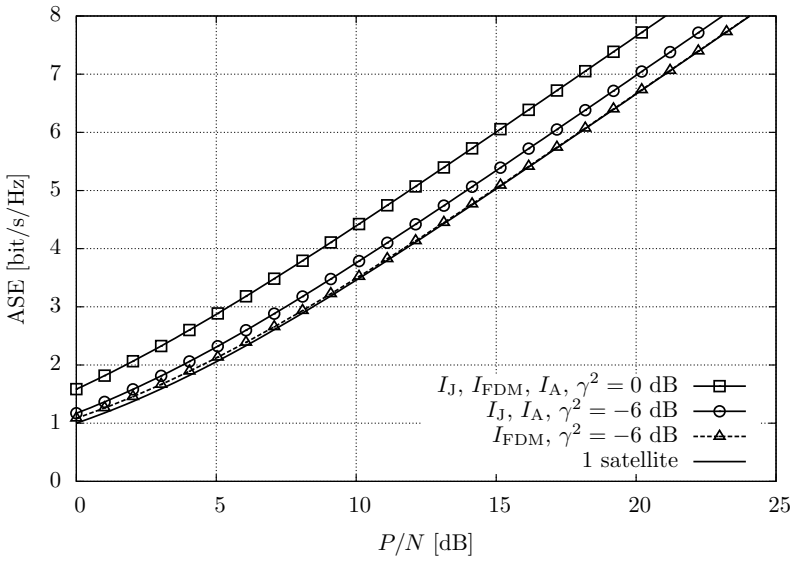

Figure 3.4: Joint ASE for different values of γ (AWGN channel with APC).

In Figure 3.4, we show the ASE I_{J} as a function of P/N, for different values of the power unbalance γ, together with the ASE that can be achieved when a single satellite is available ($\gamma \to 0$). In this case, the performance of the Alamouti scheme is exactly the same as I_{J}, as foreseen by Theorem 2. The figure also shows I_{FDM} for the same values of γ. We see that FDM is capacity-achieving when $\gamma = 1$ (i.e., $I_{\mathrm{J}} = I_{\mathrm{FDM}}$ when $\gamma = 1$, as also clear from the equations and as foreseen by Theorem 1) but it is suboptimal in the case of power unbalance.

In Figure 3.5, we report the practical ASEs for the cases of Figure 3.4. For signals with overlapping frequencies, with power unbalance $\gamma^2 \neq 0$ dB, $I_{\mathrm{J,p}}$ is lower than I_{J} only in the range of low P/N values, corresponding to the case $2I_2 < I_{\mathrm{J}}$. The transition is indicated by the change of slope in the curve. We also see that, for high power unbalance, a portion of $I_{\mathrm{J,p}}$ lies below single-satellite ASE.

In case of FDM, we clearly see how the user with the lower ASE limits $I_{\mathrm{FDM,p}}$. The curves coincide for $\gamma = 1$, while they suffer from a significant performance loss with respect to I_{FDM} for high values of power unbalance. If the power unbalance is

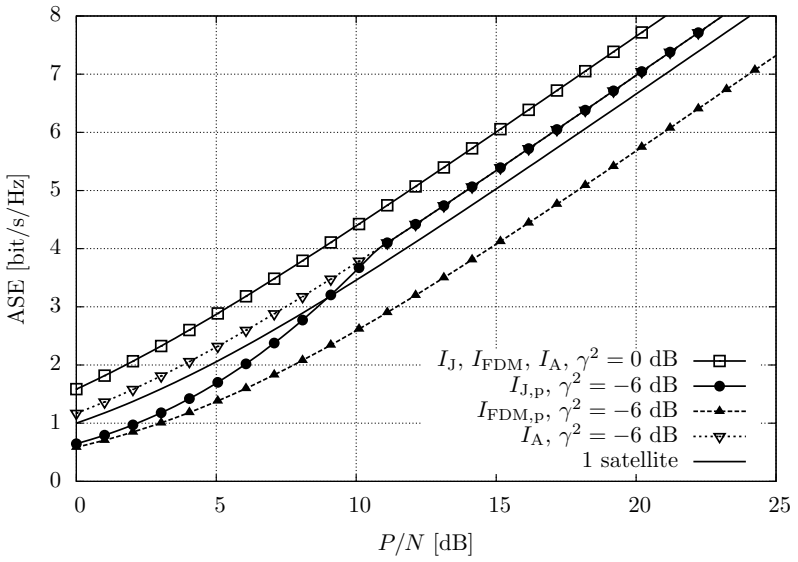

Figure 3.5: Practical ASE for different values of γ (AWGN channel with APC).

very high, FDM performs even worse than a single satellite. Finally we can notice that, when $\gamma^2 \neq 0$ dB, $I_{\mathrm{A}} > I_{\mathrm{J,p}}$ for low P/N values.

At the end of this section, we would like to motivate our choice of transmitting independent signals from the two satellites. Let us consider the opposite scenario where the same signal is transmitted from the two satellites. In this case, the received signal $y(t)$ can be expressed as

$$y(t) = x(t) + \gamma e^{j\phi(t)} x(t-\tau) + w(t)$$

where $x(t)$ is the transmitted signal, and τ the difference between the propagation delays of the two satellites. The received sample at time kT is

$$y_k = x_k + \gamma e^{j\phi_k} \sum_i \mathrm{sinc}(i - \tau/T) x_{k-i} + w_k \,.$$

The channel is equivalent to a time-varying frequency-selective channel

$$y_k = \sum_i h_{k,i} x_{k-i} + w_k \tag{3.17}$$

with impulse response $h_{k,i} = \delta_i + \gamma e^{j\phi_k} \mathrm{sinc}(i - \tau/T)$, where δ_i is the Kronecker delta function. As already said, ϕ_k is assumed slowly varying with respect to the symbol interval but, due to the oscillators' instabilities, it will be assumed with a coherence time shorter than the codeword length. Hence, we are interested in the ergodic rate obtained by averaging the information rate that can be obtained with a given value of ϕ. Independently of the value of τ, the average signal power is

$$\mathrm{E}\left[\left|\sum_i h_{k,i} x_{k-i}\right|^2\right] = (1+\gamma^2)P \tag{3.18}$$

and it can be shown that the ergodic rate cannot be higher than $\log_2\left(1+(1+\gamma^2)\frac{P}{N}\right)$, the rate achievable with independent signals (see [71] for a detailed proof).

3.6 AWGN Channel with Peak Power Constraint

As a first step to the theoretical characterization of our satellite transmission problem, we consider the case a peak-power-limited signal rather than an average-power-limited one. The adoption of a peak power constraint (PPC) comes naturally from the use of a saturated nonlinear HPA on the satellite. However, there is no expression for the channel capacity in this scenario, but only bounds are available [64]. For this reason, we concentrate on the study of a simplified discrete-time channel, where the PPC is imposed on information symbols [65].

In this section, we repeat the analysis of Section 3.5 in a peak-power-limited scenario. We first review the results in [65] for the case of a single transmitter, then we extend the reasoning to the case of two transmitters.

3.6.1 Analysis for a Single Transmitter

If we assume that $\gamma \to 0$, the model (3.2) simplifies to the following discrete-time memoryless channel model

$$y_k = x_k + w_k\,, \tag{3.19}$$

where y_k is the observable, $x_k = x_k^{(1)}$ is the k-th symbol transmitted by satellite 1, and w_k is AWGN with variance $N = N_0 W$. The input symbols x_k must be subject to a PPC, that can be expressed in the form

$$|x_k|^2 \leq P\,. \tag{3.20}$$

Channel (3.19) under constraint (3.20) was completely studied in [65]: the capacity-achieving distribution is discrete in amplitude and uniform in phase, and has the following expression

$$p(r,\theta) = p(\theta)p(r) = \frac{1}{2\pi}\sum_{\ell=1}^{m} q_\ell \delta(r-p_\ell)\,, \tag{3.21}$$

with $x_k = re^{j\theta}$. The distribution is formed of m concentric circles, each having weight q_ℓ and radius p_ℓ. The constraints of the problem, in polar coordinates, become

$$0 \leq p_\ell \leq \sqrt{P} \tag{3.22}$$

$$p_{\ell+1} > p_\ell \tag{3.23}$$

$$0 \leq q_\ell \leq 1 \tag{3.24}$$

$$\sum_{\ell=1}^{m} q_\ell = 1\,. \tag{3.25}$$

For the distribution (3.21), we can compute the rate $I(x_k;y_k)$ in closed form. First of all, we need to derive an expression for the PDFs of the channel and the observable. Based on the channel model (3.19), we have

$$p(y_k|x_k) = p(y_k|r,\theta) = \frac{1}{\pi N} e^{-\frac{|y_k - re^{j\theta}|^2}{N}}\,. \tag{3.26}$$

From (3.26) we can obtain the PDF $p(y_k)$ as

$$\begin{aligned}
p(y_k) &= \int_{r=0}^{+\infty}\int_{\theta=0}^{2\pi} p(y_k|r,\theta)p(r,\theta)\mathrm{d}r\mathrm{d}\theta \\
&= \frac{1}{\pi N}\frac{1}{2\pi}\int_{r=0}^{+\infty}\int_{\theta=0}^{2\pi} e^{-\frac{|y_k|^2+|r|^2}{N}} e^{\frac{2\Re\left[y_k re^{-j\theta}\right]}{N}} \sum_{\ell=1}^{m} q_\ell \delta(r-p_\ell)\mathrm{d}r\mathrm{d}\theta \\
&= \frac{1}{\pi N}\frac{1}{2\pi}\sum_{\ell=1}^{m} q_\ell e^{-\frac{|y_k|^2+|p_\ell|^2}{N}} \int_{\theta=0}^{2\pi} e^{\frac{2|y_k|p_\ell}{N}\cos(\arg(y_k)-\theta)}\mathrm{d}\theta \\
&= \frac{1}{\pi N}\sum_{\ell=1}^{m} q_\ell e^{-\frac{|y_k|^2+|p_\ell|^2}{N}} \mathrm{I}_0\left(\frac{2|y_k|p_\ell}{N}\right)\,,
\end{aligned} \tag{3.27}$$

where $\mathrm{I}_0(\cdot)$ is the modified Bessel function of the first kind and order zero. By combining (3.26) and (3.27) we have

$$\begin{aligned} I(x_k;y_k) &= \mathrm{E}\left[\log_2 \frac{p(y_k|x_k)}{p(y_k)}\right] \\ &= \mathrm{E}\left[\log_2 \frac{e^{-\frac{|y_k - re^{j\theta}|^2}{N}}}{\sum_{\ell=1}^{m} q_\ell e^{-\frac{|y_k|^2+p_\ell^2}{N}} \mathrm{I}_0\left(\frac{2|y_k|p_\ell}{N}\right)}\right]. \end{aligned} \tag{3.28}$$

The expectation in (3.28) is taken with respect to the actual random variables, i.e., x_k (and hence r and θ) and y_k. The latter is a function of x_k and w_k, and thus it depends on their statistics. The optimal values of m, q_ℓ and p_ℓ cannot be found in closed form, but they are subject to optimization [65]. For this reason, we evaluate (3.28) for increasing values of m and, for each value, we optimize the m radii to achieve the highest AIR. Optimization results for $1 \leq m \leq 20$ are plotted in Figure 3.6. We see that, as expected, as P/N increases, the optimal distribution is formed of a higher number of circles. We also point out that each curve in Figure 3.6 is the envelope of all curves with a lower number of circles, so m must be read as the maximum number of circles, i.e., one or more circles can have zero probability. The optimal number of circles is shown in Figure 3.7 as a function of P/N. We point out that the results in Figure 3.6 differ from those in [65] because of a different SNR definition. In fact, in [65], capacity curves are computed as a function of the SNR per dimension, while our curves are a function of the total SNR.

3.6.2 Extension to for Two Transmitters

Aim of this section is to extend the results of Section 3.6.1 to the case of two transmitters. For this scenario, we make the assumption that the optimal distributions of the two inputs are still in the form (3.21). This result has been demonstrated for real inputs [77], but not for complex inputs, as the case of interest here. For this reason, the computed AIR is a lower bound to the actual channel capacity, whose expression is not known. Under this assumption, the input amplitude distributions are

$$p(r_i) = \sum_{\ell=1}^{m_i} q_\ell^{(i)} \delta(r_i - p_\ell^{(i)}), \quad i = 1,2,$$

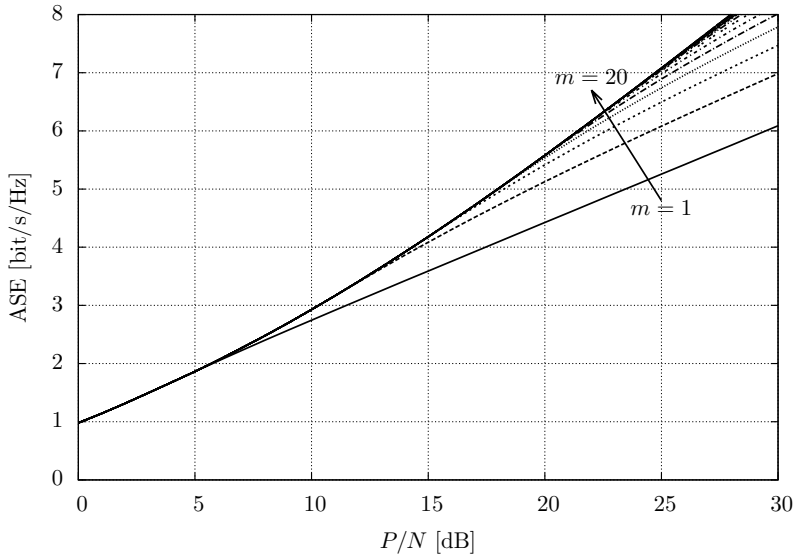

Figure 3.6: ASE for single transmitter for distributions composed of an increasing number of circles m (AWGN channel with PPC).

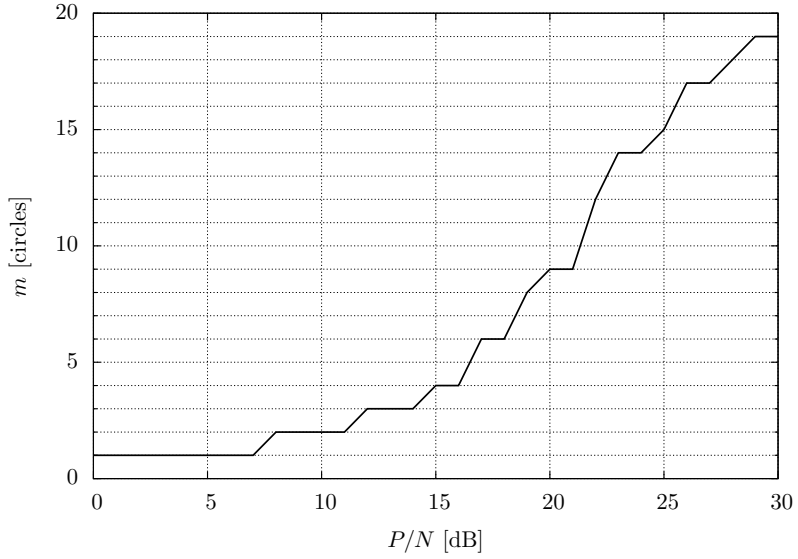

Figure 3.7: Optimal number of circles of the capacity-achieving distribution for a single transmitter.

and the received signal is an extension of (3.19):[4]

$$\begin{aligned} y_k &= x_k^{(1)} + \gamma x_k^{(2)} + w_k \\ &= r_1 e^{j\theta_1} + \gamma r_2 e^{j\theta_2} + w_k \,, \end{aligned}$$

with each of the two inputs satisfying constraints (3.22)–(3.25). In this scenario, we can express the joint AIR $I_{\mathrm{J}} = I(x_1, x_2; y)$ as an extension of (3.28):

$$I_{\mathrm{J}} = \mathrm{E}\left[\log_2 \frac{(2\pi)^2 e^{-\frac{|y_k - r_1 e^{j\theta_1} - \gamma r_2 e^{j\theta_2}|^2}{N}}}{\sum_{\ell=1}^{m_1} \sum_{i=1}^{m_2} q_\ell^{(1)} q_i^{(2)} \Lambda_{\ell,i}} \right] , \tag{3.29}$$

where

$$\Lambda_{\ell,i} = \int_0^{2\pi} \int_0^{2\pi} e^{-\frac{|y_k - p_\ell^{(1)} e^{j\theta_1} - \gamma p_i^{(2)} e^{j\theta_2}|^2}{N}} \mathrm{d}\theta_1 \mathrm{d}\theta_2 \,.$$

We have computed (3.29) for different levels of power unbalance between the two received signals; we have verified that the best performance is achieved when using input distributions with only one circle (i.e., $m_1 = m_2 = 1$ in (3.29)). The joint AIR is shown in Figure 3.8, where the curve labeled *1 satellite* is obtained as the envelope of the curves of Figure 3.6. We report here, for comparison, the AIR computed when FDM is used, assigning half of the bandwidth to each of the satellites. We see that, unlike the case of average power constraint, FDM is not the optimal choice, not even in the absence of power unbalance (when FDM gains exactly 3 dB from the single satellite). This result comes from a straightforward application of Theorem 1. In effect, since the two input distributions are not Gaussian, the inequality (3.5) is strict. Figure 3.8 also reports the AIR I_{A}, achievable by the Alamouti scheme. As foreseen by Theorem 2, we see that for $\gamma^2 = 0$ dB the rate I_{A} is perfectly equivalent to I_{FDM}, while, for $\gamma^2 = -6$ dB, FDM performs worse. For all values of γ we have that $I_{\mathrm{J}} > I_{\mathrm{A}}$, since the input signals are not Gaussian processes.

We also point out that, unlike what happens when the constraint is on the average power, in this case the theoretical upper bound for I_{J}, when $\gamma = 1$, is 6 dB higher than

[4] We point out that a phase noise term should be considered in the second signal. However, since this shift is assumed to be perfectly known at the receiver and the input distributions are invariant with respect to a phase rotation, we do not add it to our model.

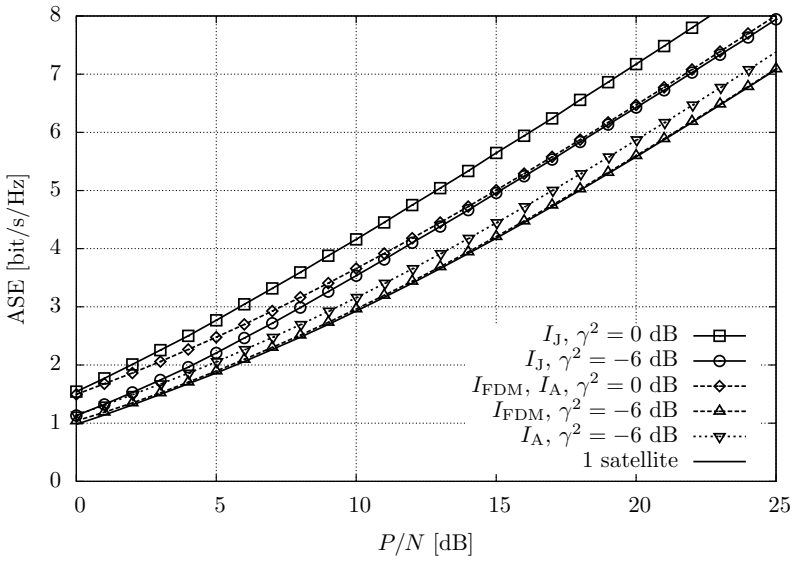

Figure 3.8: Joint ASE for different values of γ (AWGN channel with PPC).

the single transmitter case. This is because, if the two signals are perfectly in phase, the overall signal has double amplitude, and hence its power is $4P$ (i.e., 6 dB higher). This situation is unrealistic (and, in fact, we do not experience a 6 dB gain), but it is the upper limit for the AIR.

As already mentioned, in a broadcast scenario we have the further constraint that the two transmitters must use the same rate. When we impose this constraint to the rates shown in Figure 3.8, we obtain the practical rates in Figure 3.9. We see again that, as expected, the rates $I_{\mathrm{J,p}}$ and $I_{\mathrm{FDM,p}}$ have suffered a degradation for $\gamma^2 = -6$ dB, and we also notice that, for low values of P/N and a high power unbalance, the use of a single satellite may be convenient over the use of two overlapped signals. However, since the Alamouti scheme is not degraded by the application of the equal rates constraint, we can conclude that the I_{A} represents the best performance in a certain range of P/N.

We can better understand the impact of the equal rates constraint on the joint AIR by studying the ASE regions of the channel for different values of P/N, reported in

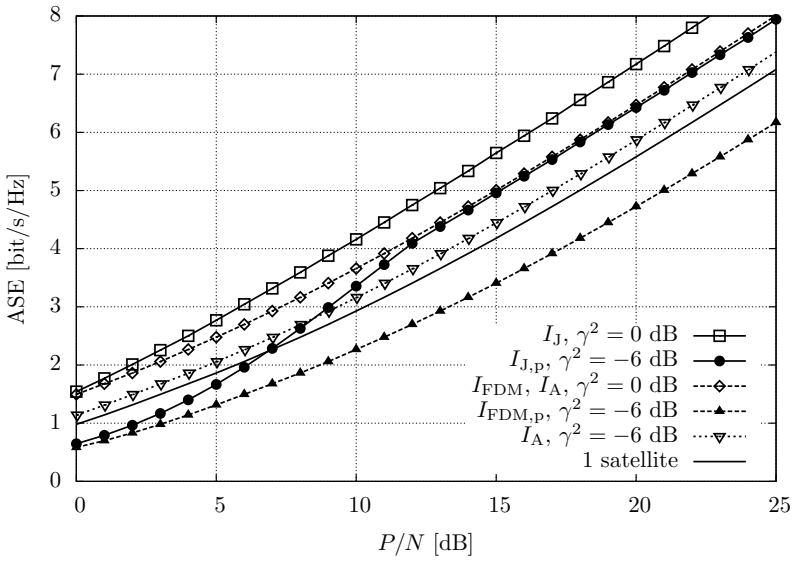

Figure 3.9: Practical ASE for different values of γ (AWGN channel with PPC).

Figure 3.10. From the analysis of these figures, we can conclude that the maximum sum-rate cannot always be achieved and we can have a numerical insight of the values of P/N and γ^2 that allow to improve the rates with respect to a case with only one transmitter. In particular, it is easy to understand that when the power unbalance is low ($\gamma^2 \to 0$ dB) the ASE region is perfectly symmetric and maximum sum-rate is achieved for all values of P/N. On the other hand, with high power unbalance ($\gamma^2 = -6$ dB) it is clear that maximum sum-rate can be achieved only at high P/N, whereas when the power is low the performance of two satellites is worse than that of a single satellite.

3.6.3 Practical Constellations for AWGN Channel with PPC

We are now interested in evaluating the performance of practical constellations with a finite number of points on the AWGN channel with PPC, in order to find which kind of discrete constellations can be successfully adopted on the satellite channel.

Starting from the single transmitter case, we see in Figure 3.11 that M-ary PSK

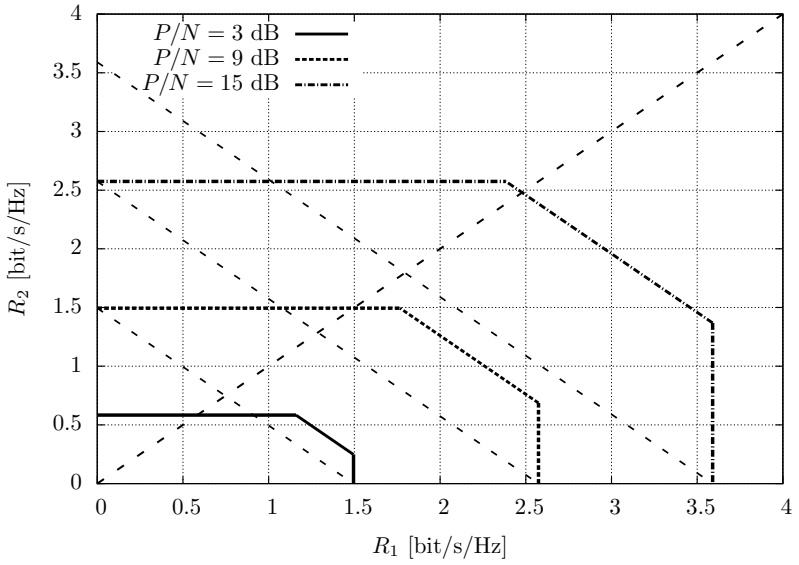

Figure 3.10: ASE regions for $\gamma^2 = -6$ dB (AWGN channel with PPC).

and APSK constellations, usually adopted in satellite communications, are practically capacity-achieving. However, as foreseen also by the theoretical analysis, constellations with multiple circles (such as APSK) are suboptimal when two transmitters are adopted. This can be seen in Figure 3.12, showing the envelopes of the ASEs achievable with constellations from QPSK to 64APSK, where APSKs exhibit a loss with respect to the bound I_{J} for high P/N values. As suggested by the theoretical results, we see that the bound is achieved by replacing APSKs with PSKs with the same number of points, whose envelopes are again shown in the figure. Figure 3.13 reports the same analysis for the practical rates, and the same conclusions hold. We point out that FDM and Alamouti schemes perform single-user operations, so they practically achieve their corresponding theoretical bounds with classical PSK/APSK constellations. Finally, we mention that we have attempted an optimization of the constellations, using the same GD algorithm described in Section 2.5.2, imposing that the constellations adopted by the two transmitters are identical. Optimization results suggest that PSKs are practically optimal in this scenario.

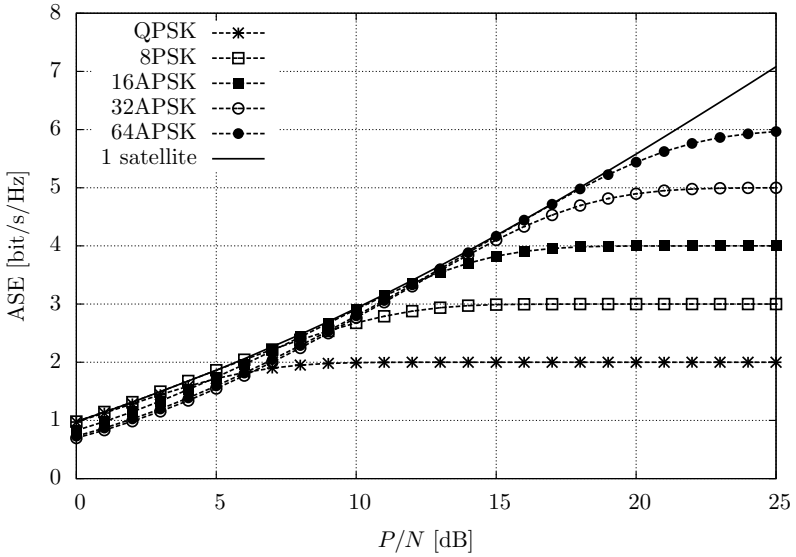

Figure 3.11: Single transmitter capacity and ASE for PSK/APSK constellations.

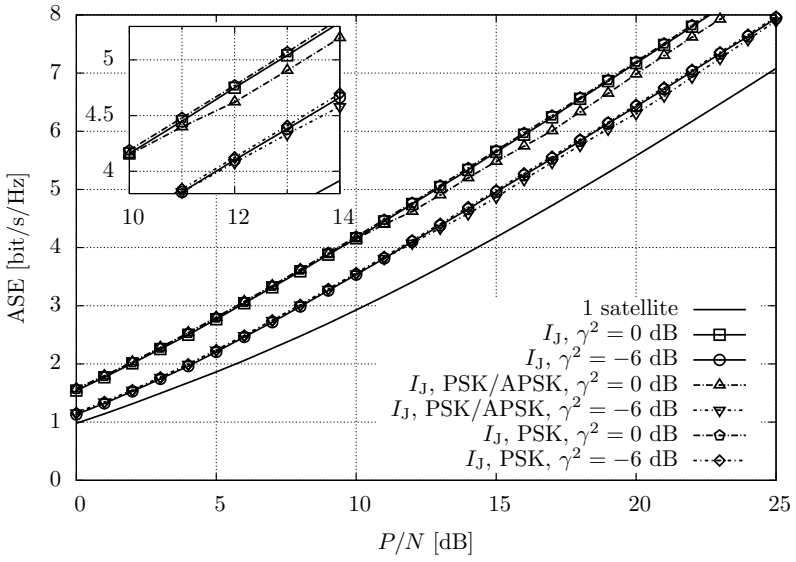

Figure 3.12: Joint ASE for PSK/APSK constellations and different values of γ.

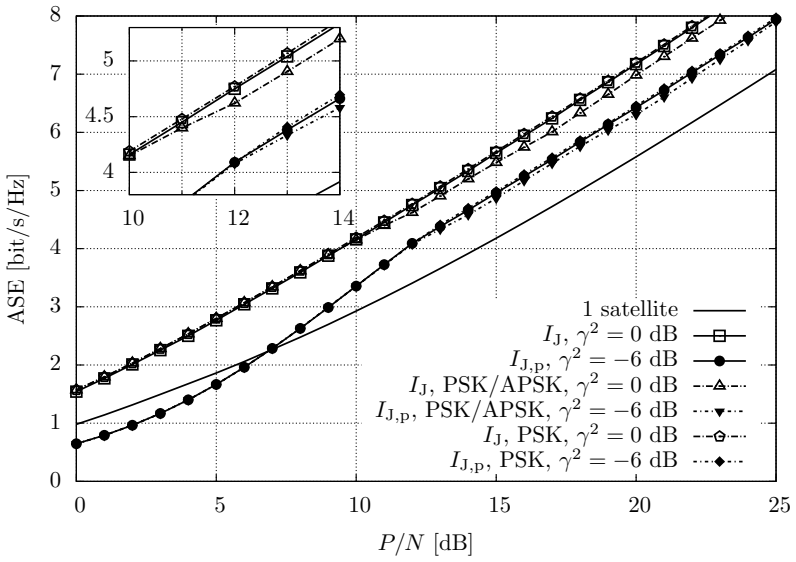

Figure 3.13: Practical ASE for PSK/APSK constellations and different values of γ.

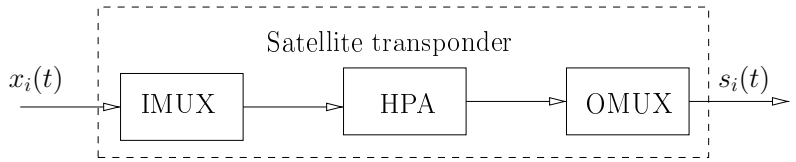

Figure 3.14: Block diagram of the considered satellite transponder.

3.7 Satellite Channel Model

This section investigates the performance of the system in Figure 3.1 when a realistic satellite transponder model is used. The block diagram of the adopted transponder model is the same as that we have adopted in Chapter 2, and it is depicted in Figure 3.14. The HPA, IMUX, and OMUX characteristics are described in Section 2.1, and the OMUX filter still has -3 dB bandwidth equal to 38 MHz, and they correspond to the DVB-S2 channel model [35].

The transmitted signals at the input of the two satellites are linearly modulated as in (3.1), with the same pulse and symbol interval, and the information symbols

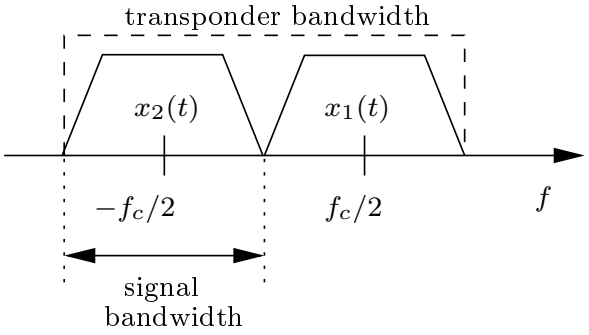

Figure 3.15: Transponder bandwidth allocation for FDM.

$x_k^{(i)}$ are drawn from the same discrete constellation. The symbol intervals of the two signals are also assumed to be perfectly aligned. Thus, the received signal reads as in (3.2). Process $\phi(t)$ models the difference of phase between oscillators and their phase noise, and is considered perfectly known at the receiver. We adopt the adaptive FS-MMSE equalizer described in Section 2.3, followed by a symbol-by-symbol multiuser detector (MUD) [78]. The MUD computes the a posteriori probabilities of the symbols as

$$p\left(y_k|x_k^{(1)},x_k^{(2)}\right) \propto \exp\left\{-\frac{\left|y_k-\beta\left(x_k^{(1)}+\gamma x_k^{(2)}e^{j\phi_k}\right)\right|^2}{N_0}\right\},$$

where y_k is the sample at the output of the FS-MMSE equalizer, β is a possible (complex-valued) bias, and $\phi_k = \phi(kT)$ is the phase noise process at the receiver (under the assumption that $\phi(t)$ is slow enough with respect to the symbol time).

Similarly to previous sections, we also consider an FDM scenario: the transponder bandwidth is equally divided into two subchannels as schematically depicted in Figure 3.15. Then, the FDM receiver performs detection separately with two FS-MMSE equalizers, followed by a symbol-by-symbol receiver.

As already done with the other channel models, we adopt the Alamouti scheme as a third possibility: the Alamouti precoding is performed on transmitted symbols and, at the receiver side, after a proper processing, two separate FS-MMSE equalizers

and symbol-by-symbol receivers are adopted. Unlike the previous scenarios, in the presence of nonlinear distortions and phase noise, the Alamouti scheme cannot perfectly separate the two signals at the receiver. However we will show in the numerical results that its performance is still excellent.

The complexity of the channel model does not allow to obtain results in a closed form as in previous sections. Hence, the achievable ASEs for this scenario are computed through the Monte Carlo method proposed in [6], already applied in Chapter 2 and briefly summarized also in Section 1.2. Once again, we recall that these values are a lower bound to the actual ASE and they are achievable with the specific adopted receiver. The ASE curves shown in the next section describe the possible achievable gains in a scenario that is more realistic than those described previously. All results will be reported as a function of P_{sat}/N, where P_{sat} is the HPA power at saturation.

3.7.1 Numerical results

For this section, we apply the transmission parameters that we have optimized in Chapter 2 for the single-satellite scenario. Namely, signals are transmitted with a symbol rate of 37 Mbaud, using an RRC shaping pulse $p(t)$ with roll-off factor $\alpha = 0.1$. We adopt the classical constellations of satellite communications, from QPSK to 32APSK (denoted as PSK/APSK schemes) and, as an alternative, we also consider the use of 16PSK and 32PSK, as suggested by the theoretical analysis. The IBO has been optimized to 0 dB for QPSK and 8PSK, and to 3 dB for all other modulations.[5]

Figure 3.16 shows the envelope of the practical ASE $I_{\text{J,p}}$ for the considered modulations, with power unbalance $\gamma^2 = 0$ dB. Details on the modulations of the envelope are reported in Table 3.1. The figure also shows the ASE for FDM, for the Alamouti scheme, and for a single satellite. In case of FDM, each signal has symbol rate $1/T = 18.5$ Mbaud, and the frequency spacing is equal to $f_c = (1+\alpha)/T = 20.35$ MHz, which has been found to be practically optimal for this scenario. We can see from the figure that two overlapped signals can achieve a higher ASE with respect to all considered alternatives. Moreover, the envelopes show that 32APSK and 32PSK are

[5] We point out that the impact of interchannel interference due to transponders transmitting on adjacent frequencies is negligible for all the presented scenarios, and hence it will not be considered [79].

Modulation	P_{sat}/N [dB]
QPSK	-10 – 0
8PSK	0 – 7.5
16APSK/16PSK	7.5 – 25

Table 3.1: P_{sat}/N range of the envelope $I_{\text{J,p}}$ for PSK and APSK constellations and $\gamma = 1$.

not convenient in case of overlapped signals, since they perform worse than 16APSK and 16PSK, and PSK constellations perform better than APSK modulations. It is interesting to notice that, although the channel model is affected by nonlinear effects, inequality (3.6) still holds true, even in this case. We also notice that, at high P_{sat}/N, FDM performs worse even than a single satellite. This loss is due to the ICI from the second FDM signal, which lies in the same OMUX bandwidth. In fact, due to the spectral regrowth after the HPA, the two FDM signals are no more orthogonal. This effect is proved in Figure 3.17, which compares the FDM curve with two ASE curves: ideal FDM in the absence of ICI, and a single satellite with twice the power P_{sat}. Similarly to the linear channel, ideal FDM can achieve the same ASE as the single satellite with double power, but in a realistic case ICI has an impact on the performance.

We can notice from Figure 3.16 that gains given by two overlapped signals with respect to a single satellite can be higher than 3 dB. The gains over 3 dB are related to the shaping of the overall signal, obtained by the sum of the satellite outputs. Indeed, as already mentioned in Section 3.3, the sum of two signals has an amplitude distribution that is closer to a Gaussian distribution. Figures 3.18 and 3.19 show the PDF and the cumulative distribution function (CDF) of the signal amplitude, properly normalized by the number of transmitting satellites. We compare the amplitude distributions of a single signal and two overlapped signals (with $\gamma^2 = 0$ dB), when the transmitters adopt 16PSK, RRC pulses with roll-off $\alpha = 0.1$, IBO equal to 3 dB. For comparison purpose we report also the PDF and CDF of the Gaussian distribution with unit variance. It is clear from the figures that the sum of two signals is closer

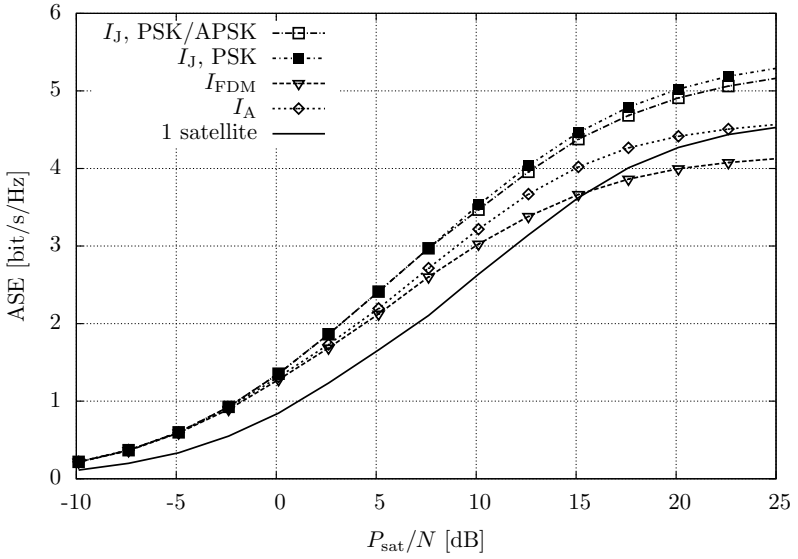

Figure 3.16: ASE achievable by PSK and APSK for two satellites and $\gamma^2 = 0$ dB.

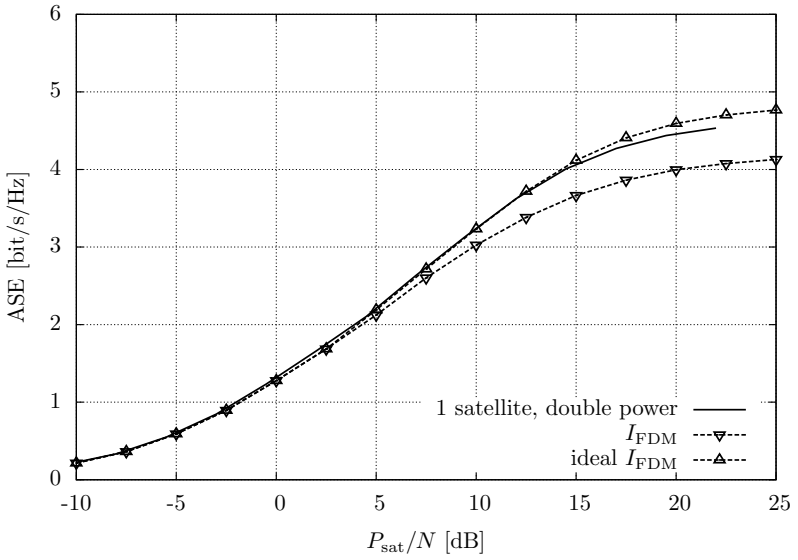

Figure 3.17: ASE achievable by PSK/APSK constellations for two satellites, using FDM and $\gamma^2 = 0$ dB.

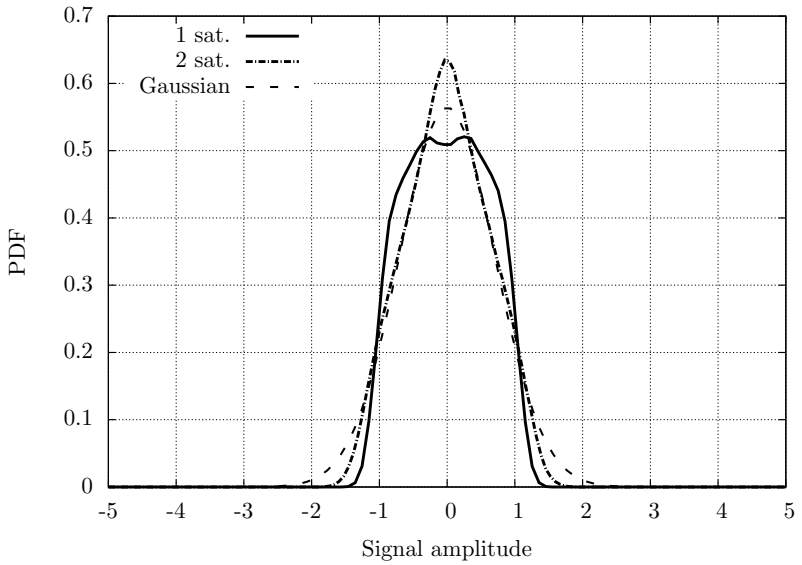

Figure 3.18: PDF of the signal amplitude with 16PSK and $\gamma^2 = 0$ dB.

to a Gaussian distribution than the single transmitter. We have verified that similar considerations hold for 8PSK.

Figure 3.20 and Table 3.2 report ASE curves for the same scenario as in Figure 3.16, but with power unbalance equal to 6 dB. Overlapped signals again outperform FDM for every P_{sat}/N value but, since the equal rate constraint limits the performance to that of the lower power signal, the Alamouti scheme and a single satellite have higher ASE at low P_{sat}/N. The behavior of $I_{\text{J,p}}$ with respect a single satellite can be seen from the ASE regions in Figure 3.21, we can notice that it is perfectly in line with results found for the peak limited AWGN channel, despite a big difference between the two models.

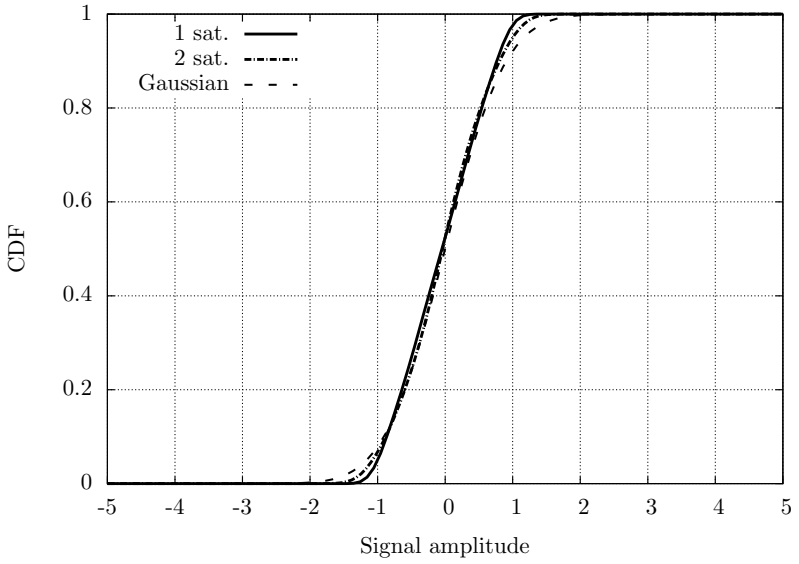

Figure 3.19: CDF of the signal amplitude with 16PSK and $\gamma^2 = 0$ dB.

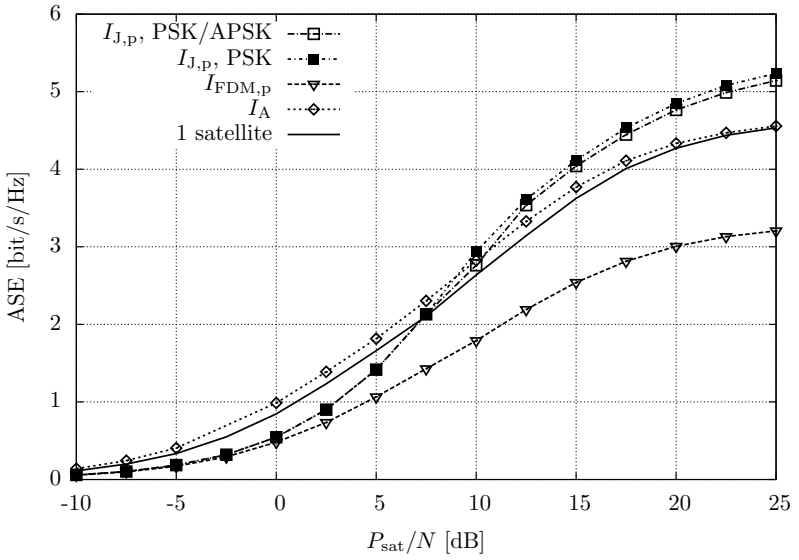

Figure 3.20: ASE achievable by PSK and APSK for two satellites and $\gamma^2 = -6$ dB.

Modulation	P_{sat}/N [dB]
QPSK	-10 – 5
8PSK	5 – 12.5
16APSK/16PSK	12.5 – 25

Table 3.2: P_{sat}/N range of the envelope $I_{\text{J,p}}$ for PSK and APSK modulations and $\gamma = 1/2$.

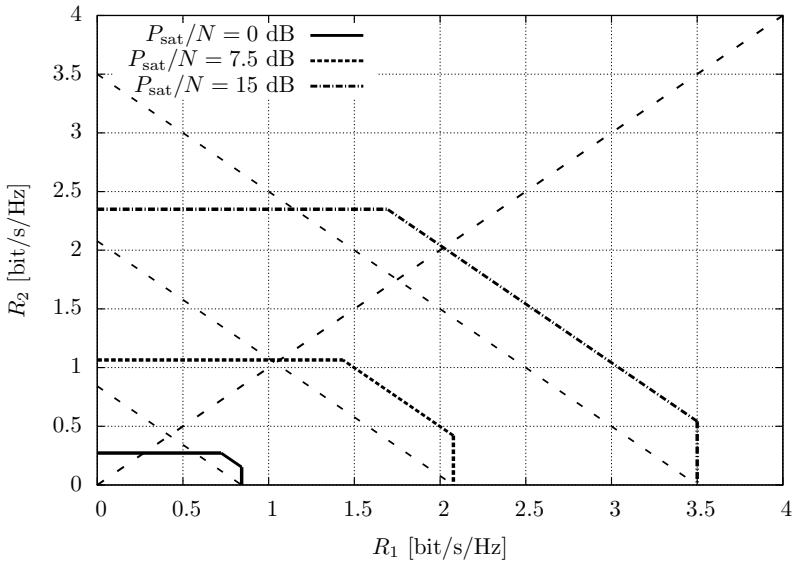

Figure 3.21: ASE regions for the two-satellites channel with $\gamma^2 = -6$ dB.

Mod.	rates	P_{sat}/N [dB]	SE [bit/s/Hz]
QPSK	1/4	-0.7	1.0
8PSK	1/4	3.0	1.5
8PSK	1/4+1/2	5.55	2.25
8PSK	1/4+3/5	7.4	2.55
8PSK	1/4+2/3	8.7	2.75

Table 3.3: MODCODs for overlapped signals with $\gamma^2 = 0$ dB.

3.8 Practical Codes for Multiple Satellites Systems

So far, this chapter has shown only information theoretical results, in terms of ASE, for different channel models. We have demonstrated that promising gains are possible on a realistic satellite channel. However, what still remains unknown is whether similar gains can be achieved by a practical system, adopting some specific MODCODs. A complete analysis of the performance of DVB-S2X MODCODs on this two-satellites channel has been performed in [80], which shows, through extrinsic information transfer (EXIT) charts [81] analysis and PER simulations, that the existing codes are not well designed to work in this scenario with multiple satellites. In particular, only a few low-cardinality MODCODs could be found to be working, and even those exhibit significant losses with respect to the ASE. The results of the analysis in [80] are reported in Figure 3.22 and Tables 3.3–3.4, where, to satisfy the equal rates constraint, the two transmitters are allowed to exchange the code rates at each new codeword (hence the notation $r_1 + r_2$ in some entries of Table 3.3). To improve the SE achieved by practical coding schemes, in this scenario, a new code design is required [58, 81].

In this section, we introduce an alternative approach to the design of a new code, that can be applied when the two signals originate from the same satellite. In this case, in fact, the two signals are generated by the same oscillator and reach the receiver at the same time because there is no difference between the two paths. Under these conditions, that ensure the absence of both delay and random phase shift between the

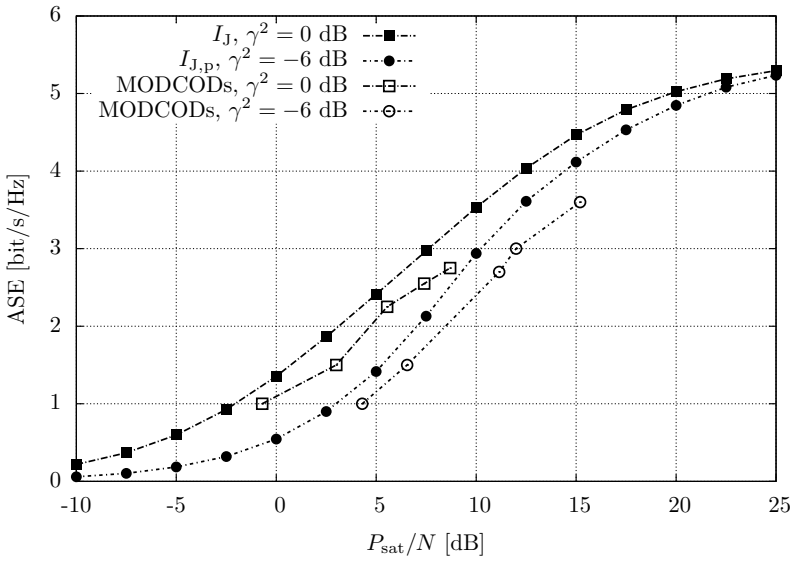

Figure 3.22: ASE and practical MODCODs for the two-satellites scenario.

Mod.	rates	P_{sat}/N [dB]	SE [bit/s/Hz]
QPSK	1/4	4.3	1.0
8PSK	1/4	6.55	1.5
8PSK	9/20	11.15	2.7
8PSK	90/180	12.0	3.0
16PSK	9/20	15.2	3.6

Table 3.4: MODCODs for overlapped signals with $\gamma^2 = -6$ dB.

two signals, we can think of optimizing the phase shift of the second signal to find the angle that maximizes the information rate. The received signal, then, becomes

$$y(t) = s_1(t) + e^{j\varphi} s_2(t) + w(t)\,,$$

where φ is a constant, properly chosen, phase shift, and the attenuation γ is equal to 1 because both signals originate in the same point. By performing an optimization on the values of φ, we verified that there is no clear optimal value. However,

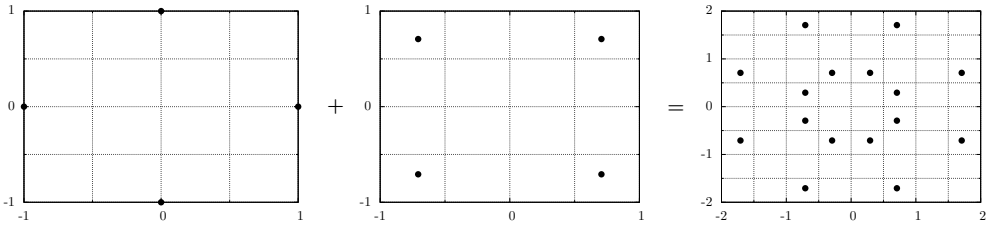

(a) Sum of two QPSK constellations.

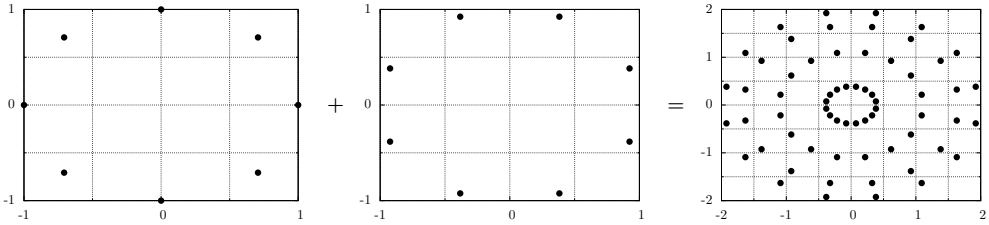

(b) Sum of two 8PSK constellations.

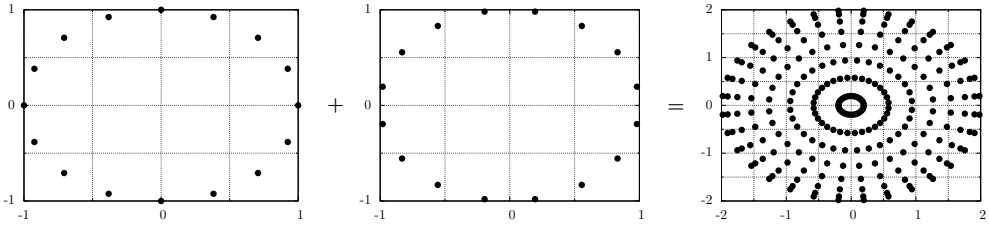

(c) Sum of two 16PSK constellations.

Figure 3.23: Joint constellations for PSK.

setting a value of $\varphi = \pi/M$, where M is the cardinality of the PSK constellation, grants the simplest design for the resulting constellation and an information rate that is practically the optimal one.

Given two M-PSK constellations, it is easy to see that, if we rotate one of them by π/M, the resulting joint constellation is formed of $M/2$ circles, each composed of $2M$ equally spaced points. Three examples are shown in Figure 3.23, for $M = 4, 8, 16$, respectively.

We then need to design a good mapping for the joint constellation. Since we have M^2 points, we need $\log_2(M^2)$ bits. We choose to use the first $\log_2(M/2)$ bits to

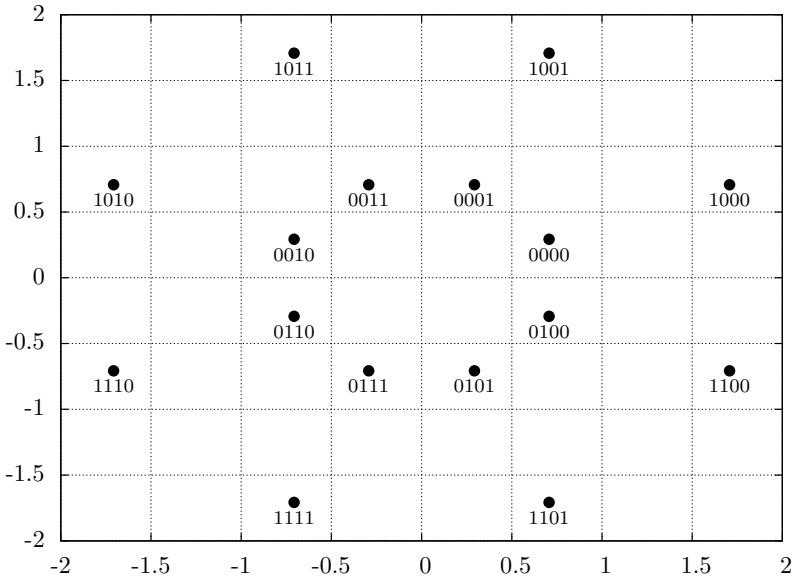

Figure 3.24: Joint mapping for two QPSK constellations.

identify the circle, and the remaining $\log_2(2M)$ bits to label the points on each circle. Mapping is Gray on each circle and also between adjacent circles. The selected joint mapping is shown in Figure 3.24 for two QPSK constellations, where the first bit identifies the circle, and the remaining three bits label the points. Unlike a classical mapping scheme, reported in Figure 3.25 for comparison, where each signal is mapped independently, the proposed approach requires a cooperative operation of the two transmitters. We have verified the performance of this new scheme both in terms of ASE and SE achieved by some practical MODCODs. The results shown in Figure 3.26 demonstrate that this joint scheme allows to improve the ASE at high SNR, but, most of all, it allows to achieve SE values close to the theoretical bounds in all the SNR range, without the need to redesign binary codes. The details of the selected MODCODs are reported in Table 3.5. Finally, we mention that the standard DVB-S2X codes can perform well when FDM or the Alamouti scheme are adopted because there are only single-user operations involved.

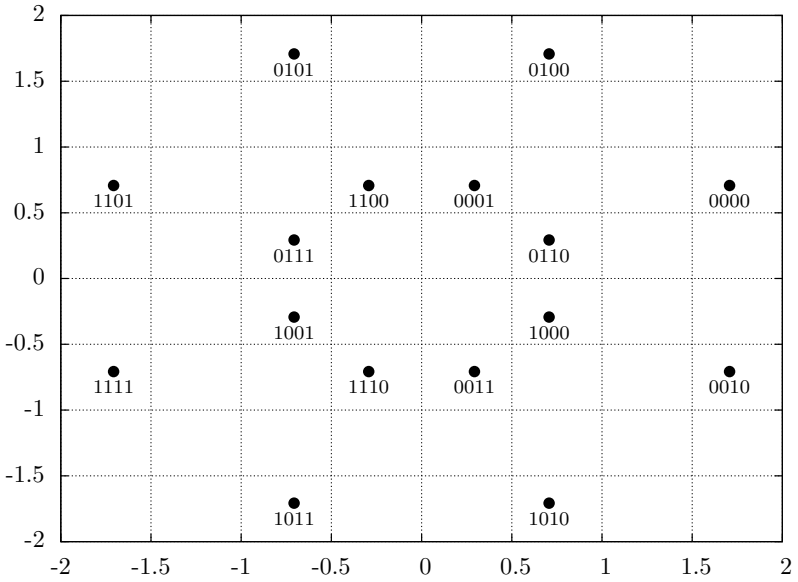

Figure 3.25: Classical mapping for two QPSK constellations.

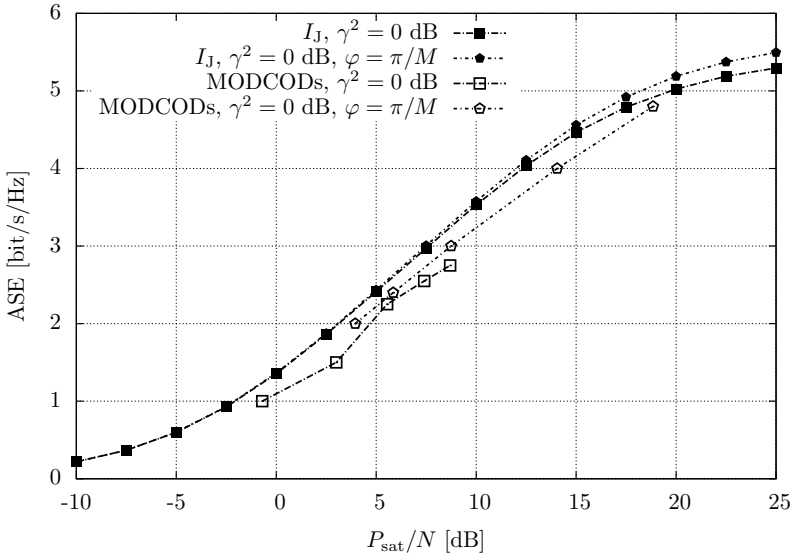

Figure 3.26: ASE and practical MODCODs with the proposed joint mapping.

Mod.	rates	P_{sat}/N	SE
QPSK	1/2	3.9	2.0
QPSK	3/5	5.85	2.4
8PSK	1/2	8.75	3.0
16PSK	1/2	14.05	4.0
16PSK	3/5	18.85	4.8

Table 3.5: MODCODs for overlapped signals and the proposed joint mapping.

3.9 Conclusions

We have investigated the rates achievable by a system using two co-located satellites. We have exploited the presence of the second satellite to improve the SE of the system. We have studied three alternative channel models: AWGN channel with APC, AWGN channel with PPC, and the DVB-S2 satellite channel. For all cases we have considered signals with overlapping frequencies, FDM, and the Alamouti scheme. Overlapped signals result to be convenient in all cases with respect to FDM, but we have shown that there are cases in which the Alamouti scheme can outperform both, and that even a single satellite can be convenient over overlapped signals: these cases depend on the power unbalance and on the received signal-to-noise power ratio. Finally, after showing that standard LDPC codes are not well designed for this two-satellites scenario, we have proposed a new cooperative mapping scheme that allows to overcome this problem without resorting to a new code design.

Chapter 4

Multiuser Detection in Multibeam Satellite Systems

The recent years have witnessed the explosion of satellite services and applications, and the related growing demand for high data rates. Next-generation satellite systems need new technologies to improve their spectral efficiency, in order to sustain the information revolution of modern societies. The grand challenge is to satisfy this demand by living with the scarcity of the frequency spectrum. Resource sharing is probably the only option, and can be implemented by adopting a multibeam system architecture, which allows to reuse the available bandwidth in many beams. The interference caused by resource sharing is typically considered undesirable, but a way to dramatically improve the spectral efficiency is to exploit this interference, by using interference management techniques at the receiver.

In this chapter, we consider the benefits of the adoption of multiuser detection at the terminal in the forward link of a multibeam satellite system. Our reference is a DVB-S2 system [35], where an aggressive frequency reuse is applied. Under these conditions, the conventional single-user detector (SUD) suffers from a severe performance degradation when the terminal is located near the edge of the coverage area, due to the high co-channel interference. On the other hand, the application of a decentralized MUD at the terminal, able to cope with the interference, can guarantee

the required performance [82, 83]. Of course, a computational complexity increase must be paid.

The literature on multiuser detection is wide, and in the area of satellite communications it essentially focuses on the adjacent channel interference mitigation for the return link [84–86], and it includes centralized techniques to be applied at the gateway. Less effort has been devoted to the forward link. Recently, the benefits that can be achieved, in terms of SE, when high frequency reuse is applied in a DVB-S2 system [35], and multiuser detection is adopted at the terminal to manage the presence of strong co-channel interference, have been investigated in [82]. The superiority of the MUD has been demonstrated through error rate simulations. In [83], the authors study the applicability of a low complexity MUD based on soft interference cancellation. The advantage of the proposed detector is shown in terms of frame error rate.

In this chapter, we generalize the analysis of [82] by supplying an information-theoretic framework which allows us to evaluate the performance in terms of AIR, without the need of lengthy error rate simulations, and hence strongly simplifying the comparison of various scenarios. Furthermore, we consider also different transmission strategies, where the two signals intended for the two beams cooperate to serve the two users (one in the first beam and the other in the second one). In one scenario, the two users in the adjacent beams are served consecutively in a TDM fashion, instead of being served simultaneously. In the other scenario, we consider the Alamouti space-time block code [60], consisting in the two satellites exchanging the transmitted signals in two consecutive transmissions.

Finally, we show that the theoretical limits predicted by the information-theoretic analysis can be approached by practical coded schemes. As expected, the Alamouti precoding based schemes work well with standard codes since single-user operations are performed. On the other hand, we observe that classical single-user codes are not suitable for multiuser applications. Therefore, we analyze the convergence behavior of joint multiuser detection/decoding by means of an EXIT chart analysis [87]. We start by considering the schemes based on the MODCODs of the DVB-S2 standard [35], and quantify the loss with respect to the theoretical limits. Once identified the reasons for this performance loss, we prove that a large gain can be obtained from

a redesign of the code and/or of the bit mapping.

In the following, Section 4.1 presents the system model and describes the three considered scenarios and related detection strategies. The information-theoretic analysis is treated in Section 4.2, and gives us the necessary means for the computation of the information rate for the reference beam. The EXIT chart analysis is described in Section 4.3. Section 4.4 presents the results of our study, whereas conclusions are drawn in Section 4.5.

4.1 System Model

We focus on the forward link of a satellite communication system. Figure 4.1 depicts a schematic view of the baseband model we are considering. Signals $s_i(t)$, $i = 1, \ldots, U$, are U signals transmitted by a multibeam satellite in the same frequency band. The satellite is thus composed of U transmitters (i.e. transponders) and serves U users on the ground. The nonlinear effects related to the high power amplifiers which compose the transponders are neglected since a multibeam satellite generally works in a multiple carriers per transponder modality, and hence the operational point of its amplifiers is far from saturation [35]. We consider the case where the users experience a high level of co-channel interference, since we assume that they are located close to the edge of the coverage area of a beam and that an aggressive frequency reuse is applied.

The signal received by a generic user can be expressed as

$$r(t) = \sum_{i=1}^{U} \gamma_i s_i(t) + w(t)\,, \tag{4.1}$$

where γ_i are proper complex gains, assumed known at the receivers, and $w(t)$ is the thermal noise. Without loss of generality, we assume that "User 1" is the reference user and that $|\gamma_i| \geq |\gamma_{i+1}|$. We will evaluate the performance of the reference user when the other users adopt fixed rates. We will consider the following three scenarios, which imply different transmission and detection strategies.

Scenario 1. Signal $s_i(t)$ is intended for user i, and we are interested in the evaluation

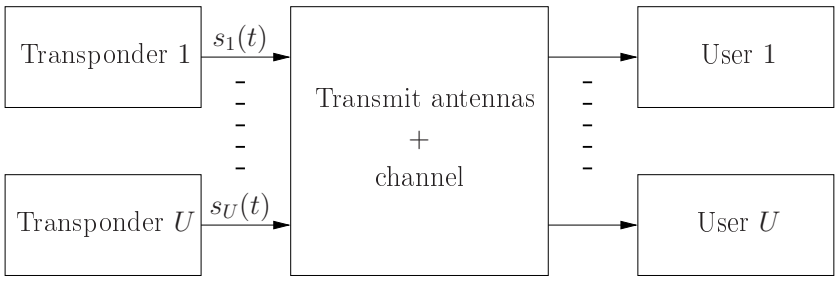

Figure 4.1: Schematic view of the considered architecture.

of the performance for "User 1", whose information is carried by the signal with $i = 1$. For this scenario, we evaluate the AIR, or equivalently the ASE, when "User 1" employs different detectors. In particular, we consider the case when "User 1" adopts:

- A SUD. In this case, all interfering signals $s_i(t)$, $i = 2, \ldots, U$ are considered as if they were additional thermal noise.
- A MUD for the useful signal and one interferer. In this case, the receiver is designed to detect the useful signal and the most powerful interfering signal (that with $i = 2$ in our model), whereas all the remaining signals are considered as if they were additional thermal noise. Data related to the interfering user are discarded after detection. This case will be called MUD$\times$2 in the following.

Our analysis can be easily extended to the case of a MUD designed for more than two users. On the other hand, given the actual users' power profile, it has been shown in [82] that the MUD$\times$2 offers the best trade-off between complexity and performance.

Scenario 2. A different transmission strategy is adopted in this case. Without loss of generality, we will consider detection of signals $s_1(t)$ and $s_2(t)$ and users 1 and 2 only. As in scenario 1, the remaining signals are considered as additional thermal noise. Instead of simultaneously transmitting signal $s_1(t)$ to "User 1" and signal $s_2(t)$ to "User 2", as in the previous scenario, we here serve "User 1" first by employing both signals $s_1(t)$ and $s_2(t)$ for a fraction α ($0 \leq \alpha \leq 1$) of the total time, and then "User 2" by employing both signals $s_1(t)$ and $s_2(t)$ for the remaining fraction $1 - \alpha$

of the total time. The fraction α can be chosen in order to maximize the sum-rate or simply by taking into account the different data rate needs of the users.

Signals $s_1(t)$ and $s_2(t)$ are independent (although carrying information for the same user). The receiver must jointly detect both signals and its complexity is comparable to that of the MUD$\times$2 described for the first scenario. In scenarios 1 and 2, $s_1(t)$ and $s_2(t)$ are properly phase-shifted in order to maximize the AIR.[1]

Scenario 3. As in the first scenario, $s_1(t)$ is for "User 1" and $s_2(t)$ for "User 2". We use two transponders to implement the Alamouti space-time block code: the two transponders for beams 1 and 2 first transmit $s_1(t)$ and $s_2(t)$ and then $-s_2^*(t)$ and $s_1^*(t)$, respectively. At the receiver side of "User 1", after a proper processing, the interference caused by signal 2 is removed and a SUD can be employed.

4.2 Information-theoretic Analysis

In this section, we describe how to compute the AIR related to "User 1" assuming the previously described transmission models. This analysis gives us the ultimate performance limits of the considered satellite system, which will be used as a benchmark for the performance of practical coded schemes.

We start by considering **scenario 1**, and describe how to compute the AIR of "User 1" assuming the MUD$\times$2 receiver. The same technique can be used to compute the AIR related to "User 2" and straightforwardly extends to the case of MUD for more than two users. The channel model assumed by the receiver is

$$y = x_1 + \gamma x_2 + w\,, \tag{4.2}$$

where x_i is the $M^{(i)}$-ary complex-valued symbol sent over the i-th beam and w collects the thermal noise, with power N, and the remaining interferers that the receiver is not able to cope with. Symbols x_1 and x_2 are mutually independent and distributed according to their probability mass function $P(x_i)$. They are also properly normalized such that $\mathrm{E}\left[|x_i|^2\right] = P$, where P is the transmitted power per user. The parameter γ is complex-valued and models the power unbalance and the phase shift between the

[1] We assume that the signals are modulated by using the same frequency.

two signals. The random variable w is assumed complex and Gaussian. We point out that this is an approximation exploited only by the receiver, while in the actual channel the interference is clearly generated as in (4.1). The MUD$\times$2 receiver has a computational complexity which is proportional to the product $M^{(1)}M^{(2)}$ [78].

We are interested here in the computation of the maximum achievable rate R_1 for "User 1" when "User 2" adopts a fixed rate R_2, and the MUD$\times$2 is employed. Rates are defined as $R_i = r^{(i)} \log_2\left(M^{(i)}\right)$, where $r^{(i)}$ is the rate of the adopted binary code. The rates of the other $U-2$ interferers do not condition our results because, at the receiver, they are treated just as noise. This problem is quite different with respect to the case of the MAC, discussed in [66] and analyzed in Chapter 3, where both rates (R_1, R_2) are jointly selected. In fact, here the rate R_2 is fixed and the data of "User 2" can be discarded after detection.

The AIR for "User 1", in the considered scenario, is given by Theorem 1, whose proof is based on the following two lemmas. An alternative proof can be found in [88]. The first one defines the maximum rate I_A achievable by "User 1" when "User 2" can be perfectly decoded.

Lemma 1. *For a fixed rate R_2, the rate*

$$I_A = \begin{cases} I(x_1;y|x_2) & \text{if} \quad R_2 \le I(x_2;y) \\ I(x_1,x_2;y) - R_2 & \text{if} \quad I(x_2;y) < R_2 \le I(x_2;y|x_1) \\ 0 & \text{if} \quad R_2 > I(x_2;y|x_1) \end{cases}$$

is achievable by "User 1" and is not a continuous function of P/N. Namely, a cut-off SNR_c *exists such that $I_A = 0$ for $P/N \le \mathrm{SNR}_c$ and $I_A > 0$ for $P/N > \mathrm{SNR}_c$ with a discontinuity.*

Proof. In [66], it is shown that the achievable region for the MAC is given by the region of points (R_1, R_2) such that

$$R_1 \le I(x_1;y|x_2) \triangleq I_1 \tag{4.3}$$

$$R_2 \le I(x_2;y|x_1) \triangleq I_2 \tag{4.4}$$

$$R_1 + R_2 \le I(x_1,x_2;y) \triangleq I_{\mathrm{J}}\,, \tag{4.5}$$

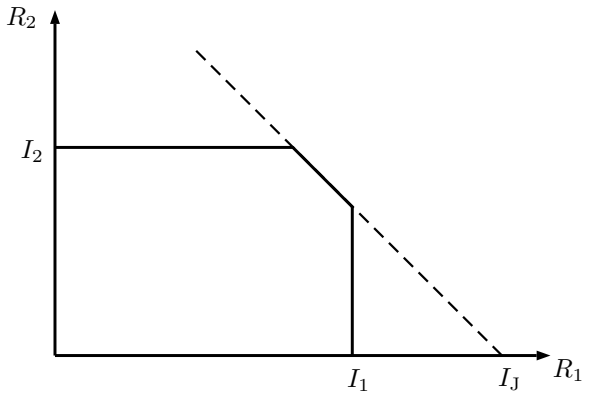

Figure 4.2: Example of MAC capacity region.

where we have adopted the same notation as in Chapter 3. An example of such a region is shown in Figure 4.2. If R_2 is constrained to a given value, we derive from (4.3) and (4.5) that

$$R_1 \leq \min\{I(x_1;y|x_2), I(x_1,x_2;y) - R_2\}$$

when $R_2 \leq I(x_2;y|x_1)$. The first term is lower when

$$R_2 \leq I(x_1,x_2;y) - I(x_1;y|x_2) = I(x_2;y)\,.$$

Thus, I_A is an achievable rate for "User 1".

We now prove that I_A has a cut-off rate. Since, $I(x_2;y|x_1)$ is a non-decreasing function of P/N [74], there exists SNR_c such that $I(x_2;y|x_1) = R_2$, and hence

$$I_A(\mathrm{SNR}_c) = 0\,.$$

On the other hand, for a small $\varepsilon > 0$, it holds $R_2 = I(x_2;y|x_1) - \delta$ where $\delta > 0$. It follows that $I(x_1;y|x_2) > I(x_1,x_2;y) - R_2$. Thus

$$I_A(\mathrm{SNR}_c + \varepsilon) = I(x_1,x_2;y) - R_2 > I(x_1;y) > 0$$

for $\varepsilon \to 0^+$. □

Discussion. The proof of the lemma can be done graphically by considering the intersection of the achievable region with a horizontal line at height R_2.

When $R_2 > I(x_2;y|x_1)$ clearly the rate of "User 2" cannot be achieved. However, we also have to account for this case, and therefore we also consider the achievable rate $I(x_1;y)$, which is the relevant rate when "User 2" is just considered as interference. In this case, the receiver exploits the statistical knowledge of the signal $s_2(t)$ but does not attempt to recover the relevant information. Particularly, the receiver does not include the decoder for "User 2".

Lemma 2. *The rate $I_S(P/N) = I(x_1;y)$ as a function of P/N is always greater than* 0 and satisfies

$$\begin{aligned} I_S(\mathrm{SNR}_c) = &\lim_{\varepsilon \to 0^+} I_A(\mathrm{SNR}_c + \varepsilon) \\ I_S(\mathrm{SNR}_c + \delta) < &\ I_A(\mathrm{SNR}_c + \delta) \end{aligned}$$

for any $\delta > 0$.

Proof. The proof is straightforward. It can be done by observing that $I(x_1;y) \leq I(x_1;y|x_2)$ and that $I(x_1;y) \leq I(x_1,x_2;y)$. □

The computation of the AIRs $I(x_1;y|x_2)$, $I(x_2;y|x_1)$, $I(x_1,x_2;y)$, $I(x_1;y)$ can be performed by using the achievable lower bound based on mismatched detection [7]. Having defined I_A and I_S as the maximum rates achievable by "User 1" when the other user can be perfectly decoded, or not, we can now compute the AIR for "User 1" by means of the following theorem.

Theorem 1. *The AIR for a single user on the two users MAC, for a fixed rate R_2, is given by*

$$R_1 \leq \max\{I_S, I_A\}, \tag{4.6}$$

and is a continuous function of P/N.

Proof. Proof made by means of the Lemmas. In fact, I_A and I_S are the maximum rates achievable by "User 1" when "User 2" can be perfectly decoded, or not, respectively. An alternative graphical proof can be derived from Figure 4.3, which plots the rate

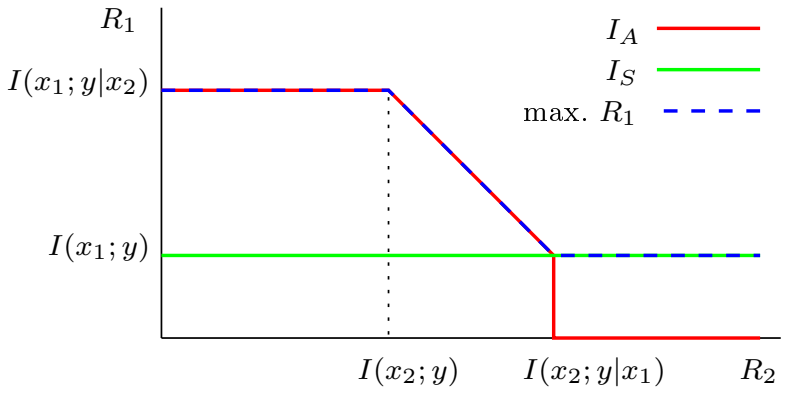

Figure 4.3: Graphical proof of Theorem 1.

achievable by "User 1" as a function of R_2, for a generic fixed value of P/N. We clearly see that inequality (4.6) is satisfied. □

Example 1. *For Gaussian symbols and $U = 2$, we obtain that*

$$R_1 \leq \begin{cases} \mathcal{G}\left(\frac{P}{N}\right) & \text{if} \quad R_2 \leq \mathcal{G}\left(\frac{P\gamma^2}{N+P}\right) \\ \mathcal{G}\left(\frac{P(1+\gamma^2)}{N}\right) - R_2 & \text{if} \quad \mathcal{G}\left(\frac{P\gamma^2}{N+P}\right) < R_2 \leq \mathcal{G}\left(\frac{P\gamma^2}{N}\right) \\ \mathcal{G}\left(\frac{P}{N+P\gamma^2}\right) & \text{if} \quad R_2 > \mathcal{G}\left(\frac{P\gamma^2}{N}\right), \end{cases}$$

where $\mathcal{G}(x) = \log_2(1+x)$. All curves are shown in Figure 4.4, for the case of $|\gamma| = 0.79$, $R_2 = 1/2$, and the overall bound is given by the red curve. We can see from the figure that this bound is clearly continuous.

When a SUD is employed at the terminal, the theoretic analysis can be based on the following discrete-time model

$$y = x_1 + w,$$

where w includes the thermal noise and the interferers that the receiver ignores. As known, the complexity of the SUD is much lower than that of the multiuser receiver, and is proportional to $M^{(1)}$. The computation of the AIR $I(x_1;y)$ is again based on

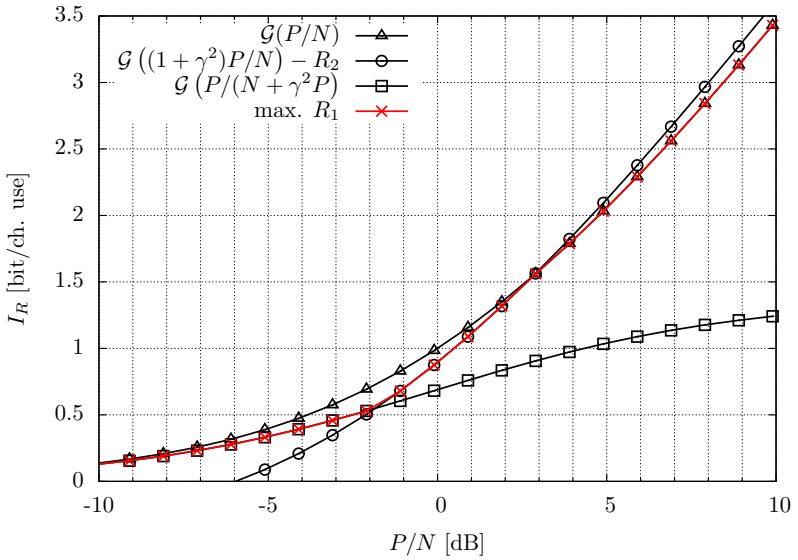

Figure 4.4: Maximum rate achievable by "User 1", for $U = 2$, Gaussian symbols, and $R_2 = 1/2$.

mismatched detection [7] and allows us to select the maximum rate for "User 1" when the co-channel interference is not accounted for.

We now consider **scenario 2** and, without loss of generality, we consider the fraction α of time when both signals $s_1(t)$ and $s_2(t)$ are used to send information to "User 1". The receiver is based on the channel model (4.2), but now the rate of signal $s_2(t)$ is not fixed. Since $s_1(t)$ and $s_2(t)$ are independent, we are exactly in the case of the MAC and, by properly selecting the rates of the two signals, any point of the capacity region can be achieved [66]. Clearly, we are interested in selecting the two rates in such a way that the sum-rate $I(x_1, x_2; y)$ is maximized.

In **scenario 3**, the two observed signals for the Alamouti processing at the terminal of "User 1" are

$$y_{\mathrm{A},1} = x_1 + \gamma x_2 + w_{\mathrm{A},1}$$
$$y_{\mathrm{A},2} = -x_2^* + \gamma x_1^* + w_{\mathrm{A},2}$$

where $w_{\mathrm{A},1}, w_{\mathrm{A},2}$ are independent Gaussian random variables with power N. After the

receiver processing [60], the observable for detection is

$$\tilde{y}_{\mathrm{A},i} = \sqrt{1+|\gamma|^2}x_i + \tilde{w}_{\mathrm{A},i} \quad i = 1,2\,, \tag{4.7}$$

and is still a sufficient statistic for detection. The information carried by $\tilde{y}_{\mathrm{A},2}$ is discarded and the AIR for "User 1" is that of an interference free channel with SNR $(1+|\gamma|^2)P/N$, divided by 2 to take into account the two consecutive transmission intervals necessary.

4.3 EXIT Chart Analysis

In this section, we analyze the convergence behavior of the schemes based on multiuser detection by means of an EXIT chart analysis [87]. The aim is to evaluate the convergence behavior of joint detection/decoding schemes in **scenario 1** and **scenario 2**, and to design novel practical schemes with performance close to the theoretical limits.

In the following description, we assume the presence of only two independent signals, those processed by the receiver of "User 1", but the results in Section 4.4 will be generated according to the general model (4.1). Each transmitted signal is obtained through a concatenation of a code with a modulator through a bit interleaver. The information data $\mathbf{b}_i$ of signal i is encoded by the encoder $\mathcal{C}_i$ with rate $r^{(i)}$ into the codeword $\mathbf{v}_i$, which is interleaved and mapped through a modulator $\mathcal{M}_i$ onto a sequence of $M^{(i)}$-ary symbols $\mathbf{x}_i$. Here, the channel model is the vectorial extension of the model (4.2), which allows us to consider sequences of symbols.

The joint detection/decoding scheme consists of a multiuser detection module $\mathcal{M}_{\mathrm{MU}}^{-1}$, and two *a posteriori* probability decoders $\mathcal{C}_1^{-1}$ and $\mathcal{C}_2^{-1}$ matched to the encoders $\mathcal{C}_1$ and $\mathcal{C}_2$ of the two transponders. The described system is reported in Figure 4.5.

The SISO MUD exchanges soft information with the two decoders $\mathcal{C}_1^{-1}$ and $\mathcal{C}_2^{-1}$, in an iterative fashion. More generally, the detector and the decoders can also be composed by SISO blocks. In this chapter, we focus on LDPC codes, whose decoder is composed of sets of variable and check nodes (the variable-node decoder (VND) and

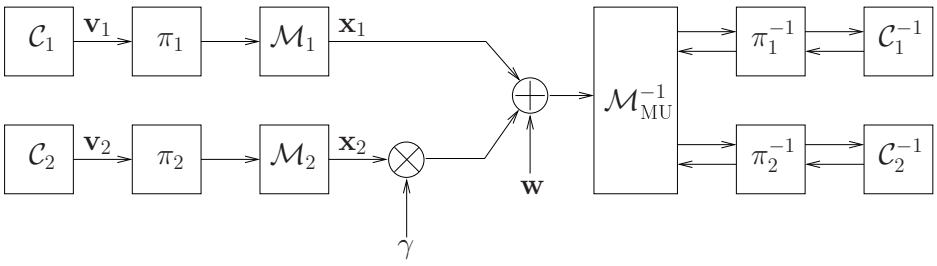

Figure 4.5: Block diagram of the considered system.

check-node decoder (CND)). Iterative decoding is performed by passing messages between variable and check nodes. We distinguish between *local* iterations, within each LDPC decoder, and *global* iterations, between the MUD and the two decoders. A global iteration consists of a single local iteration of decoders $\mathcal{C}_1^{-1}$ and $\mathcal{C}_2^{-1}$ and a single activation of the detector $\mathcal{M}_{\mathrm{MU}}^{-1}$. Accordingly, the iterative decoding process can then be tracked using a multi-dimensional EXIT chart. Alternatively, the EXIT functions of the constituent decoders and of the MUD can be properly combined and projected into a two-dimensional chart [89]. Similar to a system composed by only two SISO blocks, the convergence threshold of our system can be visualized as a tunnel between the two curves in the projected EXIT chart.

Let $I_{E_{\mathbf{v}_i}^{\mathcal{C}_i}}$ denote the extrinsic mutual information (MI) generated by decoder $\mathcal{C}_i^{-1}$ of user i on codeword $\mathbf{v}_i$ at the output of $\mathcal{C}_i$. Also, let $I_{E_{\mathbf{v}_i}^{\mathcal{M}_{\mathrm{MU}}}}$ be the extrinsic MI generated by the MUD on codeword $\mathbf{v}_i$ (more precisely on its interleaved version). Correspondingly, denote by $I_{A_{\mathbf{v}_i}^{\mathcal{C}_i}}$ and $I_{A_{\mathbf{v}_i}^{\mathcal{M}_{\mathrm{MU}}}}$ the *a priori* MI at the input of decoder $\mathcal{C}_i^{-1}$ and of $\mathcal{M}_{\mathrm{MU}}^{-1}$, respectively. $I_{E_{\mathbf{v}_i}^{\mathcal{C}_i}}$ is a function of $I_{A_{\mathbf{v}_i}^{\mathcal{C}_i}}$, while $I_{E_{\mathbf{v}_i}^{\mathcal{M}_{\mathrm{MU}}}}$ is a function of $I_{A_{\mathbf{v}_i}^{\mathcal{M}_{\mathrm{MU}}}}$, for $i = 1,2$, of the channel SNR P/N, and of the channel gain γ:

$$\begin{aligned} I_{E_{\mathbf{v}_i}^{\mathcal{C}_i}} &= T^{\mathcal{C}_i}\left(I_{A_{\mathbf{v}_i}^{\mathcal{C}_i}}\right), \\ I_{E_{\mathbf{v}_i}^{\mathcal{M}_{\mathrm{MU}}}} &= T^{\mathcal{M}_{\mathrm{MU}}}\left(I_{A_{\mathbf{v}_1}^{\mathcal{M}_{\mathrm{MU}}}}, I_{A_{\mathbf{v}_2}^{\mathcal{M}_{\mathrm{MU}}}}, P/N, \gamma\right). \end{aligned} \tag{4.8}$$

Notice that $I_{A_{\mathbf{v}_i}^{\mathcal{C}_i}} = I_{E_{\mathbf{v}_i}^{\mathcal{M}_{\mathrm{MU}}}}$ and $I_{A_{\mathbf{v}_i}^{\mathcal{M}_{\mathrm{MU}}}} = I_{E_{\mathbf{v}_i}^{\mathcal{C}_i}}$. The EXIT functions in (4.8) can be computed by Monte Carlo simulations of the individual component blocks using a Gaus-

sian approximation of the related a priori values. We combine now the EXIT functions of encoder 2 and of the MUD in a single EXIT function, which we denote by $I_{E_{\mathbf{v}_1}^{\mathcal{C}_\mathrm{H}}} = T^{\mathcal{C}_\mathrm{H}}\left(I_{A_{\mathbf{v}_1}^{\mathcal{C}_\mathrm{H}}}, P/N, \gamma\right)$, where $I_{A_{\mathbf{v}_1}^{\mathcal{C}_\mathrm{H}}} = I_{E_{\mathbf{v}_1}^{\mathcal{C}_1}}$. Now, the iterative process can be tracked by displaying in a single plot the EXIT function of "User 1", $I_{E_{\mathbf{v}_1}^{\mathcal{C}_1}}$, and the EXIT function $I_{E_{\mathbf{v}_1}^{\mathcal{C}_\mathrm{H}}}$. $I_{E_{\mathbf{v}_1}^{\mathcal{C}_\mathrm{H}}}$ can be computed for all values $0 \leq I_{A_{\mathbf{v}_1}^{\mathcal{C}_\mathrm{H}}} \leq 1$ by activating the decoder $\mathcal{C}_2^{-1}$ and $\mathcal{M}_{\mathrm{MU}}^{-1}$ until $I_{E_{\mathbf{v}_1}^{\mathcal{C}_\mathrm{H}}}$ has converged to a fixed value.

Clearly, the performance of this multiple concatenated system depends on the schedule of activation of the component blocks. On the other hand, in [89] it is shown that the limit behavior is independent of the activation schedule, provided that the EXIT functions of the constituent SISO blocks are monotonically nondecreasing, which is the case of any useful code and detector, and the blocks are activated until no further gain is possible.

The system in Figure 4.5 can represent both **scenario 1** and **scenario 2**. We recall that, in the first scenario, the information to recover is conveyed by signal 1 only, while the rate of the other signal is fixed. Our design will be thus aimed at finding a good code $\mathcal{C}_1$, while the code for the other signal cannot be changed and will be chosen among those foreseen by the DVB-S2 standard [35]. In the case of **scenario 2**, the scheme in Figure 4.5 is representative of the fraction of time in which both signals are carrying information for "User 1". In this case, we assume to have the freedom to choose the code of the two signals and also to apply a joint bit mapping, as we will see in Section 4.4.2. Moreover, if we assume that $|\gamma| = 1$, the convergence analysis strongly simplifies, since it is reasonable to assume that the two transponders employ the same code and modulation format. In this special case, we have that $I_{E_{\mathbf{v}_1}^{\mathcal{C}_1}} = I_{E_{\mathbf{v}_2}^{\mathcal{C}_2}}$ and the EXIT chart can be directly visualized in two dimensions, by plotting the MI curve of the MUD and of the decoder.

4.4 Numerical Results

We assume as reference system the DVB-S2 standard [35]. We choose an aggressive frequency reuse, to generate a high co-channel interference, and consider 6 users,

Case	λ_2	λ_3	λ_4	λ_5	λ_6
1	0 dB	25 dB	25 dB	27 dB	30 dB
2	2 dB	26 dB	26 dB	27 dB	30 dB
3	4 dB	27 dB	26 dB	27 dB	30 dB

Table 4.1: Power profiles for the considered simulations, corresponding to a two-color frequency reuse.

which are located close to the edge of the coverage area of the reference beam. To identify the users' power profile, we define the signal-to-interference power ratio as

$$\lambda_i = |\gamma_1|^2/|\gamma_i|^2,$$

and consider three realistic cases which have a different power profile, listed in Table 4.1. These distributions are typical of the forward link of a multibeam broadband satellite system with two-color frequency reuse.

For the first two scenarios, we assume that "User 1" adopts a QPSK modulation, therefore the signal with $i = 1$ in **scenario 1**, and signals 1 and 2 in **scenario 2** use a QPSK. "User 1", in **scenario 3**, adopts a 16APSK modulation so that we have the same receiver complexity as in **scenario 2**. In the case of **scenario 1**, the performance is heavily affected by the rate of "User 2": in order to fix the rate of signal 2, we consider the MODCODs distribution shown in Figure 4.6. The other signals adopt the following modulation formats in all scenarios: 8PSK for signals with $i = 3,4$ and 6, and 16APSK for the signal with $i = 5$. In the case of **scenario 2**, $\alpha = 0.5$ is assumed.

Figures 4.7–4.9 show the AIR, measured in bit per channel use, of "User 1" as a function of P/N, for the three considered interference patterns. In the case of **scenario 1**, we evaluate both the AIR achievable by a SUD and that achievable by the MUD$\times$2 algorithm, and the reported curves are obtained by computing the AIRs when "User 2" adopts the MODCODs in Figure 4.6, and then averaging according to their distribution.

Our results show that we cannot identify the strategy which universally achieves

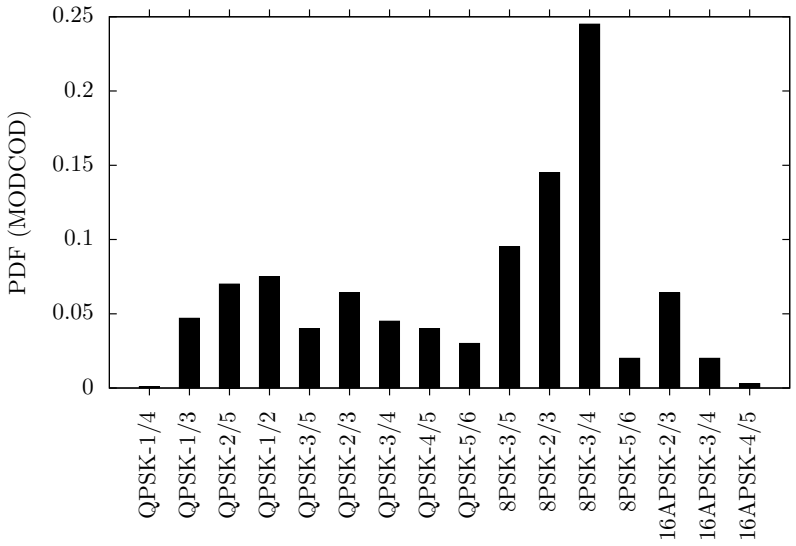

Figure 4.6: Typical MODCODs distribution.

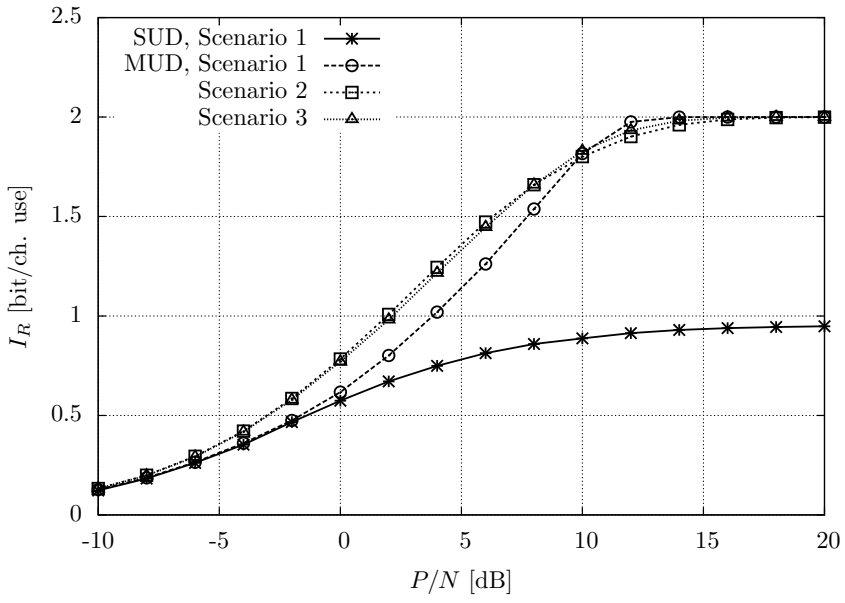

Figure 4.7: AIR of “User 1” for case 1 and the three considered scenarios.

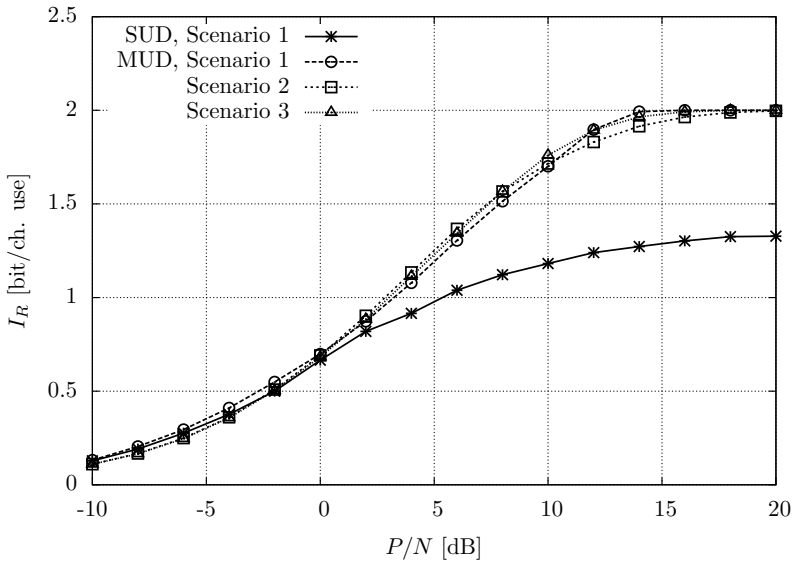

Figure 4.8: AIR of "User 1" for case 2 and the three considered scenarios.

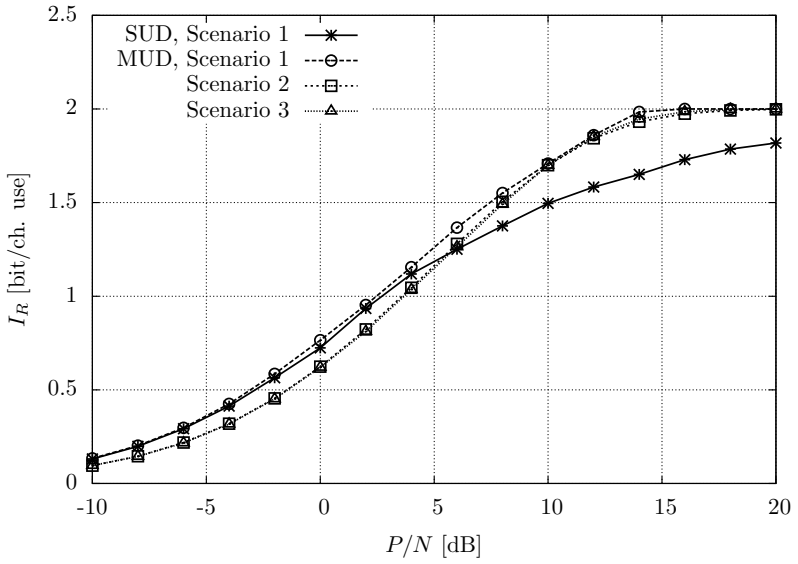

Figure 4.9: AIR of "User 1" for case 3 and the three considered scenarios.

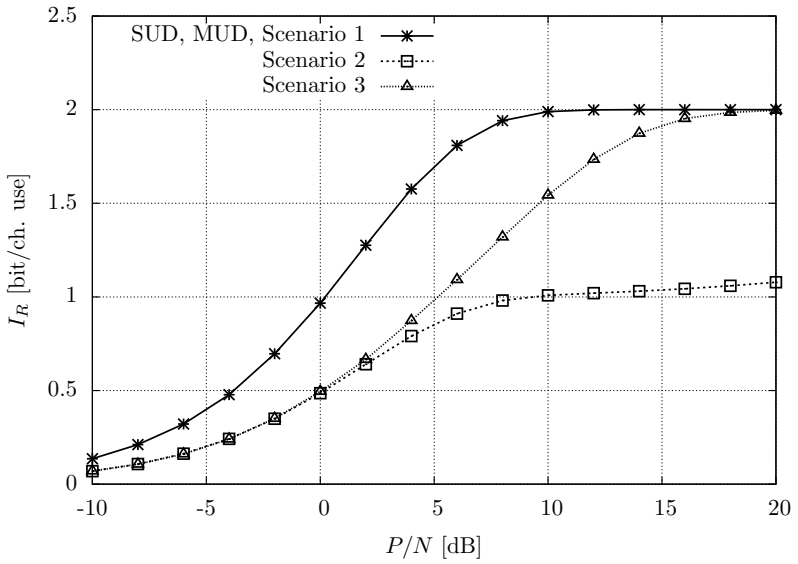

Figure 4.10: Information rate of "User 1" when it is located at the center of the beam.

the best performance. In particular, the figures show that "User 1" has the best AIR in **scenario 2** and **scenario 3** in the first case, where the interference of the second signal is very strong, while in the third case it has higher AIR in **scenario 1** for low-to-medium SNR values. In the second case the three strategies offer similar performance when the MUD is applied in **scenario 1**. As expected, in **scenario 1** the adoption of the MUD gives the best results with respect to the SUD, at the price of an increased complexity. In case 3, the SUD gives very good AIRs, and hence it is the best choice to compromise between complexity and performance for a large SNR range.

It is worth noting that, while all the proposed strategies are very effective when "User 1" is close to the edge of the beam, this is not always true if the user is located at the center of the beam. In Figure 4.10, we report the AIR in a case in which the power of the signal $s_2(t)$ tends to 0: the best strategy is the classical one, and the AIR in the case of **scenario 2** is highly degraded since half of the data for "User 1" cannot be recovered. This fact calls for a performance evaluation at system level.

We now consider practical MODCODs based on multiuser detection and the

Alamouti precoder and we focus on the gap between practical and theoretical performance. In the following, we will not consider the SUD of **scenario 1**. As shown by the information theoretic analysis, it is not easy to compare the three scenarios, since the best strategy depends on the power profile of the interfering signals, the rates of the signals, and the SNR. Figure 4.11 shows the AIR in case 1. In **scenario 1**, the AIR curve is no more the average AIR with respect to the distribution 4.6, but the signal $s_2(t)$ is assumed to adopt an 8PSK. We first consider MODCODs based on the LDPC codes with rates 1/2 and 3/4[2], with length 64800 bits, of the DVB-S2 standard, with the corresponding interleavers. In **scenario 1**, we use the rate 3/4 LDPC code for signal $s_2(t)$, in order to simulate the most probable MODCOD according to the distribution in Figure 4.6. In the first two scenarios, we consider iterative detection and decoding and allow a maximum of 50 global iterations. The BER results have been computed by means of Monte Carlo simulations and are reported in the AIR plane in Figure 4.11 using, as reference, a BER of 10^{-4}. These results show that schemes based on the Alamouti precoding and the codes of the standard have good performance, being the loss with respect to the corresponding AIR curve around 1 dB. This is because only single-user operations are performed. On the contrary, the loss of practical MODCODs with respect to the AIR limits is high for both scenarios 1 and 2, being about 2 and 4 dB at $I_R = 1$ and 1.5 bit/ch. use, respectively.

In the following sections, we will try to reduce this loss by redesigning the code of "User 1". Furthermore, we will adopt the joint bit mapping proposed in Section 3.8 in **scenario 2**, where we have greater design freedom since both signals are for "User 1". Our design approach is based on EXIT charts: this tool is able to point out the limits of the DVB-S2 based MODCODs and provides very useful insights on the code and mapper design. We will limit the analysis to case 1, but the same tools can be applied to the other power profiles.

[2]The adoption of these two code rates for "User 1" corresponds to AIR 1 and 1.5 bit/ch. use, respectively.

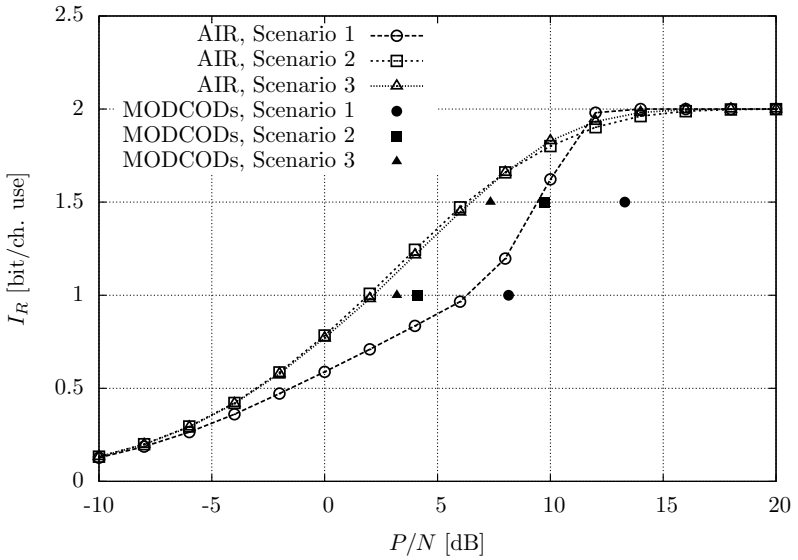

Figure 4.11: AIR and MODCODs of "User 1" in case 1.

4.4.1 LDPC Design for Iterative Detection/Decoding

Figure 4.12 shows the EXIT chart for **scenario 2** in case 1. The MI curve of the MUD has been obtained for $P/N = 3$ dB, while the considered codes have rate 1/2. Let us first focus on the MI curve of the LDPC code of the DVB-S2 standard. As already pointed out in Section 3.8, the EXIT chart analysis reveals that the DVB-S2 codes do not fit the detector, which means that codes which have been designed for systems employing single-user detection, are not the best choice for the considered MUD schemes. The EXIT chart of **scenario 1** has similar features. This observation pushes us towards the redesign of the LDPC code.

The EXIT chart analysis clearly suggests that, in our scenario, we need an LDPC code that is more powerful at the beginning of the iterative process, to have a better curve matching between detector and decoder. This is not surprising since, in interference-limited channels, a SISO detector is effectively able to mitigate the interference when the information coming from the decoders is somehow reliable. In other words, we mainly need a good head start. We adopt the heuristic technique for

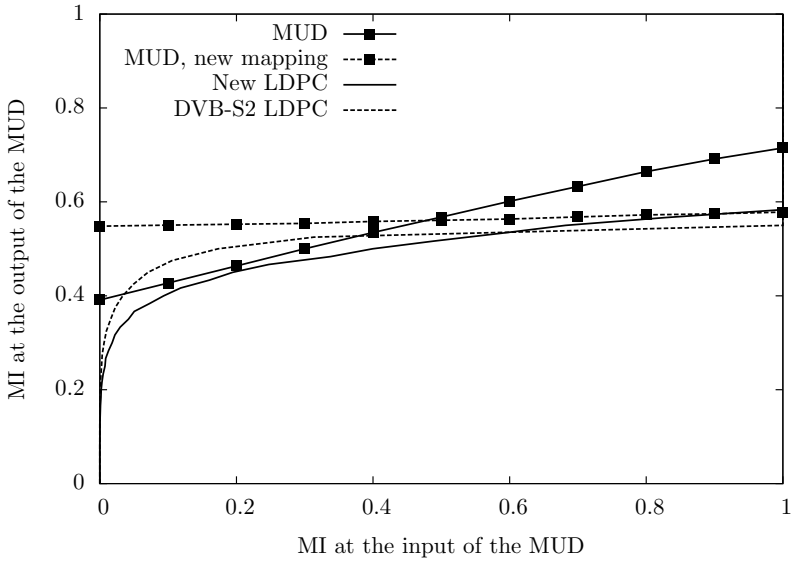

Figure 4.12: EXIT chart for scenario 2 in case 1 at $P/N = 3$ dB.

Scen.	Rate	VND distribution	CND distribution
1	1/2	2 (60%) 3 (31.4%) 10 (8.6%)	6 (100%)
2	1/2	2 (60%) 3 (36.5%) 20 (3.5%)	6 (100%)
1	3/4	2 (80%) 3 (18.3%) 50 (1.7%)	12 (100%)
2	3/4	2 (70%) 3 (28.5%) 50 (1.5%)	12 (100%)

Table 4.2: Details of designed LDPC codes.

the optimization of the degree distribution of the LDPC variable and check nodes proposed in [81]. This method consists of a curve fitting on EXIT charts. We optimize the VND and CND distribution, limiting for simplicity our optimization procedure to codes with uniform check node distribution and only three different variable node degrees. The EXIT curve of the new LDPC is shown in Figure 4.12.

Using this approach, for each scenario we could design a rate 1/2 and a rate 3/4 LDPC code, whose parameters are summarized in Table 4.2. The codes of length 64800 are then obtained by using the PEG algorithm [90] and the performance is

Scen.	Rate	AIR th.	DVB Code (gap)	New Code (gap)	New Map. (gap)
1	1/2	6.3 dB	8.15 dB (1.85)	7.4 dB (1.1)	
2	1/2	1.95 dB	4.1 dB (2.15)	3.05 dB (1.1)	2.75 dB (0.8)
1	3/4	9.45 dB	13.3 dB (3.85)	11.75 dB (1.55)	
2	3/4	6.25 dB	9.75 dB (3.5)	7.9 dB (1.65)	6.95 dB (0.7)

Table 4.3: BER convergence thresholds for the proposed solutions.

reported in Table 4.3. For **scenario 2** we have used two different codes, but with the same degree distribution, for the two signals in order to increase the diversity between them.

4.4.2 Joint Bit Mapping for Scenario 2

After the observation of the poor match between the curves in the EXIT chart, in Section 4.4.1 we have seen how to improve the threshold by properly changing the code. Here, instead, we propose an alternative approach which is focused on the MI curve of the detector. In particular, we apply the joint bit mapping proposed in Section 3.8 to the two signals in **scenario 2**. As mentioned, this cooperative approach works exceptionally well in conjunction with the DVB-S2 codes. The idea behind this solution comes from the fact that transmitting a single signal with Gray mapping gives rise to a practically horizontal EXIT curve for the detector [58], that is exactly what we need if we want to use the codes of the standard. Indeed, the EXIT curve of the MUD with joint mapping has much smaller slope than that related to the classical mapping, as shown in Figure 4.12. We recall that the adopted joint constellations and mapping are those shown in Figures 3.23 and 3.24.

Table 4.3 summarizes the BER results, at AIR 1 and 1.5 bit/channel use, in terms of convergence threshold, defined as the P/N corresponding to a BER of 10^{-4}. We also report the AIR limit in P/N obtained through the information-theoretic analysis. The results show that the gap between the theoretical and the convergence thresholds can be reduced thanks to the new LDPC codes and the joint bit mapping.

4.5 Conclusions

In this chapter, we have considered the forward link of a multibeam satellite system, where a MUD is employed to increase the achievable rates in the presence of strong co-channel interference. We have shown that multiuser detection can considerably increase the achievable rate at the cost of a higher computational complexity.

Furthermore, we have considered two alternative transmission strategies, where the signals from two beams serve two users in a TDM way or employing the Alamouti space-time block code. We have shown that these approaches are effective when the co-channel interference is very strong. The conclusive picture is complex, since our results demonstrate that a transmission/detection strategy which is universally superior to the others does not exist, but the performance depends on several factors, such as the SNR, the users' power profile, and the rate of the strongest interferer. This fact outlines the importance of the proposed analysis framework, which allows to avoid computationally intensive simulations.

Finally, we have analyzed the performance of coded schemes employing joint multiuser detection/decoding, and showed that the theoretical bounds can be approached thanks to the redesign of the code and/or of the bit mapping.

Chapter 5

Spectral Efficiency Improvements of Earth Observation Links

This chapter investigates the possible improvements of the ASE in Earth observation (EO) links by applying some advanced techniques at the transmitter and at the receiver. We will analyze two different scenarios, with one and two channels, respectively. For both scenarios, we will perform an optimization of the symbol rate and apply techniques such as TFP at the transmitter and more sophisticated detectors at the receiver. Section 5.1 deals with the single channel scenario, while Section 5.2 presents the scenario with two channels. Finally, Section 5.3 concludes the chapter.

5.1 Single Channel Scenario

The first scenario analyzed in this chapter is that depicted in Figure 5.1. The information bits to be transmitted to Earth are mapped on K symbols of an $M-$ary zero-mean complex constellation to generate the sequence $\{x_k\}_{k=0}^{K-1}$. We can express the complex envelope of the transmitted signal as

$$x(t) = \sum_{k=0}^{K-1} x_k p(t - kT_s),$$

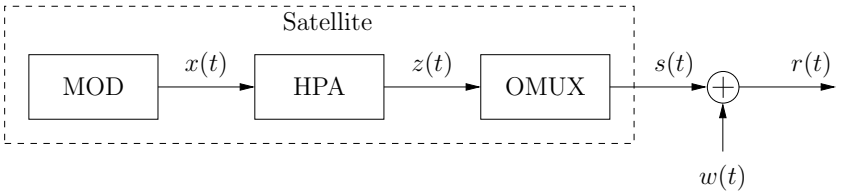

Figure 5.1: Block diagram of the transmitter for the single channel scenario.

where the shaping pulse $p(t)$ is an RRC pulse with roll-off factor $\alpha = 0.35$ and T_s is the symbol interval. The HPA AM/AM and AM/PM characteristics are those foreseen by the DVB-S2 standard [35] and reported in Figure 2.2, while the OMUX filter is a 5-th order elliptic filter [91] with a ripple of 0.1 dB, passband $B_\mathrm{p} = 600$ MHz and stopband $B_\mathrm{s} = 750$ MHz. The amplitude response of the adopted filter is shown in Figure 5.2. The reference system operates with a symbol rate $R_\mathrm{s} = 500$ Mbaud and allows the use of the static DPD described in [57] to help compensating the nonlinear distortions introduced by the HPA. The received signal is then affected by an AWGN process, whose low-pass equivalent $w(t)$ has power spectral density N_0. The received signal has expression

$$r(t) = s(t) + w(t)\,,$$

where $s(t)$ is the signal at the output of the transponder.

At the receiver, for the reference scenario, we will adopt the FS-MMSE equalizer described in Section 2.3, followed by a symbol-by-symbol detector. As already done in previous chapters, we will use, as a figure of merit, the ASE of the system, defined as

$$\mathrm{ASE} = \frac{I_R}{T_s B_\mathrm{p}} \quad [\mathrm{bit/s/Hz}],$$

where I_R is the maximum AIR of the channel.

5.1.1 Optimization of the Reference Architecture

For the optimization of this reference system, we consider the application of advanced techniques at both the transmitter and receiver sides. The analyzed solutions are sim-

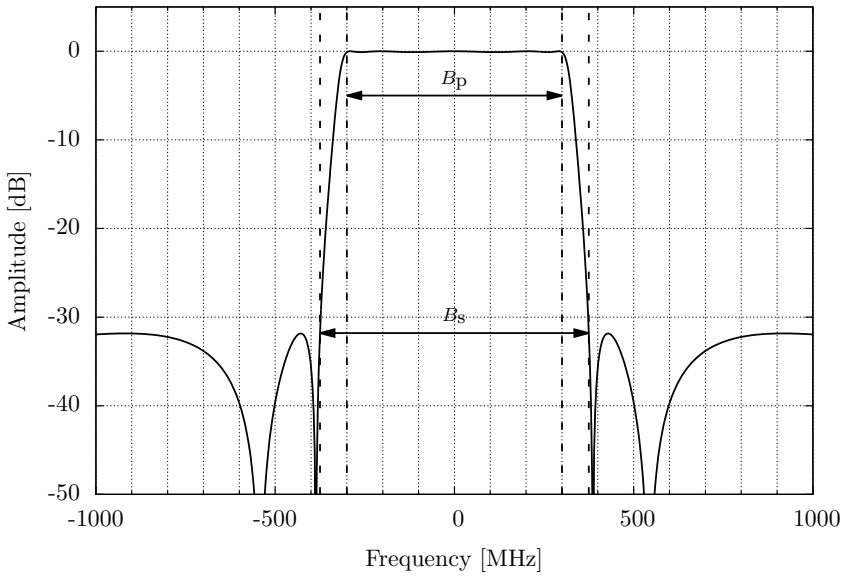

Figure 5.2: Adopted OMUX filter for the single channel EO scenario.

ilar to those applied in Chapter 2, and they can be summarized as follows. The reader can refer to Chapter 2 for a more detailed characterization of the different techniques.

The optimization of the symbol rate and of the signal bandwidth. The symbol rate and the roll-off factor of the pulse $p(t)$ can be jointly optimized to find the best setting for a fixed bandwidth of the OMUX filter. Hence, we will consider the adoption of lower roll-off values and an increased symbol rate.

The application of the time packing technique. The symbol interval can be decreased to improve the ASE. We can define the symbol interval as $T_s = \tau T$, where T is half of the main lobe duration of $p(t)$ and $\tau \leq 1$ is the time packing factor, which will be properly selected to maximize the efficiency of the system.

The use of a more sophisticated receiver. The increased ISI introduced by the two previously mentioned techniques can be more effectively coped with by adopting a more sophisticated detector, able to take into account part of the channel memory. We will then adopt the adaptive CS receiver described in Section 2.3, which consists of an FS equalizer, an adaptive CS filter and a BCJR detector. When the channel

memory at the detector is set to $L = 0$, this scheme is equivalent to the FS-MMSE of the reference scenario.

The use of more advanced predistortion algorithms. In a scenario like the DVB-S2 model, the information is generated on Earth and transmitted through a satellite channel. In this EO scenario, instead, data is generated directly on the satellite. This fact allows us to use a signal predistorter (SPD) instead of a DPD. SPDs have been widely studied in the literature [92–94] due to their ability to work on the samples of the continuous time signal rather than on the transmitted symbols. However, their use in a conventional DVB-S2 scenario is not feasible: in fact, an SPD usually tries to invert the nonlinearity introduced by the HPA. The presence of an IMUX filter between the SPD and the HPA does not allow an effective compensation of the nonlinear effects. In this EO scenario, however, there is no need for the IMUX filter, so the use of an SPD is a promising solution.

The block diagram of the SPD we propose in this chapter is shown in Figure 5.3. We model the signal at the output of the SPD, as also done in [93], as

$$v(t) = \sum_{s=0}^{S} g_s x(t)|x(t)|^{2s}, \tag{5.1}$$

that is, as a memoryless Volterra series taking into account odd order terms only. The complex coefficients $\mathbf{g} = \{g_s\}_{s=0}^{S}$ in (5.1) are selected to minimize the MSE between the transmitted signal $x(t)$ and the signal at the output of the HPA, $z(t)$:

$$\mathbf{g} = \underset{\mathbb{C}^{S+1}}{\operatorname{argmin}} \mathrm{E}\left[|z(t) - x(t)|^2\right]. \tag{5.2}$$

The block "SPD computation" in Figure 5.3 performs the minimization (5.2) through the algorithm described in [95] and included in the nonlinear optimization package [96].

5.1.2 Numerical Results

We adopt the classical constellations used in satellite communications, from QPSK to 64APSK, optimizing the IBO for every case. Figure 5.4 shows the ASE of the system with an optimized symbol rate, in comparison with the reference scenario. The

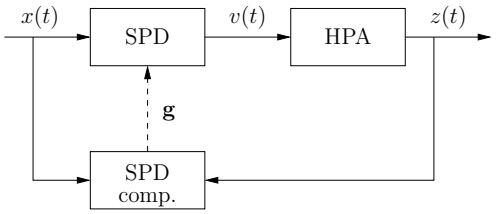

Figure 5.3: Block diagram of the proposed SPD.

roll-off factor is set to $\alpha = 0.35$ for all curves. We also compare the performance of the static DPD of [57] with the SPD proposed in the previous section, with $S = 2$ (that is, modeled as a fifth order nonlinearity), for increasing values of the memory considered at the receiver, $L = 0, 1$. The details on the symbol rate for the curves of Figure 5.4 are reported in Table 5.1. We can notice that the performance of the two predistortion algorithms is similar, both in terms of ASE and maximum allowed symbol rate, especially in the medium-low SNR range. We also notice that, in this range, increasing the complexity of the detector can provide only very limited advantages. More relevant differences arise in the high SNR region, where the DPD and the detector with $L = 1$ grant the highest ASE. In all cases, however, the gains over the reference scenario are significant. We also mention that we have performed the same analysis by using reduced roll-off values, namely 0.2 and 0.1, but the results do not improve with respect to the reference value of 0.35. For this reason, we will not apply roll-offs other than 0.35 in the rest of the chapter.

We next consider the application of time packing. For this analysis, only the DPD has been applied, but similar results can be expected for the SPD. Figure 5.5 shows the ASE for QPSK and 8PSK when the value of τ has been optimized. The memory of the BCJR has been set to $L = 4$, which, we found, is practically optimal for this scenario. Both curves have been computed starting from the reference symbol rate $R_s = 500$ Mbaud. We see that, although the symbol time is optimized, time packing cannot reach the same performance as transmission with orthogonal signaling with increased symbol rate. In fact, Figure 5.5 also reports the ASE of 8PSK and 16APSK with optimized symbol rates. The latter curves achieve higher values of ASE with a

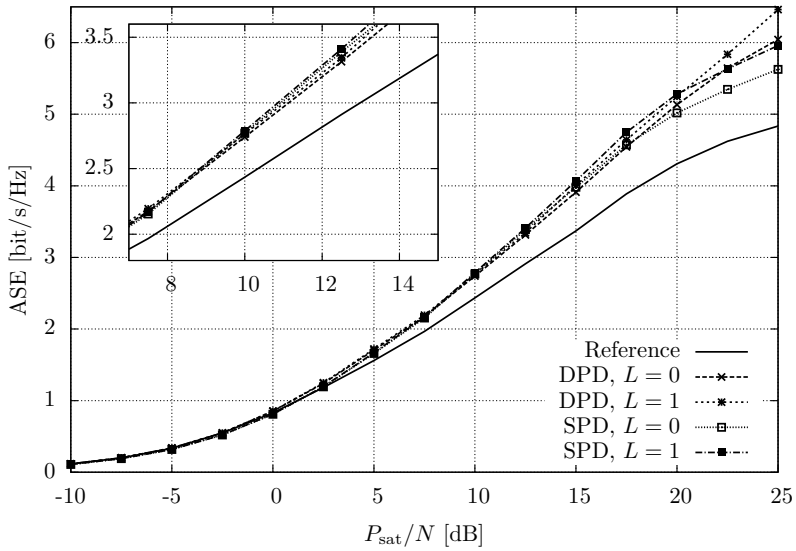

Figure 5.4: ASE for the single channel scenario and optimized symbol rate.

P_{sat}/N [dB]	DPD				SPD			
	$L=0$		$L=1$		$L=0$		$L=1$	
	M	R_{s}	M	R_{s}	M	R_{s}	M	R_{s}
-10	8	500	8	500	4	550	4	550
-5	8	550	8	550	4	500	4	500
0	8	600	8	600	8	600	8	600
5	8	650	8	650	8	650	8	650
10	16	650	16	650	16	650	16	650
15	32	650	16	850	32	650	16	850
20	64	650	32	800	32	650	16	850
25	64	650	64	800	64	650	32	850

Table 5.1: Optimized symbol rate R_{s} (in Mbaud) for the curves in Figure 5.4.

much lower complexity, relying only on a symbol-by-symbol detector, with $L = 0$. This result is somewhat expected, as it is in line with that obtained for a DVB-S2

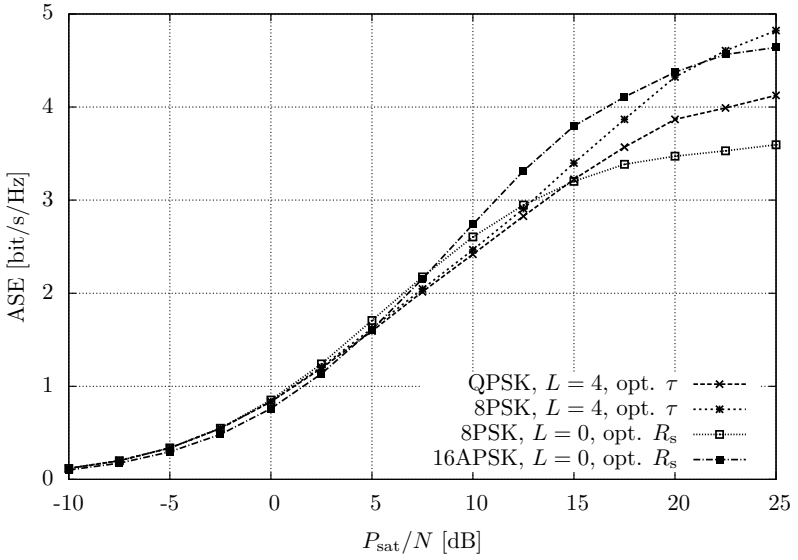

Figure 5.5: ASE for the single channel scenario and time packing.

scenario, discussed in Chapter 2. Hence, time packing will not be considered anymore for EO scenarios.

5.2 Two Channels Scenario

In this section, we extend the investigation to a system using two transponders on the same satellite. The block diagram of the transmitter, in this case, is a direct extension of that considered in the single channel scenario, and it is shown in Figure 5.6. The two HPAs and OMUX filters are identical, and they have the same characteristics as those of the previous section. The reference architecture still has the same transmission parameters, namely symbol rate $R_{\mathrm{s}} = 500$ Mbaud and RRC pulses with roll-off $\alpha = 0.35$. Moreover, for the reference scenario, we will consider the two channels to be spaced in frequency by $F = 750$ MHz. This value ensures that the passbands of the two OMUX filters do not overlap with each other, leaving an appropriate guard band between the two channels. The receiver will adopt two FS-MMSE equalizers

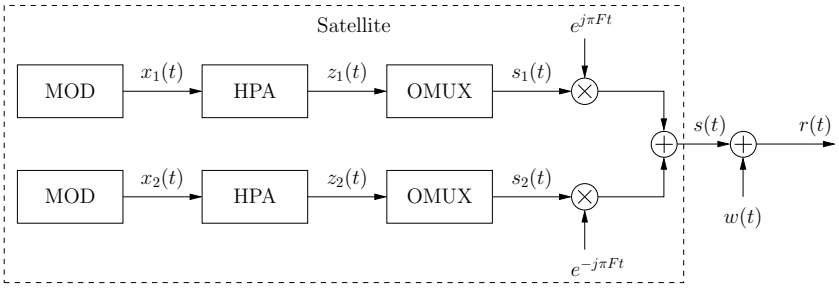

Figure 5.6: Block diagram of the transmitter for the two channels scenario.

followed by two SUDs, as already done in the single channel reference scenario.

To compute the ASE of this system, a bandwidth definition is required. In order to define the overall signal bandwidth, we can proceed as follows.

1. Compute the AIR of the system as the sum of the AIRs of the two channels.
2. After the signal are shifted in frequency, insert a filter with the same shape as the OMUX filters, but with passband B_{f} large enough to leave the two signals, and hence the AIR of the system, unchanged.
3. Progressively reduce B_{f} until a reduction in the AIR is observed.
4. Define the bandwidth of the system as the smallest value of B_{f} which causes a reduction of the AIR not greater than 1% with respect to the case without the filter.

With this procedure we could define the reference bandwidth as $B_{\mathrm{f}} = 1320$ MHz, and compute the ASE as

$$\mathrm{ASE} = \frac{I_R}{T_s B_{\mathrm{f}}} \quad [\mathrm{bit/s/Hz}].$$

5.2.1 Optimization of the Reference Architecture

Different techniques can be applied to improve the reference scenario. Some of them are similar to those used in the single channel case, while others take into account the presence of the second carrier, both at the transmitter and at the receiver sides.

Some predistortion techniques able to jointly operate on multiple channels have been proposed in the literature (refer to [97–100] for some examples), but they all assume to work in a multiple channels per transponder scenario. In our case, each channel has its own HPA, so we do not believe that said techniques are applicable as they are. Hence, following from the results in Section 5.1, we will apply only the static DPD and we will not consider time packing. The applied techniques are the following.

The optimization of the symbol rate. As already done previously, we will increase the symbol rate to the maximum value allowed by the bandwidth of the OMUX filters.

The application of the frequency packing technique. The central frequency of the two carriers can be selected, jointly with the symbol rate, to maximize the ASE. In fact, the presence of a guard band can be exploited to reduce the distance between the two carriers and increase the symbol rate, thus introducing a certain amount of ICI.

The use of a more sophisticated receiver. To cope with said interference, different receivers can be adopted. The adaptive CS filters can be followed not only by a SUD, as in the single channel case, but also by a MUD, which is expected to better handle the ICI arising from the application of the frequency packing technique, at the price of an increased complexity of the detection stage. To fully exploit the available bandwidth, we will then remove the two OMUX filters at the output of the transponders, and introduce a single large filter with bandwidth B_{f}. In this bandwidth, we will allow the two signals to be as overlapped as possible, and we will adopt both the SUD and the MUD. The block diagram of the transmitter for this new architecture is shown in Figure 5.7, where the BPF is a band-pass filter with bandwidth B_{f}.

The use of the Alamouti space-time block code. As already done in Chapters 3 and 4, we will also consider the Alamouti space-time block code [60] as a convenient alternative. In this way we can transmit fully overlapped signals and perform only single-user operations at the receiver. However, due to the processing foreseen by Alamouti, the same information has to be transmitted twice over two consecutive signaling intervals.

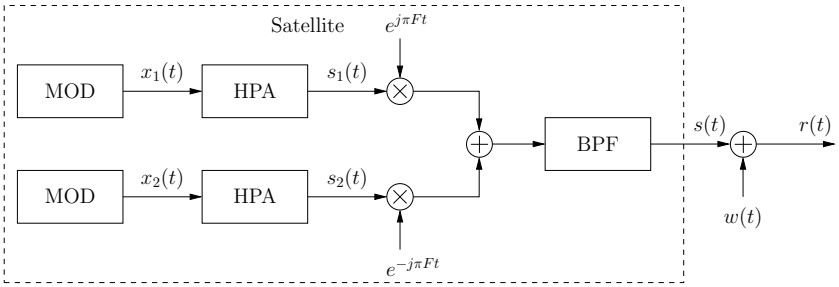

Figure 5.7: Evolution of the transmitter for the two channels scenario.

5.2.2 Numerical Results

Figure 5.8 compares the envelope of the ASE for different transceiver schemes, all considering a memory $L = 0$ at the detector, with modulations formats ranging from QPSK to 64APSK. In particular, the curve labeled *with OMUX* only differs from the reference in the symbol rate and central frequency of the two channels. We see that this optimization alone grants significant gains. Further small gains can be achieved by removing the two OMUX filters and introducing the single filter with bandwidth B_{f} (*no OMUX* curves). In this case, the SUD and the MUD have practically the same performance; this fact is not surprising, since they both perform symbol-by-symbol detection. Finally, the Alamouti scheme can outperform all other alternative techniques.

We then increased the memory considered at the detector. We point out that this investigation has been carried out only for the schemes without the two inner OMUX filters. This is because the increased ICI that arises when the filters are removed needs a higher complexity detector to be coped with. The resulting ASE curves are shown in Figure 5.9. If we compare them with the corresponding curves in Figure 5.8, we see that the SUD and the Alamouti schemes have only small benefits with respect to symbol-by-symbol detection, and only in the high SNR range. On the other hand, the gains of the MUD are very significant, even more if we consider that the curve with $L = 1$ has been obtained, for complexity reasons, only with 8PSK, while all other curves take into account modulation formats up to 64APSK. The optimized values

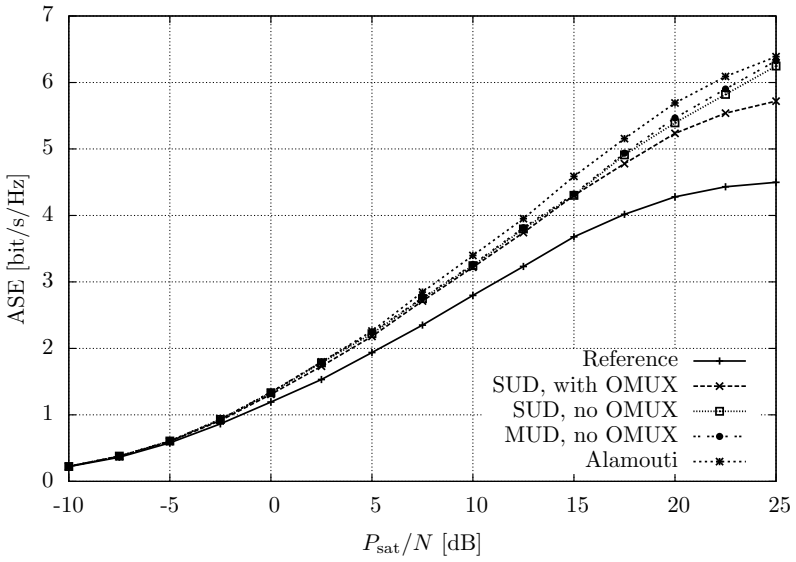

Figure 5.8: ASE for the two channels scenario with $L = 0$.

of symbol rate R_{s} and frequency spacing F for the MUD with $L = 1$ are reported in Table 5.2. We can notice that this scheme allows the signals to be almost completely overlapped in the central SNR region, thus increasing the symbol rate to very high values.

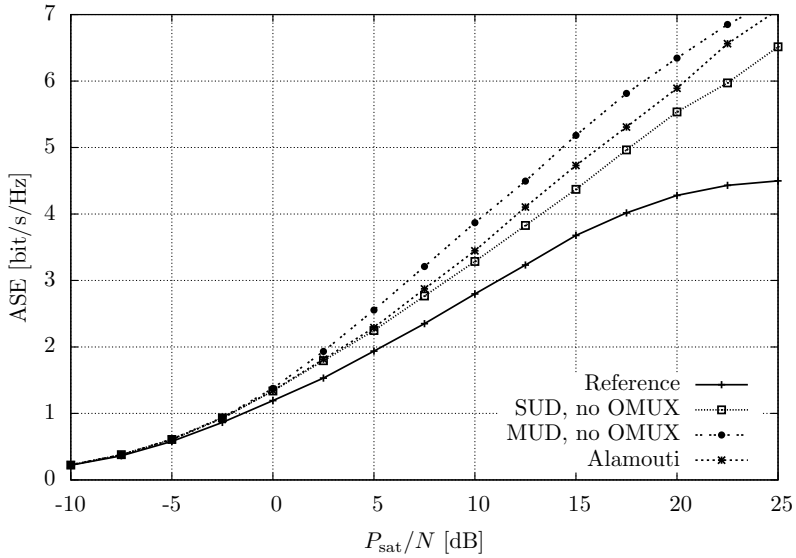

Figure 5.9: ASE for the two channels scenario with $L = 1$.

P_{sat}/N [dB]	R_{s} [Mbaud]	F [MHz]
-10	572	594
-5	704	528
0	1364	66
5	1408	66
10	1452	0
15	1760	66
20	1760	132
25	1804	198

Table 5.2: Optimized symbol rate and frequency spacing for the MUD with $L = 1$ and 8PSK.

5.3 Conclusions

We have analyzed two different scenarios of EO links, with one and two channels, respectively. We have shown that, in both cases, significant SE gains are possible with respect to the current configuration through the application of advanced techniques at the transmitter and at the receiver. In particular, we have optimized the symbol rate and introduced more sophisticated detection algorithms. For the scenario with two channels, we have also demonstrated that the application of frequency packing, coupled with a MUD at the receiver, can achieve an excellent performance when compared with all other techniques. Finally, we have proposed the use of the Alamouti scheme as a lower complexity alternative to the MUD.

Conclusions

In this thesis, we have considered four different scenarios in the area of satellite communications. For each scenario, we have presented advanced techniques to improve the spectral efficiency of the transmission.

First of all, we have investigated the optimization of the current standard for digital video broadcasting. We have derived the optimal symbol rate and signal bandwidth, and verified that significant gains over conventional architectures are possible if the receiver adopts a simple fractionally-spaced equalizer. We have then evaluated the performance of more sophisticated detection algorithms and optimization techniques, namely time packing and the design of optimized constellations. While time packing cannot provide gains in this scenario, a properly designed constellation can give some further advantages. We have verified that the information theoretic results find a perfect correspondence in the use of the practical codes foreseen by the current standard and its extension.

In the second scenario, we have studied a network composed of two co-located satellites for signals broadcasting. We have modeled the system with three different models, with increasing complexity, to simulate the real satellite channel. Moreover, we have applied three alternative transmission techniques, namely signals perfectly overlapped in frequency, frequency division multiplexing, and the Alamouti space-time block code. We have verified that the performance of the three approaches strongly depends on the channel conditions, but we have shown an excellent correspondence between the linear channel with peak power constraint and a more realistic satellite channel model. This has allowed us to obtain some theoretical results, show-

ing that, in many cases of interest, the use of a second satellite can give significant gains over a single satellite system.

We have then considered the application of multiuser detection in a multibeam satellite system. In particular, we have focused our attention to users which experience a high interference from adjacent cells. Also in this case, we have compared three transceiver schemes: a classical multiuser detection approach, a time division approach in which the beams cooperate to serve each user, and the Alamouti scheme. We have analyzed the performance in different channel conditions, and verified that a solution that always outperforms the others does not exist. Finally, we have shown that classical channel codes, designed for single-user detection, are not suitable for the multiuser approach. We have then demonstrated that the information theoretic bounds can be approached by a redesign of the channel code or of the joint bit mapping of the symbols.

Finally, we have investigated the possible spectral efficiency gains in an Earth observation scenario. We have considered two different configurations, when the satellite uses one or two antennas, and applied several transceiver techniques. We have shown that properly increasing the symbol rate can provide significant advantages with respect to the reference system. Moreover, for the two channels configuration, we have compared classical single-user detection, multiuser detection, and the Alamouti scheme. We have verified that an optimized scheme using multiuser detection is the best solution, at the expense of an increased complexity. The Alamouti technique, on the other hand, provides good performance with a reduced complexity.

Bibliography

[1] L. R. Bahl, J. Cocke, F. Jelinek, and J. Raviv, "Optimal decoding of linear codes for minimizing symbol error rate," *IEEE Trans. Inform. Theory*, vol. 20, pp. 284–287, Mar. 1974.

[2] G. D. Forney, Jr., "Maximum-likelihood sequence estimation of digital sequences in the presence of intersymbol interference," *IEEE Trans. Inform. Theory*, vol. 18, pp. 284–287, May 1972.

[3] G. Ungerboeck, "Adaptive maximum likelihood receiver for carrier-modulated data-transmission systems," *IEEE Trans. Commun.*, vol. com-22, pp. 624–636, May 1974.

[4] G. Colavolpe and A. Barbieri, "On MAP symbol detection for ISI channels using the Ungerboeck observation model," *IEEE Commun. Letters*, vol. 9, pp. 720–722, Aug. 2005.

[5] F. R. Kschischang, B. J. Frey, and H.-A. Loeliger, "Factor graphs and the sum-product algorithm," *IEEE Trans. Inform. Theory*, vol. 47, pp. 498–519, Feb. 2001.

[6] D. M. Arnold, H.-A. Loeliger, P. O. Vontobel, A. Kavčić, and W. Zeng, "Simulation-based computation of information rates for channels with memory," *IEEE Trans. Inform. Theory*, vol. 52, pp. 3498–3508, Aug. 2006.

[7] N. Merhav, G. Kaplan, A. Lapidoth, and S. Shamai, "On information rates for mismatched decoders," *IEEE Trans. Inform. Theory*, vol. 40, pp. 1953–1967, Nov. 1994.

[8] U. Fincke and M. Pohst, "Improved methods for calculating vectors of short length in a lattice, including a complexity analysis," *Mathematics of computation*, vol. 44, pp. 463–471, Apr. 1985.

[9] L. G. Barbero and J. S. Thompson, "Fixing the complexity of the sphere decoder for MIMO detection," *IEEE Trans. Wireless Commun.*, vol. 7, pp. 2131–2142, June 2008.

[10] A. Prlja and J. B. Anderson, "Reduced-complexity receivers for strongly narrowband intersymbol interference introduced by faster-than-Nyquist signaling," *IEEE Trans. Commun.*, vol. 60, no. 9, pp. 2591–2601, 2012.

[11] G. Colavolpe, G. Ferrari, and R. Raheli, "Reduced-state BCJR-type algorithms," *IEEE J. Select. Areas Commun.*, vol. 19, pp. 848–859, May 2001.

[12] F. Rusek and D. Fertonani, "Bounds on the information rate of intersymbol interference channels based on mismatched receivers," *IEEE Trans. Inform. Theory*, vol. 58, pp. 1470–1482, Mar. 2012.

[13] D. D. Falconer and F. Magee, "Adaptive channel memory truncation for maximum likelihood sequence estimation," *Bell System Tech. J.*, vol. 52, pp. 1541–1562, Nov. 1973.

[14] S. A. Fredricsson, "Joint optimization of transmitter and receiver filter in digital PAM systems with a Viterbi detector," *IEEE Trans. Inform. Theory*, vol. IT-22, pp. 200–210, Mar. 1976.

[15] C. T. Beare, "The choice of the desired impulse response in combined linear-Viterbi algorithm equalizers," *IEEE Trans. Commun.*, vol. 26, pp. 1301–1307, Aug. 1978.

[16] N. Sundstrom, O. Edfors, P. Ödling, H. Eriksson, T. Koski, and P. O. Börjesson, "Combined linear-Viterbi equalizers - a comparative study and a minimax design," in *Proc. Vehicular Tech. Conf.*, (Stockholm, Sweden), pp. 1263–1267, June 1994.

[17] N. Al-Dhahir and J. M. Cioffi, "Efficiently computed reduced-parameter input-aided MMSE equalizers for ML detection: A unified approach," *IEEE Trans. Inform. Theory*, vol. 42, pp. 903–915, Apr. 1996.

[18] M. Lagunas, A. I. Perez-Neia, and J. Vidal, "Joint beamforming and Viterbi equalizer in wireless communications," in *Proc. Asilomar Conf. Signals, Systems, Comp.*, vol. 1, pp. 915–919, Nov. 1997.

[19] S. A. Aldosari, S. A. Alshebeili, and A. M. Al-Sanie, "A new MSE approach for combined linear-Viterbi equalizers," in *Proc. Vehicular Tech. Conf.*, (Tokyo, Japan), pp. 1263–1267, May 2000.

[20] U. L. Dang, W. H. Gerstacker, and D. T. M. Slock, "Maximum SINR prefiltering for reduced state trellis based equalization," in *Proc. IEEE Intern. Conf. Commun.*, (Kyoto, Japan), June 2011.

[21] F. Rusek and A. Prlja, "Optimal channel shortening for MIMO and ISI channels," *IEEE Trans. Wireless Commun.*, vol. 11, pp. 810–818, Feb. 2012.

[22] A. Modenini, F. Rusek, and G. Colavolpe, "Adaptive rate-maximizing channel-shortening for ISI channels," *IEEE Commun. Letters*, vol. 19, pp. 2090–2093, Dec. 2015.

[23] J. M. Cioffi, "Data transmission theory." Available at *http://www.stanford.edu/group/cioffi/*.

[24] S. Hu and F. Rusek, "On the design of reduced state demodulators with interference cancellation for iterative receivers," in *Proc. 24th IEEE Intern. Symp. on Personal, Indoor, and Mobile Radio Comm. (PIMRC)*, (Hong Kong, China), pp. 981–985, Aug. 2015.

[25] S. Hu and F. Rusek, "On the design of channel shortening demodulators for iterative receivers in MIMO and ISI channels." Available at *http://arxiv.org/abs/1506.07331*.

[26] J. E. Mazo, "Faster-than-Nyquist signaling," *Bell System Tech. J.*, vol. 54, pp. 1450–1462, Oct. 1975.

[27] A. Liveris and C. N. Georghiades, "Exploiting faster-than-Nyquist signaling," *IEEE Trans. Commun.*, vol. 47, pp. 1502–1511, Sept. 2003.

[28] F. Rusek and J. B. Anderson, "The two dimensional Mazo limit," in *Proc. IEEE International Symposium on Information Theory*, (Adelaide, Australia), pp. 970–974, Nov. 2005.

[29] A. Barbieri, D. Fertonani, and G. Colavolpe, "Time-frequency packing for linear modulations: spectral efficiency and practical detection schemes," *IEEE Trans. Commun.*, vol. 57, pp. 2951–2959, Oct. 2009.

[30] A. Modenini, G. Colavolpe, and N. Alagha, "How to significantly improve the spectral efficiency of linear modulations through time-frequency packing and advanced processing," in *Proc. IEEE Intern. Conf. Commun.*, (Ottawa, Canada), pp. 3299–3304, June 2012.

[31] S. Isam, I. Kanaras, and I. Darwazeh, "A truncated SVD approach for fixed complexity spectrally efficient FDM receivers," in *Proc. IEEE Wireless Commun. and Network. Conf.*, (Cancun, Mexico), pp. 1584–1589, Mar. 2011.

[32] P. Banelli, S. Buzzi, G. Colavolpe, A. Modenini, F. Rusek, and A. Ugolini, "Modulation formats and waveforms for 5G networks: Who will be the heir of OFDM?," *IEEE Signal Processing Mag.*, vol. 31, pp. 80–93, Nov. 2014.

[33] A. Piemontese, A. Modenini, G. Colavolpe, and N. Alagha, "Improving the spectral efficiency of nonlinear satellite systems through time-frequency packing and advanced processing," *IEEE Trans. Commun.*, vol. 61, pp. 3404–3412, Aug. 2013.

[34] G. Colavolpe and T. Foggi, "Time-frequency packing for high capacity coherent optical links," *IEEE Trans. Commun.*, vol. 62, pp. 2986–2995, Aug. 2014.

[35] ETSI EN 302 307-1 Digital Video Broadcasting (DVB), Second generation framing structure, channel coding and modulation systems for Broadcasting, Interactive Services, News Gathering and other broadband satellite applications, Part I: DVB-S2. Available on ETSI web site (http://www.etsi.org).

[36] ETSI EN 300 421 Digital Video Broadcasting (DVB), Framing structure, channel coding and modulation for 11/12 GHz satellite services. Available on ETSI web site (http://www.etsi.org).

[37] ETSI EN 302 307-2 Digital Video Broadcasting (DVB), Second generation framing structure, channel coding and modulation systems for Broadcasting, Interactive Services, News Gathering and other broadband satellite applications, Part II: S2-Extensions (DVB-S2X). Available on ETSI web site (http://www.etsi.org).

[38] S. Cioni, G. Colavolpe, C. Ernst, and A. Ginesi, "Bandwidth Optimization for Satellite Digital Broadcasting," in *31st AIAA International Communications Satellite Systems Conference*, (Florence, Italy), Oct. 2013.

[39] DVB-TM-S2 Channel Model Group, DVB-S2X Channel Models, Apr. 2014. Available on ETSI web site (http://www.etsi.org).

[40] M. Eroz, L.-N. Lee, N. Loghin, U. De Bie, F. Simoens, and D. Delaruelle, "New DVB-S2X constellations for improved performance on the satellite channels," *International Journal of Satellite Communications and Networking*. Article first published online: September 2015.

[41] A. Morello and V. Mignone, "DVB-S2X: extending DVB-S2 flexibility for core markets and new applications," *International Journal of Satellite Communications and Networking*. Article first published online: November 2015.

[42] J. E. Mazo and H. J. Landau, "On the minimum distance problem for faster-than-Nyquist signaling," *IEEE Trans. Inform. Theory*, pp. 1420–1427, Nov. 1988.

[43] A. Modenini, F. Rusek, and G. Colavolpe, "Optimal transmit filters for ISI channels under channel shortening detection," *IEEE Trans. Commun.*, vol. 61, pp. 4997–5005, Dec. 2013.

[44] F. Kayhan and G. Montorsi, "Constellation design for transmission over nonlinear satellite channels," in *Proc. IEEE Global Telecommun. Conf.*, (Anaheim, CA, U.S.A.), pp. 3401–3406, Dec. 2012.

[45] F. Kayhan and G. Montorsi, "Joint signal-labeling optimization under peak power constraint," *Intern. J. of Satellite Communications and Networking*, vol. 30, pp. 251–263, Nov./Dec. 2012.

[46] F. Kayhan and G. Montorsi, "Optimal constellations for the pragmatic receiver in the DVB-S2 standard," in *31st AIAA International Communications Satellite Systems Conference*, (Florence, Italy), Oct. 2013.

[47] E. Casini, R. De Gaudenzi, and A. Ginesi, "DVB-S2 modem algorithms design and performance over typical satellite channels," *Intern. J. of Satellite Communications and Networking*, vol. 22, pp. 281–318, May/June 2004.

[48] A. Barbieri and G. Colavolpe, "On pilot-symbol-assisted carrier synchronization for DVB-S2 systems," *IEEE Trans. Broadcast.*, vol. 53, pp. 685–692, Sept. 2007.

[49] S. Cioni, G. Colavolpe, V. Mignone, A. Modenini, A. Morello, M. Ricciulli, A. Ugolini, and Y. Zanettini, "Transmission parameters optimization and receiver architectures for DVB-S2X systems," *International Journal of Satellite Communications and Networking*. Article first published online: June 2015.

[50] J. B. Soriaga, H. Pfister, and P. Siegel, "Determining and approaching achievable rates of binary intersymbol interference channels using multistage decoding," *IEEE Trans. Inform. Theory*, vol. 53, pp. 1416–1429, Apr. 2007.

[51] S. Benedetto, E. Biglieri, and V. Castellani, *Digital Transmission Theory*. Englewood Cliffs, NJ: Prentice-Hall, 1987.

[52] A. Modenini, *Advanced transceivers for spectrally-efficient communications*. PhD thesis, University of Parma, Parma, Italy, Jan. 2014.

[53] Digital Video Broadcasting (DVB), Report of the TM-S2 study mission on green field technologies for satellite transmissions, Jan. 2014.

[54] H. Meyr, M. Oerder, and A. Polydoros, "On sampling rate, analog prefiltering, and sufficient statistics for digital receivers," *IEEE Trans. Commun.*, vol. 42, pp. 3208–3214, Dec. 1994.

[55] G. Colavolpe, A. Modenini, and F. Rusek, "Channel shortening for nonlinear satellite channels," *IEEE Commun. Letters*, vol. 16, pp. 1929–1932, Dec. 2012.

[56] G. Colavolpe and A. Piemontese, "Novel SISO detection algorithms for nonlinear satellite channels," *IEEE Wireless Commun. Letters*, vol. 1, pp. 22–25, Feb. 2012.

[57] G. Karam and H. Sari, "Analysis of predistortion, equalization, and ISI cancellation techniques in digital radio systems with nonlinear transmit amplifiers," *IEEE Trans. Commun.*, vol. 37, pp. 1245–1253, Dec 1989.

[58] S. ten Brink, "Designing iterative decoding schemes with the extrinsic information transfer chart," *AEU Int. J. Electronic. Commun.*, vol. 54, pp. 389–398, Dec. 2000.

[59] S. Haykin, *Adaptive Filter Theory*. Englewood Cliffs, NJ: Prentice-Hall, 3rd ed., 1996.

[60] S. M. Alamouti, "A simple transmit diversity technique for wireless communications," *IEEE J. Select. Areas Commun.*, vol. 16, pp. 1451–1458, Oct. 1998.

[61] S. Sharma, S. Chatzinotas, and B. Ottersten, "Cognitive beamhopping for spectral coexistence of multibeam satellites," in *Future Network and Mobile Summit (FutureNetworkSummit), 2013*, pp. 1–10, July 2013.

[62] D. Christopoulos, S. Chatzinotas, and B. Ottersten, "User scheduling for coordinated dual satellite systems with linear precoding," in *Proc. IEEE Intern. Conf. Commun.*, pp. 4498–4503, June 2013.

[63] J. G. Smith, "The information capacity of amplitude- and variance-constrained scalar Gaussian channels," *Information and Control*, vol. 18, pp. 203–219, Apr. 1971.

[64] S. Shamai (Shitz), "On the capacity of a Gaussian channel with peak power and bandlimited input signals," *Archiv Elektronik und Uebertragungstechnik (AEU)*, vol. 42, pp. 340–346, Dec. 1988.

[65] S. Shamai (Shitz) and I. Bar-David, "The capacity of average and peak-power-limited quadrature Gaussian channels," *IEEE Trans. Inform. Theory*, vol. 41, pp. 1061–1071, July 1995.

[66] T. M. Cover and J. A. Thomas, *Elements of Information Theory*. New York: John Wiley & Sons, 2nd ed., 2006.

[67] T. M. Cover, "An achievable rate region for the broadcast channel," *IEEE Trans. Inform. Theory*, vol. 21, pp. 399–404, July 1975.

[68] G. Caire and S. Shamai (Shitz), "On the achievable throughput of a multi-antenna Gaussian broadcast channel," *IEEE Trans. Inform. Theory*, vol. 49, pp. 1691–1706, July 2003.

[69] H. Weingarten, Y. Steinberg, and S. Shamai (Shitz), "The capacity region of the Gaussian multiple-input multiple-output broadcast channel," *IEEE Trans. Inform. Theory*, vol. 52, pp. 3936–3964, Sept. 2006.

[70] A. El Gamal and T. M. Cover, "Multiple user information theory," *Proceedings of the IEEE*, vol. 68, pp. 1466–1483, Dec. 1980.

[71] A. Modenini, A. Ugolini, A. Piemontese, and G. Colavolpe, "On the use of multiple satellites to improve the spectral efficiency of broadcast transmissions," *IEEE Trans. Broadcast.*, vol. 61, pp. 590–602, Dec. 2015.

[72] C. Shannon, "A mathematical theory of communication," *Bell System Tech. J.*, pp. 379–423, July 1948.

[73] A. Dembo, T. M. Cover, and J. A. Thomas, "Information theoretic inequalities," *IEEE Trans. Inform. Theory*, vol. 37, pp. 1501–1518, Nov. 1991.

[74] D. Guo, S. Shamai, and S. Verdú, "Mutual information and minimum mean-square error in Gaussian channels," *IEEE Trans. Inform. Theory*, vol. 51, pp. 1261–1282, Apr. 2005.

[75] W. Feller, *An Introduction to Probability Theory and Its Applications, Vol. 2*. John Wiley & Sons, 3rd ed., 1971.

[76] E. Lukacs and E. P. King, "A property of the normal distribution," *The Annals of Mathematical Statistics*, vol. 25, no. 2, pp. 389–394, 1954.

[77] B. Mamandipoor, K. Moshksar, and A. K. Khandani, "On the sum-capacity of Gaussian MAC with peak constraint," in *Proc. IEEE International Symposium on Information Theory*, (Cambridge, MA), pp. 26–30, July 2012.

[78] S. Verdú, *Multiuser Detection*. Cambridge, UK: Cambridge University Press, 1998.

[79] G. Colavolpe, N. Mazzali, A. Modenini, A. Piemontese, and A. Ugolini, "Next generation waveforms for improved spectral efficiency," tech. rep., Sept. 2013. ESA Contract No. 4000106528.

[80] G. Colavolpe, A. Modenini, A. Piemontese, and A. Ugolini, "Interference management techniques for satellite networks – Candidate interference management techniques and evaluation methodology – Scenario 1," tech. rep., Nov. 2014. ESA Contract No. 4000109715/13/NL/FE.

[81] S. ten Brink, G. Kramer, and A. Ashikhmin, "Design of low-density parity-check codes for modulation and detection," *IEEE Trans. Commun.*, vol. 52, pp. 670–678, Apr. 2004.

[82] S. Andrenacci, M. Angelone, E. A. Candreva, G. Colavolpe, A. Ginesi, F. Lombardo, A. Modenini, C. Morel, A. Piemontese, and A. Vanelli-Coralli, "Physical layer performance of multi-user detection in broadband multi-beam systems based on DVB-S2," in *Proc. European Wireless (EW 2014)*, (Barcelona, Spain), May 2014.

[83] G. Cocco, M. Angelone, and A. I. Perez-Neira, "Co-channel interference cancellation at the user terminal in multibeam satellite systems," in *Proc. 7th Advanced Satell. Mobile Syst. Conf. and 13th Intern. Workshop on Signal Proc. for Space Commun. (ASMS&SPSC 2014)*, (Livorno, Italy), pp. 43–50, Sept. 2014.

[84] A. Piemontese, A. Graell i Amat, and G. Colavolpe, "Frequency packing and multiuser detection for CPMs: how to improve the spectral efficiency of DVB-RCS2 systems," *IEEE Wireless Commun. Letters*, vol. 2, pp. 74–77, Feb. 2013.

[85] B. F. Beidas, H. El Gamal, and S. Kay, "Iterative interference cancellation for high spectral efficiency satellite communications," *IEEE Trans. Commun.*, vol. 50, pp. 31–36, Jan. 2002.

[86] G. Colavolpe, D. Fertonani, and A. Piemontese, "SISO detection over linear channels with linear complexity in the number of interferers," *IEEE J. Sel. Topics in Signal Proc.*, vol. 5, pp. 1475–1485, Dec. 2011.

[87] S. ten Brink, "Convergence behavior of iteratively decoded parallel concatenated codes," *IEEE Trans. Commun.*, vol. 49, pp. 1727–1737, Oct. 2001.

[88] W. Nam, D. Bai, J. Lee, and I. Kang, "Advanced interference management for 5G cellular networks," *IEEE Commun. Mag.*, vol. 52, pp. 52–60, May 2014.

[89] F. Brännström, L. K. Rasmussen, and A. J. Grant, "Convergence analysis and optimal scheduling for multiple concatenated codes," *IEEE Trans. Inform. Theory*, vol. 51, pp. 3354–3364, Sept. 2005.

[90] H. Xiao and A. H. Banihashemi, "Improved progressive-edge-growth (PEG) construction of irregular LDPC codes," *IEEE Commun. Letters*, vol. 8, pp. 715–717, Dec. 2004.

[91] W. Cauer, *Synthesis of linear communication networks*. New York: McGraw–Hill, 2nd ed., 1958.

[92] L. Ding, G. Zhou, D. Morgan, M. Zhengxiang, J. Kenney, K. Jaehyeong, and C. Giardina, "A robust digital baseband predistorter constructed using memory polynomials," *IEEE Trans. on Commun.*, vol. 52, pp. 159–165, Jan. 2004.

[93] N. Mazzali, B. Shankar, and B. Ottersten, "On-board signal predistortion for digital transparent satellites," in *Proc. IEEE Intern. Work. on Signal Processing Advances for Wireless Commun.*, (Stockholm, Sweden), pp. 535–539, June-July 2015.

[94] N. Kelly, M. Allegue-Martínez, P.-D. Arapoglou, and A. Zhu, "Bandwidth-constrained digital pre-compensation technique for multi-carrier satellite communications," *International Journal of Satellite Communications and Networking*. Article first published online: April 2015.

[95] M. J. D. Powell, "The BOBYQA algorithm for bound constrained optimization without derivatives," tech. rep., Department of Applied Mathematics and Theoretical Physics, Cambridge, England, Aug. 2009.

[96] S. G. Johnson, "The NLopt nonlinear-optimization package." *http://ab-initio.mit.edu/nlopt*.

[97] B. Beidas, R. Seshadri, and N. Becker, "Multicarrier successive predistortion for nonlinear satellite systems," *IEEE Trans. on Commun.*, vol. 63, pp. 1373–1382, Apr. 2015.

[98] R. Piazza, B. Shankar, E. Zenteno, D. Ronnow, J. Grotz, F. Zimmer, M. Grasslin, F. Heckmann, and S. Cioni, "Multicarrier digital pre-distortion/equalization techniques for non-linear satellite channels," in

Proc. AIAA Intern. Communications Satellite Systems Conf., (Ottawa, Canada), Sept. 2012.

[99] R. Piazza, B. M. R. Shankar, and B. Ottersten, "Data predistortion for multicarrier satellite channels based on direct learning," *IEEE Trans. Signal Processing*, vol. 62, pp. 5868–5880, Nov. 2014.

[100] E. Zenteno, R. Piazza, B. M. R. Shankar, D. Rönnow, and B. Ottersten, "Multiple-input multiple-output symbol rate signal digital predistorter for nonlinear multi-carrier satellite channels," *IET Communications*, vol. 9, no. 16, pp. 2053–2059, 2015.

Acknowledgements

The work presented in this thesis is the outcome of the years of the Ph.D. course. It has been accomplished thanks to the help of several people I had the opportunity to collaborate with. First of all, my gratitude goes to my supervisor, Giulio Colavolpe, for his constant help and support. Then, I am thankful to my past and present colleagues at SPADiC Lab—Amina, Andrea, Michelangelo, Nicolò, Tommaso, and Yuri—for the friendly environment and fruitful collaboration.